Electron-Positron Annihilation into Photons

at $\sqrt{s}$ = 50 to 64 GeV

by

Kevin L. Sterner

Dissertation submitted to the Faculty of the

Virginia Polytechnic Institute and State University

in partial fulfillment of the requirements for the degree of

DOCTOR OF PHILOSOPHY

in

Physics

APPROVED:

Alexander Abashian, Chairman

Kazuo Gotow

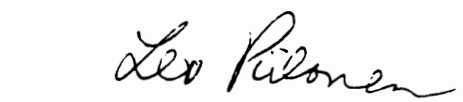

Leo Piilonen

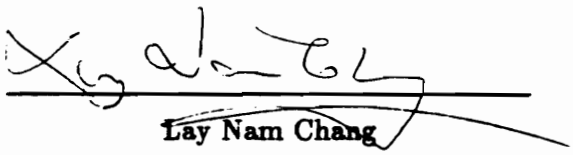

Lay Nam Chang

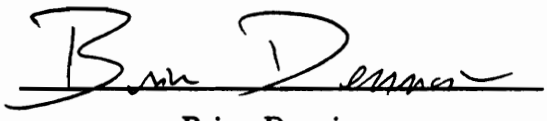

Brian Dennison

December, 1993

Blacksburg, Virginia

Electron-Positron Annihilation into Photons

at $\sqrt{s}$ =50 to 64 GeV

by

Kevin L. Sterner

Committee Chairman: Alexander Abashian

Physics

(ABSTRACT)

We present a study of e^+e^- collisions where only photons are visible in the final state in data taken with the AMY detector at TRISTAN. Data are presented at CM energies from 50 to 64 GeV, with a total integrated luminosity of 189.1 pb^{-1}. Differential cross sections for $e^+e^- \rightarrow \gamma\gamma, \gamma\gamma\gamma$ are measured and compared to $\mathcal{O}(\alpha^3)$ QED. A search for electron compositeness through an $e^+e^-\gamma\gamma$ contact interaction is conducted, and limits are presented. A search for the pair production of unstable photinos is also presented with limits. Finally, the result of a search for anomalous $\gamma\gamma$ production is presented, based upon energy scan data taken in December, 1992.

Acknowledgements

This thesis rests so squarely on the brilliance of others that I blush to call it "my work". The theoretical underpinnings, the analysis techniques, the experimental equipment, and the lion's share of the software were all developed by many people much more capable than I. I gratefully acknowledge their achievements.

I also acknowledge the hard work and expertise of the other AMY collaborators and of the TRISTAN staff. I joined the collaboration after the construction phase was completed and data were already being taken. Still, the collaboration generously let me sift through the data and publish results, even though I did not fully participate in the preceding work. They have my deepest thanks. I would also like to specifically thank Professors Steve Olsen, Akihiro Maki, and Kazuo Abe for leading the collaboration which has been so good to me.

My advisors, Professors Alexander Abashian, Kazuo Gotow, and Leo Piilonen provided outstanding guidance and generous support throughout my years as a graduate student. I thank them for giving me a start in this best-of-all careers. I also thank Professors Brian Dennison and Lay Nam Chang for kindly serving on my thesis committee.

I received a great deal of help and encouragement from my co-workers at VPI. Drs. Anzhi Lai, Kangping Hu Loewenstein, and comrade Mark Mattson helped me get through everything, from the classes we attended to the analysis of my data. Drs. Eva Low and Dan Haim, and yes, even Master Tim Duty provided help and advice whenever I needed it.

All of the figures in Chapters 1 and 2, plus Figure 4-2, were produced by my wife, Patricia F. Sterner. The AMY Collaboration is welcome to use them with proper credit.

Many of my excellent friends supported me with encouragement and kindness. They are too numerous to list here, but a few stand out as my "rocks of Gibraltar". Peter Klier, Dr. Robert Downes, Stefan Jones, John A. ("JAM") Madonia and Paula Peterson, Dr. Peter MacPherson, and Peter and Laurel Kandianis are model human beings, one and all.

I also thank the humble American taxpayer, whose wealth was expropriated, under threat of incarceration, to fund this research. Although the benefits (let alone the contents) of this research are not easily grasped by the average taxpayer, I at least owe him the best quality research I can produce.

Ayn Rand, Edward Gibbon, Friedrich Nietzsche, and Rush Limbaugh provided the moral and philosophical guidance I needed. Bruce Sterling taught me to follow my weird, embrace my nerditude, and celebrate my geekdom. Thanks, man.

My brother David and my sister, Dr. Diana Hamilton, provided friendly competition and encouragement in the race to complete our Ph.D.'s. Diana won, even though I had a two-year head start. The joy of such a contest is that even "losing" is an occasion of great pride.

My parents, Charles and Linda Sterner, contributed genetic material I've found invaluable. They also provided me with a stable and nurturing home life, and paid for my undergraduate education. The love and encouragement they continue to give me is perhaps most valuable of all.

Finally, this thesis would have been flatly impossible without the love, understanding, and technical skills of my wife, Tricia. She gave up a lucrative design position back home in Pennsylvania just to "live in squander [*sic*]" (as they say in Blacksburg) on my graduate stipend, waited for me while I worked in Japan, and saw me through to the completion of my Ph.D. In return for her sacrifice and patience, I dedicate this work, in love, to her.

Contents

List of Figures

List of Tables

Chapter 1

Introduction

The simplest possible gauge symmetry is the U(1) symmetry of quantum electrodynamics (QED); one of the simplest processes described by QED is the annihilation of an electron and a positron into a pair of photons. Because of this simplicity, $e^+e^- \to \gamma\gamma$ provides a clean test of QED even at very high collision energies. Indeed, the simplicity of this process is preserved well past the Z-pole, as the electroweak interaction contributes no new diagrams at the tree level.

It was shown very early, however, that the vacuum is not so pat: in any physical example of this process, the initial state electron and positron will suffer some amount of photon bremsstrahlung [1]. As one improves an experiment in order to detect these radiated photons, an ever-increasing number of photons at ever-decreasing energies is observed. The effect of this infrared divergence is such that, no matter how sophisticated one's experiment, the final state can never be completely described.

Clearly, for any experiment with the energy and angular resolution sufficient to resolve even the coarsest of these radiative effects, any measurement of this process must include higher order real corrections ($e^+e^- \to \gamma\gamma\gamma$, etc.) and virtual corrections in the perturbative expansion. One would then also hope to measure experimentally these higher-order processes

with more than two photons in the final state; this would allow empirical measurements of the sizes of the predicted corrections, and also provide supplemental tests of the underlying physics.

Once the radiative corrections have been dealt with, measurements of $e^+e^- \to \gamma\gamma$ can be used to explore not only QED, but physics beyond the standard model. Deviations in the differential cross section might reveal evidence for possible electron substructure. Highly acoplanar $\gamma\gamma$ events might provide evidence for an unstable photino, the conjectured supersymmetric partner to the photon.

Very recently, the L3 experiment at LEP recorded four interesting events containing two leptons and two photons in the final state, with no missing momentum or energy [2]. While each event by itself was perfectly consistent with QED, the invariant mass distribution of the photon pairs was anomalously clumped near 60 GeV. While this observation meshes neatly with neither the Standard Model nor any of its conjectured extensions, it does raise the possibility of a state near 60 GeV that decays primarily into two photons.

In this dissertation, we will examine $e^+e^- \to \gamma\gamma, \gamma\gamma\gamma$ in data taken with the AMY detector at the TRISTAN e^+e^- collider. The data represent a total luminosity of 189.1 pb^{-1} at center-of-momentum energies from 50 to 64 GeV. In the remainder of this chapter, we will examine e^+e^- annihilation into photons in the Standard Model, and the effects of several simple extensions to the Standard Model. Chapter 2 gives an overview of the experimental apparati, namely, TRISTAN and AMY. In Chapter 3 we will cover the Monte Carlo methods that allow us to compare the experimental data to the Standard Model. Chapter 4 will describe the methods used to select $e^+e^- \to n\gamma$ events from the AMY data. Chapter 5 will list the criteria used to select the data samples. Chapters 6 and 7 will present the analysis of $e^+e^- \to \gamma\gamma$ and $e^+e^- \to \gamma\gamma\gamma$ and show the comparison with standard QED, while Chapter 8 will employ these results to search for evidence of electron compositeness. Chapter 9 will present a search for unstable photinos. Conclusions are presented in Chapter 10. Two appendices are presented at the end of the dissertation: the first presents the results

of a search for the resonant production of $\gamma\gamma$ events near 60 GeV, and the second concerns the conversion of photons to e^+e^- pairs.

1.1 $e^+e^- \to \gamma\gamma$, $\gamma\gamma\gamma$ in the Standard Model

1.1.1 The Born Cross Section

The process $e^+e^- \to \gamma\gamma$ is described at tree level by two QED Feynman diagrams (Figure 1-1). In the first, or t-channel diagram, we describe the positron by a Dirac spinor u_1 with 4-momentum p_1 and spin s_1, and the electron by a spinor $u_2(p_2, s_2)$. The outgoing photons are assigned momenta (polarizations) of q_1 (ϵ_1) and q_2 (ϵ_2), respectively. This yields the invariant amplitude

$$-i\mathcal{M}_1 = (ie)^2 \bar{u}_1(p_1, s_1) \left(\not{\epsilon}_1^* \frac{i}{\not{p}_1 - \not{q}_1 - m} \not{\epsilon}_2^* \right) u_2(p_2, s_2), \tag{1.1}$$

where m is the electron mass, and slashes indicate multiplication by the Dirac matrices.

The second, or u-channel diagram is the same as the first, except that the identities of the final state photons have been interchanged. This produces the invariant amplitude

$$-i\mathcal{M}_2 = (ie)^2 \bar{u}_1(p_1, s_1) \left(\not{\epsilon}_2^* \frac{i}{\not{p}_1 - \not{q}_2 - m} \not{\epsilon}_1^* \right) u_2(p_2, s_2). \tag{1.2}$$

When we average over initial states and sum over final states, the square of the summed amplitude in the high-energy limit is proportional to the Born cross section:

$$\left(\frac{d\sigma}{d\Omega} \right)^{\gamma\gamma}_{\text{Born}} = \frac{1}{64\pi^2 s} \overline{|\mathcal{M}_1 + \mathcal{M}_2|^2} = \frac{\alpha^2}{2s} \left[\frac{t}{u} + \frac{u}{t} \right] = \frac{\alpha^2}{s} \frac{1 + \cos^2\theta}{1 - \cos^2\theta}, \tag{1.3}$$

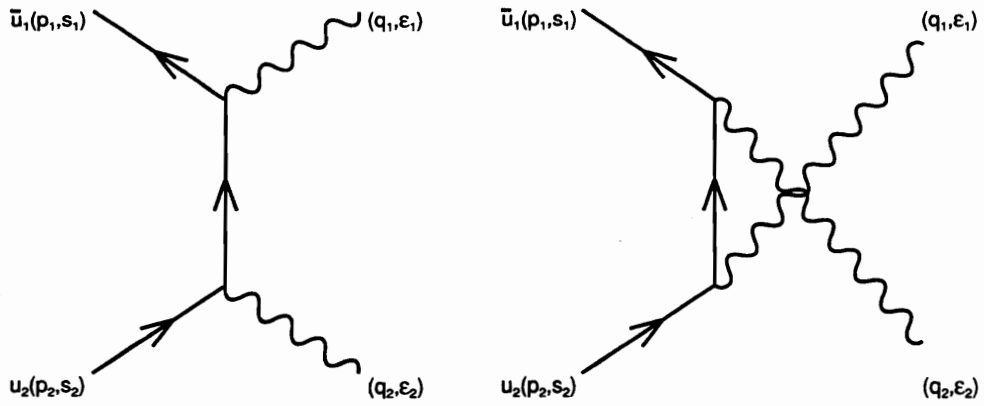

Figure 1-1: Tree level diagrams for $e^+e^- \rightarrow \gamma\gamma$.

where α is the fine structure constant, s, t, u are the usual Mandelstam variables $s = 4E^2$, $t = -\frac{s}{2}(1 - \cos\theta)$, $u = -\frac{s}{2}(1 + \cos\theta)$ in the center-of-mass frame in the high-energy limit, E is the incident beam energy, and θ is the angle between the incoming electrons and the outgoing photons in the center-of-mass frame.

This cross section exhibits—insofar as we can assign directions—singular forward and backward peaks in the final state. These correspond to the cases where the t-channel and u-channel electron propogators are almost on-shell. Experimentally, of course, these electrons are as indistinguishable as the final state photons.

1.1.2 Virtual Corrections to $e^+e^- \to \gamma\gamma$

The low-order QED virtual corrections are shown in Figs. 1-2 – 1-4, and include electron self-energy diagrams, vertex corrections, and box diagrams. Contributions from diagrams with a fermion loop, a charged boson loop, or a Fadeev-Popov ghost loop are negligible [3], [4].

Each of the virtual corrections can be expressed in the form:

$$\left(\frac{d\sigma}{d\Omega}\right)_a^{\gamma\gamma} = \frac{\alpha^3}{2\pi s} \cdot [G_a(s,t) + G_a(s,u)] \equiv \left(\frac{d\sigma}{d\Omega}\right)_{\text{Born}}^{\gamma\gamma} \cdot \delta_a, \tag{1.4}$$

where the subscript a indicates the type of QED virtual correction, i.e. self-energy, vertex, or box diagram correction. The terms $G_a(s,u)$ are identical to the terms $G_a(s,t)$ with t and u interchanged [5].

Electroweak effects begin to appear in the perturbative expansion at the one-loop level. We will not cover them in this dissertation; their contributions at TRISTAN energies are small, and they would cloud our discussion of QED. Then, too, the virtual corrections due to the weak bosons are not as simple as the corresponding virtual photon corrections, since the W and Z masses are so large. The reader is referred to [6] for a complete discussion of the $\mathcal{O}(\alpha^3)$ electroweak virtual corrections to $e^+e^- \to \gamma\gamma$.

Electron Self-Energy Correction

The diagrams for $e^+e^- \rightarrow \gamma\gamma$ including electron self-energy due to the photon are shown in Figure 1-2.[1] The calculation of the contributions from these diagrams is straightforward, but leads to a grave conceptual difficulty: because the photon is massless, and because the net momentum transfer for the added photon propagator is zero, the contribution from these diagrams is actually infinite. With a wink and a nod we will set this problem aside, by assigning a fictitious, unspecified rest mass λ to the photon.[2]

The QED self energy correction is thus:

$$G_{\text{self}}(s,t) = \left[\ln\left(\frac{\lambda^2}{m^2}\right) + \frac{1}{2}\ln\left(\frac{-t}{m^2}\right) + \frac{3}{2}\right] \cdot \frac{u}{t}. \tag{1.5}$$

Vertex Correction

The four diagrams for the photon vertex correction are shown in Figure 1-3. As in the case of electron self-energy, the photon propagator leads to a divergence of order $\ln\lambda$. The resulting correction is

$$G_{\text{vertex}}(s,t) = \left[-2\ln\left(\frac{\lambda^2}{m^2}\right) - \ln\left(\frac{-t}{m^2}\right) - 3\right] \cdot \frac{u}{t} - 2\ln\left(\frac{-t}{m^2}\right) + 1. \tag{1.6}$$

[1] We can also draw four other diagrams of the same order, where the self-energy correction is applied to the external electron lines. Because the initial state electron and positron are on-shell by construction, however, the contribution from these diagrams is zero. The effect of electron self-energy is implicitly included in the mass of the electron.

[2] This is not a dishonest approach. The offensive infinite quantity hides in a term proportional to $\ln\lambda$, which returns our infinity upon evaluation.

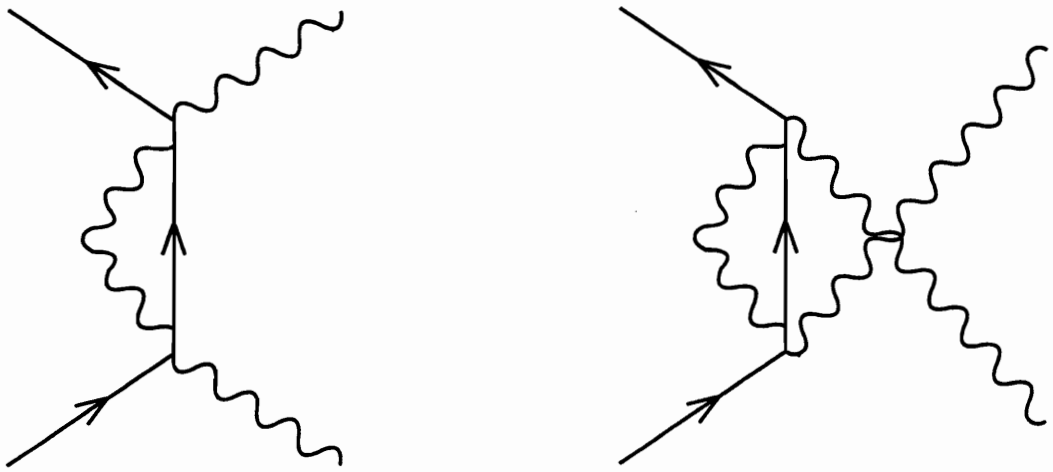

Figure 1-2: Diagrams for electron self-energy due to the photon.

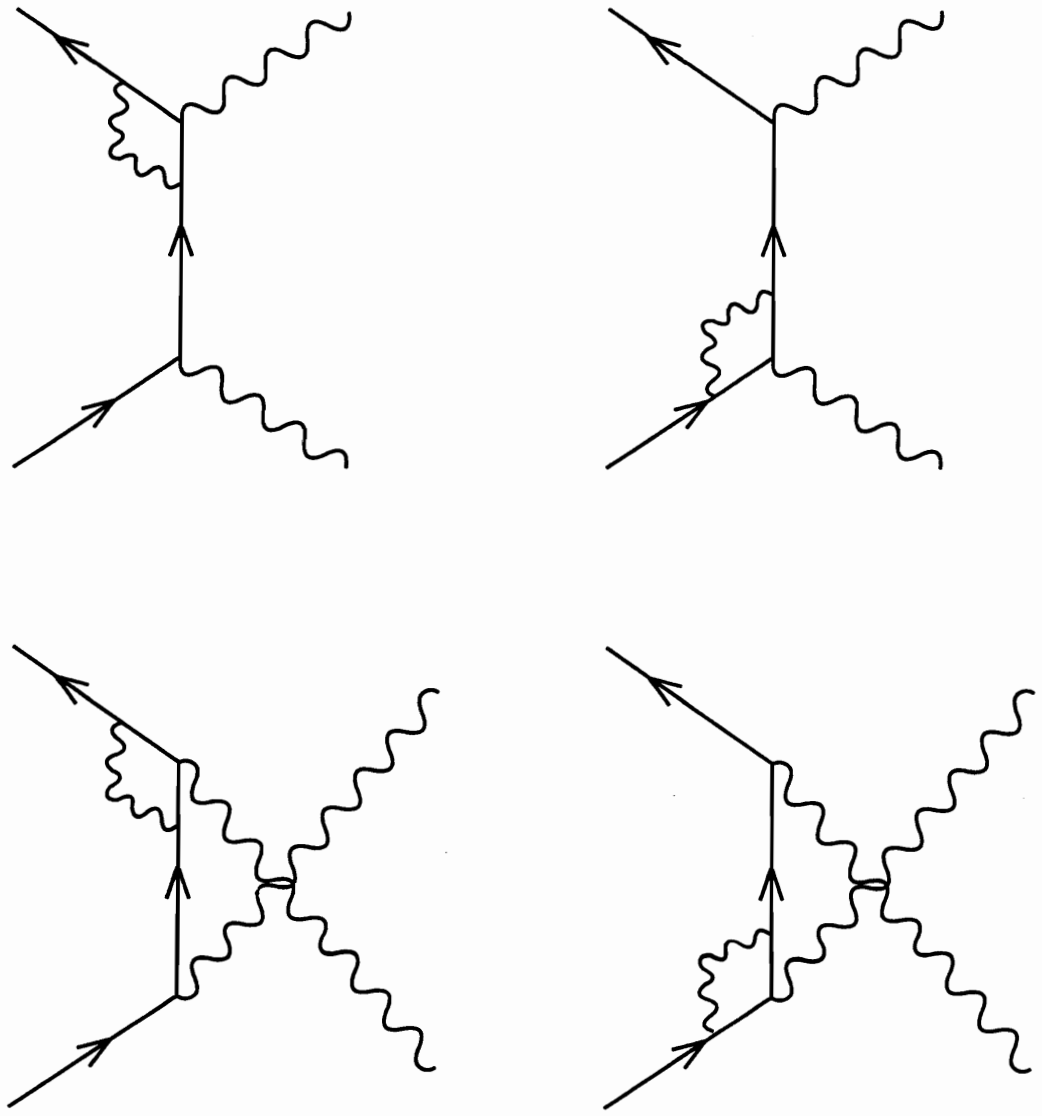

Figure 1-3: Photon vertex correction diagrams for $e^+e^- \rightarrow \gamma\gamma$.

Box Diagram Correction

The two photon box diagrams are shown in Figure 1-4. Details of the calculation can be found in [7]; here we quote the result:

$$\begin{aligned} G_{\rm box}(s,t) &= 2C\cdot\frac{u}{t} + D\cdot\left(2-\frac{u}{t}+2\frac{t}{u}\right) - \frac{t}{4s}\cdot\left(7+3\frac{t}{u}\right)\cdot[\ln(b)]^2 \\ &\quad + \ln(b) + \left(2+\frac{u}{t}+2\frac{t}{u}\right)\cdot\left\{\frac{\pi}{3}+\frac{1}{2}\cdot\left[\ln\left(\frac{-t}{m^2}\right)\right]^2\right\} \\ &\quad + \left(2\frac{u}{t}+3\right)\cdot\ln\left(\frac{-t}{m^2}\right) - 1, \end{aligned} \tag{1.7}$$

where

$$C = \ln(b)\ln\left(\frac{m}{\lambda}\right) + \frac{\pi^2}{4} + \ln\left(\frac{-t}{m^2}\right)\ln(b), \tag{1.8}$$

$$D = \frac{1}{4}[\ln(b)]^2 + \frac{\pi^2}{6} + \ln\left(\frac{-t}{m^2}\right)\ln(b), \tag{1.9}$$

and

$$b = (1-a)/(1+a), \quad a = \sqrt{1-4m^2/s}. \tag{1.10}$$

1.1.3 Real Corrections to $e^+e^- \to \gamma\gamma$

We now must consider the effect of a third real photon in the final state. We have seen that arbitrary numbers of photons are always present, but even one additional photon leads to a problem: if we could devise an experiment to catch all three photons (even those of an arbitrarily small energy), the entire $\gamma\gamma$ cross section would be subsumed into the $\gamma\gamma\gamma$ cross section. One practical way to approach this problem is to choose some minimum photon energy (ideally somewhat below the experimental detection limit, but otherwise arbitrary).

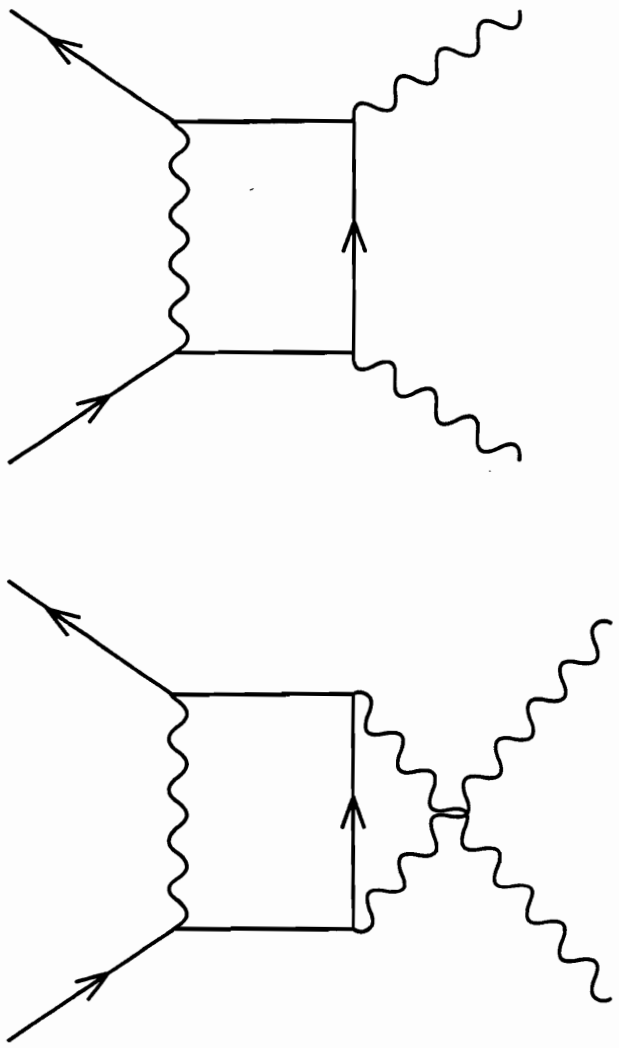

Figure 1-4: Photon box diagrams for $e^+e^- \rightarrow \gamma\gamma$.

The "soft photon" emission cross section—that part of the $\gamma\gamma$ cross section below the photon energy cut—can then be calculated without considering the momentum of the third photon, and included as a correction to the $\gamma\gamma$ cross section [7]. The "hard photon" emission cross section, where the momentum of the third photon becomes important, can be treated separately.[3]

1.1.4 Soft Photon Emission Correction to $e^+e^- \to \gamma\gamma$

The cross section for emitting an additional photon of some small energy E_{soft} is proportional to $1/E_{\text{soft}}$, thus the cross section for producing an $e^+e^- \to \gamma\gamma$ event *without* an additional photon is exactly zero. In an experiment where we wish to distinguish a $\gamma\gamma$ from a $\gamma\gamma\gamma$ event, however, what we want to know is the cross section for producing an $e^+e^- \to \gamma\gamma$ event without additional photons *except* those below the detection limit. This part of the cross section diverges.

As in the case of the virtual corrections, we can regulate this divergence by pretending that the photon has a finite mass λ. The part of the soft emission cross section containing this divergence can be separated from the finite part, thus:

$$\left(\frac{d\sigma}{d\Omega}\right)^{\gamma\gamma}_{\text{soft}} = \left(\frac{d\sigma}{d\Omega}\right)^{\gamma\gamma}_{\text{Born}} \cdot [R_{\text{div}}(E_{\text{soft}}, \lambda) + R_{\text{finite}}]\,. \tag{1.11}$$

The calculations of R_{div} and R_{finite} are too lengthy to present here, but they are derived in a number of sources [9], [10], [11]. If we assume (as at TRISTAN) that the laboratory frame is the CM frame, we state that

[3] An alternative approach, calculating the infrared divergence non-perturbatively using the Yennie-Frautschi-Suura exponentiation technique [8], shows great promise, but has yet to be implemented in the $e^+e^- \to n\gamma$ case. The main practical advantage to the YFS approach is the accurate generation of many soft photons in a single event without having to calculate intractable legions of diagrams.

$$
\begin{aligned}
R_{\text{div}} &= \frac{\alpha}{\pi}\left[\frac{1+a^2}{a}\ln\left(\frac{1}{b}\right) - 2\right]\ln\left(\frac{2E_{\text{soft}}}{\lambda}\right) \\
R_{\text{finite}} &= \frac{\alpha}{\pi}\left\{\frac{1}{a}\ln\left(\frac{1}{b}\right) - \frac{1+a^2}{2a}\left[2\text{Sp}\left(\frac{2a}{1+a}\right) + \frac{1}{2}\ln^2\left(\frac{1}{b}\right)\right]\right\},
\end{aligned}
\tag{1.12}
$$

where m is the electron mass, and we have introduced the Spence function

$$
\text{Sp}(x) = -\int_0^x \frac{\ln(1-t)}{t}dt. \tag{1.13}
$$

Taking the extreme relativistic limit, and knowing that $\text{Sp}(1) = \pi/6$, we see that

$$
\begin{aligned}
R_{\text{div}} &= \frac{\alpha}{\pi}2\left[\ln\left(\frac{s}{m^2}\right) - 1\right]\cdot\ln\left(\frac{2E_{\text{soft}}}{\lambda}\right), \\
R_{\text{finite}} &= \frac{\alpha}{\pi}\left[\ln\left(\frac{s}{m^2}\right) - \frac{1}{2}\ln^2\left(\frac{s}{m^2}\right) - \frac{\pi^2}{3}\right].
\end{aligned}
\tag{1.14}
$$

The soft photon emission contribution to the $\gamma\gamma$ cross section is then given by:

$$
\left(\frac{d\sigma}{d\Omega}\right)^{\gamma\gamma}_{\text{soft}} = \left(\frac{d\sigma}{d\Omega}\right)^{\gamma\gamma}_{\text{Born}}\cdot\frac{\alpha}{\pi}\left[2(\rho-1)\cdot\ln\left(\frac{2E_{\text{soft}}}{\lambda}\right) + \rho - \frac{1}{2}\rho^2 - \frac{\pi^2}{3}\right], \tag{1.15}
$$

where $\rho = \ln(s/m^2)$. It should be noted that all of the angular dependence for this expression is contained in the Born cross section, i.e. that the soft photons are radiated isotropically.

1.1.5 $e^+e^- \to \gamma\gamma\gamma$ Cross Section

Before we can calculate the contribution to the $\gamma\gamma$ cross section from the emission of a hard real photon, it is of course necessary to compute the cross section for electron-positron

annihilation into three photons. There are six diagrams for $e^+e^- \to \gamma\gamma\gamma$. One of these is shown in Figure 1-5; the other diagrams are distinguished only by the order of the final state photons [12].

The differential cross section for $e^+e^- \to \gamma\gamma\gamma$ is somewhat more difficult to express than that for $e^+e^- \to \gamma\gamma$, simply because there are three particles in the final state. If we note that there are three independent momentum dimensions for each photon and four energy/momentum constraint equations, we see that the differential cross section has five dimensions, rather than the simple two dimensions of the $e^+e^- \to \gamma\gamma$ cross section.[4] There are many possible coordinate system choices for this 5-dimensional space; here we illustrate one [13].

We start with the standard right-handed Cartesian coordinate system defined relative to the AMY detector. The $+z$-axis is defined as being in the direction of the initial-state electron; polar angles are measured relative to this axis. Azimuthal angles are measured relative to the $+x$-axis, clockwise as viewed from the $+z$-axis. The $+y$-axis is defined as pointing in the $-(\hat{x} \times \hat{z})$ direction ("upwards", in the vernacular).

Next we will define four of the five independent dimensions by choosing the directions of two of the photons, denoted (θ, ϕ) and (θ', ϕ'), respectively. These are illustrated in Figure 1-6.

We must be careful in choosing our last coordinate. It is not convenient to choose a polar or azimuthal angle for the third photon, as the directions of the three photons are constrained by momentum conservation to lie in a plane, as shown in Figure 1-7. We have already chosen two of the photon directions. We define the angle between them to be ψ_3, noting that

$$\cos\psi_3 = \sin\theta \sin\theta' \cos(\phi - \phi') + \cos\theta \cos\theta'. \tag{1.16}$$

[4] In each case, one of these dimensions can be integrated away at the outset: the assumption of unpolarized initial states results in an overall ϕ symmetry.

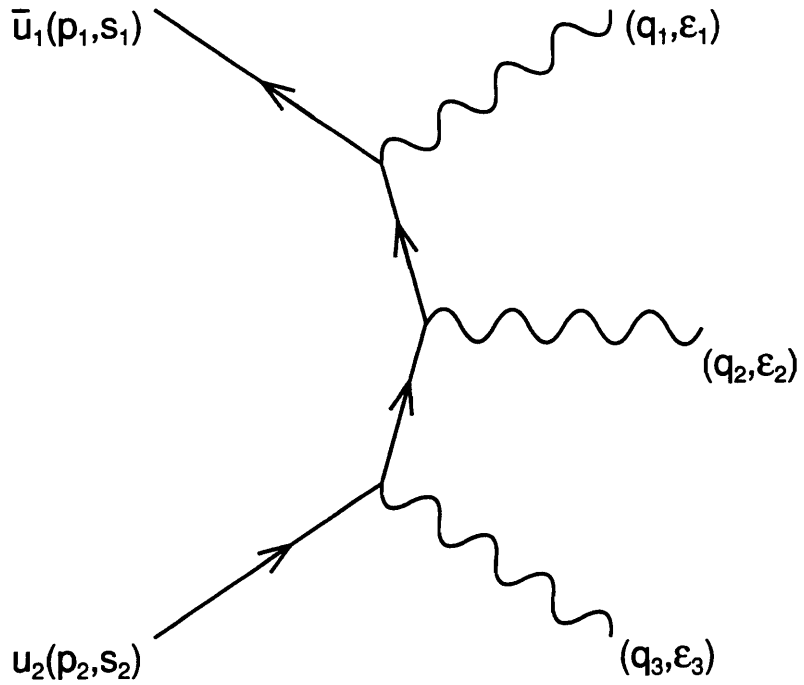

Figure 1-5: Diagram for $e^+e^- \rightarrow \gamma\gamma\gamma$.

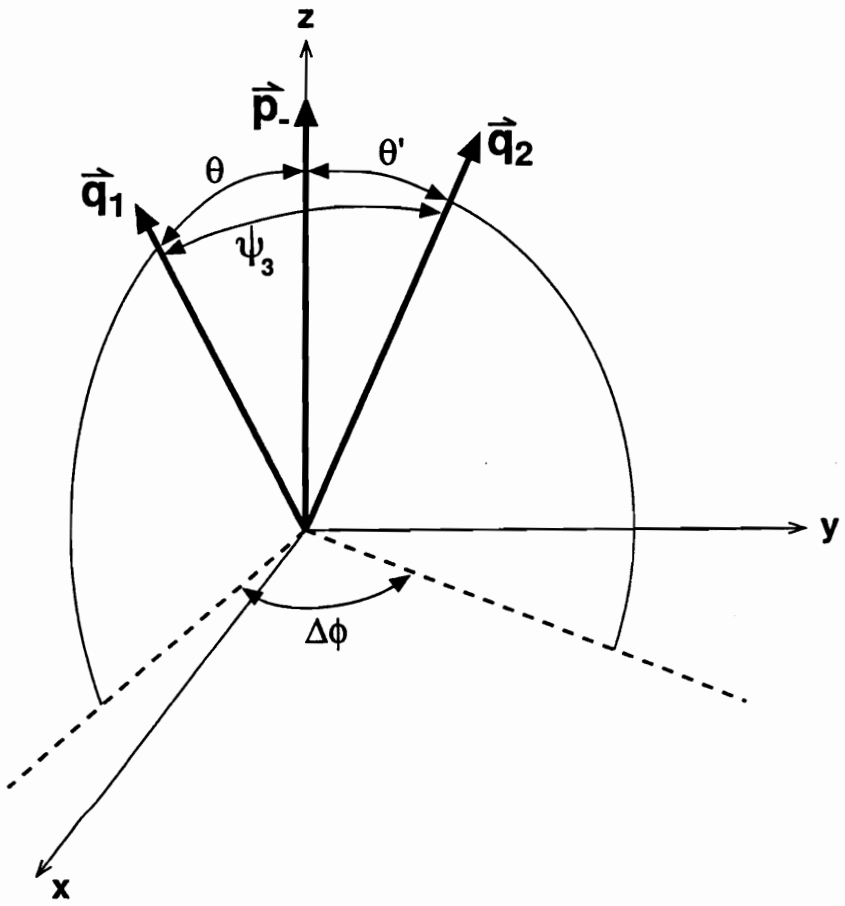

Figure 1-6: Coordinate system for $e^+e^- \to \gamma\gamma\gamma$.

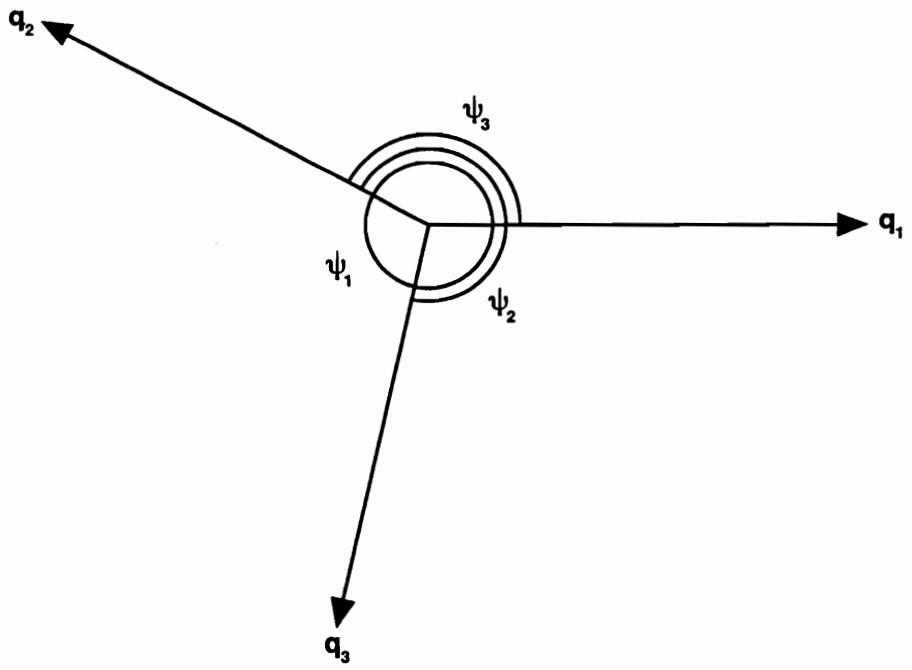

Figure 1-7: Plane containing the final state photons.

We can calculate all of the remaining quantities if we pick the energy of one of the first two photons as our fifth dimension. If we choose the energy of the first photon to be q_1, the energy of the second photon would be

$$q_2 = \frac{\sqrt{s}(2q_1 - \sqrt{s})}{2[q_1(1-\cos\psi_3) - \sqrt{s}]}, \tag{1.17}$$

where $\sqrt{s}$ is the center-of-mass energy. We need only solve the energy and momentum conservation equations to determine the energy and direction of the third photon.

We can now write down the cross section for $e^+e^- \to \gamma\gamma\gamma$:

$$\frac{d\sigma}{d\Omega d\Omega' dq_1} = \frac{\alpha^3}{8\pi^2 s}\frac{q_1 q_2}{\sqrt{s} - q_1(1-\cos\psi_3)}\tau^{3\gamma}, \tag{1.18}$$

$$\begin{aligned}\tau^{3\gamma} = {} & s\frac{(p_+q_1)^2 + (p_-q_1)^2}{(p_+q_2)(p_-q_2)(p_+q_3)(p_-q_3)} - 2\frac{m^2}{(p_+q_1)^2}\left[\frac{(p_-q_2)}{(p_-q_3)} + \frac{(p_-q_3)}{(p_-q_2)}\right] \\ & -2\frac{m^2}{(p_-q_1)^2}\left[\frac{(p_+q_2)}{(p_+q_3)} + \frac{(p_+q_3)}{(p_+q_2)}\right] + [\text{cyclic permutations in } (q_1, q_2, q_3)],\end{aligned} \tag{1.19}$$

where $d\Omega = \sin\theta\, d\theta\, d\phi$, $d\Omega' = \sin\theta'\, d\theta'\, d\phi'$, and $\tau^{3\gamma}$ is the square of the matrix element for the process $e^+e^- \to \gamma\gamma\gamma$ [14].

1.1.6 Hard Photon Emission Correction to $e^+e^- \to \gamma\gamma$

The hard photon emission contribution to the $e^+e^- \to \gamma\gamma$ cross section is derived by evaluating the q_1 and Ω' integrals in the above equation:

$$\left(\frac{d\sigma}{d\Omega}\right)^{\gamma\gamma}_{\text{hard}} = \left(\frac{d\sigma}{d\Omega}\right)^{3\gamma}_{\zeta<\zeta_c; q_3>E_{\text{soft}}; q_1,q_2>E_{\text{hard}}} = \frac{\alpha^3}{8\pi^2 s}\int dq_1\, d\cos\theta'\, d\phi' \frac{q_1 q_2}{\sqrt{s} - q_1(1-\cos\psi_3)}\tau^{3\gamma}. \tag{1.20}$$

Here we employ some kinematical restrictions to separate the $\gamma\gamma$ from the $\gamma\gamma\gamma$ cross section: ζ (the acollinearity angle of the first two photons, which is supplementary to ψ_3) is required to be less than some critical value ζ_c; q_3 is required to be greater than the soft photon energy cut $E_{\rm soft}$, and q_1 and q_2 are required to be greater than a hard photon energy cut $E_{\rm hard}$.

1.1.7 Total $\mathcal{O}(\alpha^3)$ Cross Section for $e^+e^- \to \gamma\gamma$

Now that we have calculated the individual contribution from each species of diagram, we must add them up to get the total $\mathcal{O}(\alpha^3)$ cross section for $e^+e^- \to \gamma\gamma$:

$$\begin{aligned}\left(\frac{d\sigma}{d\Omega}\right)^{e^+e^-\to\gamma\gamma}_{\zeta<\zeta_c;\, q_1,q_2>E_{\rm hard}} &= \left(\frac{d\sigma}{d\Omega}\right)^{\gamma\gamma}_{\rm Born}\cdot[1 + R_{\rm div}(E_{\rm soft},\lambda) + R_{\rm finite} + \delta_{\rm self}(\lambda) \\ &\quad + \delta_{\rm vertex}(\lambda) + \delta_{\rm box}(\lambda) + \delta_{\rm hard}(E_{\rm soft}, E_{\rm hard}, \zeta_c)] \\ &= \left(\frac{d\sigma}{d\Omega}\right)^{\gamma\gamma}_{\rm Born}\cdot(1+\delta). \end{aligned} \tag{1.21}$$

Note that the terms δ_a contain angular dependence.

1.1.8 Fate of the Infrared Divergence

As a final note, let us consider the total effect of the divergent terms in our $\mathcal{O}(\alpha^3)$ cross section. We can separate the individual terms in the cross section into finite and divergent parts:

$$\left(\frac{d\sigma}{d\Omega}\right)^{\gamma\gamma}_a = \left(\frac{d\sigma}{d\Omega}\right)^{\rm finite}_a + \left(\frac{d\sigma}{d\Omega}\right)^{\rm div}_a . \tag{1.22}$$

The individual divergent contributions to the $\mathcal{O}(\alpha^3)$ $e^+e^- \to \gamma\gamma$ cross section are given by:

$$\left(\frac{d\sigma}{d\Omega}\right)^{\rm div}_{\rm self} = \frac{\alpha^3}{2\pi s}\ln\left(\frac{\lambda^2}{m^2}\right)\left[\frac{t}{u}+\frac{u}{t}\right], \tag{1.23}$$

$$\left(\frac{d\sigma}{d\Omega}\right)^{\rm div}_{\rm vertex} = -\frac{\alpha^3}{2\pi s}2\ln\left(\frac{\lambda^2}{m^2}\right)\left[\frac{t}{u}+\frac{u}{t}\right], \tag{1.24}$$

$$\left(\frac{d\sigma}{d\Omega}\right)^{\rm div}_{\rm box} = \frac{\alpha^3}{2\pi s}2\ln(b)\ln\left(\frac{m}{\lambda}\right)\left[\frac{t}{u}+\frac{u}{t}\right], \tag{1.25}$$

$$\left(\frac{d\sigma}{d\Omega}\right)^{\rm div}_{\rm soft} = \frac{\alpha^3}{2\pi s}2\left[\rho-1\right]\ln\left(\frac{2E_{\rm soft}}{\lambda}\right)\left[\frac{t}{u}+\frac{u}{t}\right]. \tag{1.26}$$

If we rearrange things to put the logarithmic terms in the same order of λ, and keep only the terms containing λ, we see that

$$\left(\frac{d\sigma}{d\Omega}\right)^{\rm div}_{\rm total} = -\frac{\alpha^3}{2\pi s}\left\{\ln\left(\frac{\lambda^2}{m^2}\right)+\ln(b)\ln\left(\frac{\lambda^2}{m^2}\right)+\left[\rho-1\right]\ln\left(\frac{\lambda^2}{m^2}\right)\right\}\cdot\left[\frac{t}{u}+\frac{u}{t}\right]. \tag{1.27}$$

Recalling that

$$b = \frac{1-a}{1+a} = \frac{s}{2m^2}-\frac{s}{2m^2}\sqrt{1-\frac{4m^2}{s}}-1, \tag{1.28}$$

and noting, to $\mathcal{O}(m^4)$, that

$$\sqrt{1-\frac{4m^2}{s}} \simeq 1-\frac{2m^2}{s}-\frac{2m^4}{s^2}, \tag{1.29}$$

the divergent part of the cross section becomes

$$\left(\frac{d\sigma}{d\Omega}\right)^{\rm div}_{\rm total} = -\frac{\alpha^3}{2\pi s}\left\{1+\ln\left[\frac{s}{2m^2}\left(\frac{2m^2}{s}+\frac{2m^4}{s^2}\right)-1\right]+\rho-1\right\}\ln\left(\frac{\lambda^2}{m^2}\right)\cdot\left[\frac{t}{u}+\frac{u}{t}\right]$$

$$= 0. \tag{1.30}$$

The infinite contributions from the virtual corrections exactly cancel the infinite contribution from soft real photon emission.[5] The fictitious photon mass λ, having disappeared entirely from our equations, can be safely set to zero. The structure is complete; never mind that the roof hovered in midair while the foundation was being laid!

1.2 Unstable Photinos in Supersymmetric Models

A leading candidate in the search for higher symmetries beyond the Standard Model is supersymmetry (SUSY), which demands symmetry between the fundamental fermions and bosons [15]. It would be expressed in physical particles as a discrete, conserved charge known as R-parity. All currently known fundamental particles are defined to have even R-parity. SUSY postulates that for each state of even R-parity there would be a state of odd R-parity. These odd R-parity—or supersymmetric—states would share exactly the same properties as their even R-parity partners, save for having one half-integer less intrinsic spin.

The fundamental fermions and bosons do not form mass-degenerate doublets, however, so if SUSY exists it must be deeply broken. R-parity must be conserved, so SUSY states cannot decay solely into conventional particles. It therefore follows that the lightest SUSY particle (LSP) must be stable. Furthermore, cosmological considerations show that the LSP must be massless, or very nearly so [16].

Many explicit SUSY models assume that the photino (the SUSY partner to the photon, denoted $\tilde{\gamma}$) is massless, that it is the LSP, and that it is therefore stable. Accordingly, most experimental searches for evidence of SUSY take this as a starting assumption. It has been shown, however, that in spontaneously broken models where the photino is massive, the photino is necessarily *unstable*, and decays into a photon and a Goldstino ($\tilde{G}$) [18].

[5] The alert reader will notice that the series expansion in equation 1.30 could be continued to higher order in m, reviving the divergence. These terms, however, will be cancelled by terms in the higher order real and virtual corrections.

The two tree-level diagrams for photino pair production are shown with the photino decay diagram in Figure 1-8. The interaction is mediated by the exchange of a scalar electron (or selectron, denoted $\tilde{e}$), the superpartner to the electron. The differential cross section for this process is:

$$\frac{d\sigma}{dx} = \frac{1}{4}\pi\alpha^2 s\beta^3 \frac{k^2(1+x^2) - s(2k - m_{\tilde{\gamma}}^2 - s/4)x^2 + s^2\beta^2 x^4/4}{(k^2 - s^2\beta^2 x^2/4)^2}, \tag{1.31}$$

where $k = M(\tilde{e})^2 - M(\tilde{\gamma})^2 + s/2$, β is the velocity of the photino ($\tilde{\gamma}$), and $x = \cos\theta_{\tilde{\gamma}}$ (see, for example, [19] or [20]).

The subsequent decay of the photino is given by the effective Lagrangian

$$\mathcal{L}_{\text{eff}} = -\frac{1}{2d}\bar{\psi}_{\tilde{G}}\sigma_{\mu\nu}\,\partial\!\!\!/\,[F^{\mu\nu}\psi_{\tilde{\gamma}}] + \text{h.c.}, \tag{1.32}$$

and the lifetime for decay by this process is given by

$$\tau_{\tilde{\gamma}\to\gamma\tilde{G}} = \frac{8\pi d^2}{M_{\tilde{\gamma}}^5}, \tag{1.33}$$

where d is the square of the SUSY breaking scale. Clearly, if this scale is too large and the photino mass is too light, the lifetime will be too long to observe the decay.

Events from this process would typically appear as an acoplanar pair of photons in the barrel region of the detector, with the Goldstinos remaining undetected. Here we define acoplanarity to be $\xi = |180° - \Delta\phi|$, where $\Delta\phi$ is the azimuthal opening angle between the photons.

The primary background for the detection of this acoplanar $\gamma\gamma$ signature is $e^+e^- \to (\gamma)\gamma\gamma$, where one of the photons remains undetected. The background process $e^+e^- \to (e^+e^-)\gamma\gamma$ (where the final state e^+ and e^- escape detection) has a smaller production cross section,

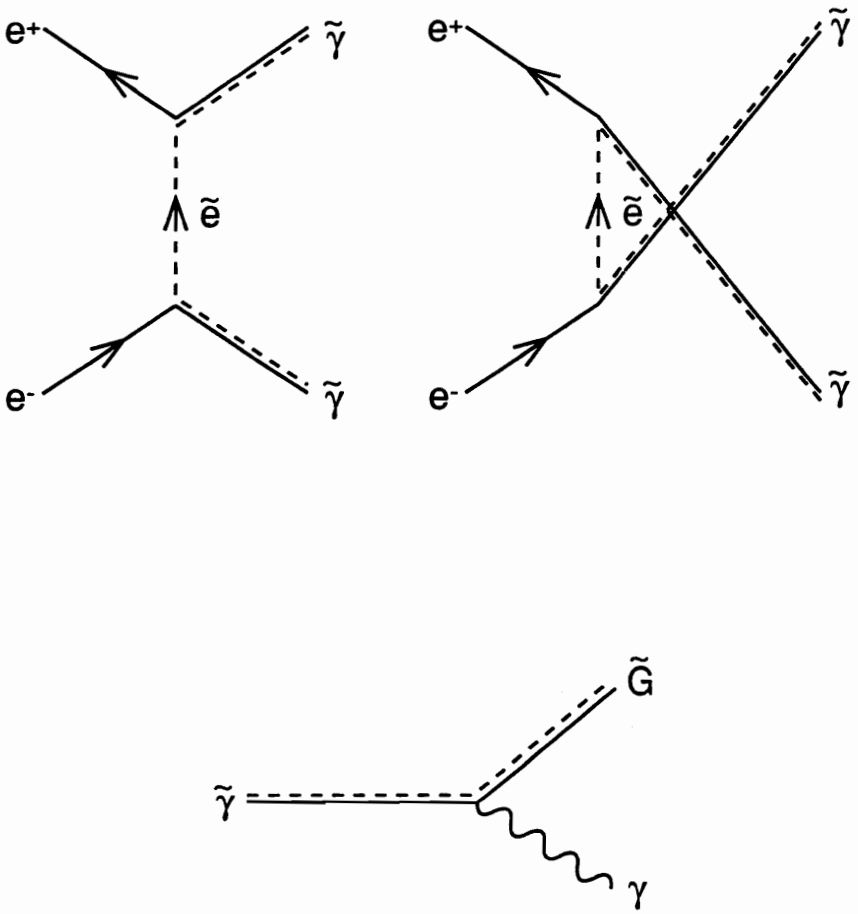

Figure 1-8: Diagrams for $e^+e^- \rightarrow \tilde{\gamma}\tilde{\gamma}$ and subsequent decay.

but it has more phase space available to produce the signature. The smallest (yet the most difficult to remove) background process is $e^+e^- \rightarrow (\nu\bar{\nu})\gamma\gamma$.

Supergravity Models

So far we have considered SUSY only as a global symmetry. If we impose SUSY as a spontaneously broken local symmetry (known as supergravity, or SUGRA) the super-Higgs mechanism eliminates the goldstino by bequeathing its degrees of freedom to the gravitino ($\tilde{G}_{3/2}$), the spin 3/2 partner to the graviton. The phenomenological properties of the gravitino are identical to those of the goldstino, except that the gravitino acquires a mass $M_{\tilde{G}_{3/2}} = \sqrt{4\pi G/3}\, d$, where G is the Newtonian gravitational constant [21].

1.3 The Effects of Composite Models

A simple method for extending physics beyond the Standard Model (indeed, one that has worked before) is the conjecture that the known "fundamental" fermions are actually composed of smaller particles, known as preons. The great advantage of these composite models is that they manifestly exhibit the numerous quark-lepton symmetries that are observed in nature, symmetries that are imposed in an ad-hoc manner in the Standard Model.

Several explicit models have been advanced as to the form of the inter-preon interaction. Regardless of the form of this interaction, however, the general aspect of electron compositeness would distort the $e^+e^- \rightarrow \gamma\gamma$ spectrum in a characteristic way: the nontrivial electron form factor would lead, at the onset of the effects of compositeness, to an electron contact interaction.

Electron compositeness is one possible answer to a long-standing question about QED: is it a fundamentally finite theory, and are the infinite quantities hidden by renormalization theory

physically meaningless? Divergences follow directly from the assumed point-like nature of electrons and photons; a finite theory would imply that there is some fundamental length over which the interaction is smoothed out [22]. At a high enough energy scale (called the QED cutoff scale, denoted Λ), the effects of this smearing would become apparent.

We can represent the effects of the QED cutoff scale by assigning a form factor to the electron propagator. The cross section for this process to lowest order in Λ would have the form

$$\frac{d\sigma}{d\Omega} = \frac{\alpha^2}{s}\frac{1+\cos^2\theta}{1-\cos^2\theta}\left[1 \pm \frac{s^2}{2\Lambda_{\pm}^4}\left(1-\cos^2\theta\right)\right]. \tag{1.34}$$

The QED cutoff model is theoretically disfavored, because it does not exhibit chiral invariance. We can approach electron compositeness in a chirally invariant way by introducing an additional diagram (Figure 1-9) into the perturbative expansion at the tree level, representing an $ee\gamma\gamma$ contact interaction. The Lagrangian for this process has the form:

$$\mathcal{L}_{e^+e^-\gamma\gamma} = \frac{2ie^2}{\Lambda^4} F^{\mu\sigma} F_{\sigma}{}^{\nu} \sum_{j=L,R} \eta_j \bar{\psi}_j \gamma_\mu \partial_\nu \psi_j \tag{1.35}$$

where L, R denote left- and right-handed chirality, Λ is a mass scale factor which characterizes the inter-preon interaction, and $\eta_{L,R} = \pm 1$ or 0 describes the coupling to the L, R chirality states.

The $\mathcal{O}(\alpha^2)$ $e^+e^- \rightarrow \gamma\gamma$ cross section in the absence of transverse beam polarization then becomes [23]:

$$\left(\frac{d\sigma}{d\Omega}\right)_{e^+e^-\rightarrow\gamma\gamma} = \frac{\alpha^2}{2s}\left\{\frac{1+\cos^2\theta}{1-\cos^2\theta}\left[\left(1+\frac{\eta_L s^2}{4\Lambda^4}\sin^2\theta\right)^2 + \left(1+\frac{\eta_R s^2}{4\Lambda^4}\sin^2\theta\right)^2\right]\right\}, \tag{1.36}$$

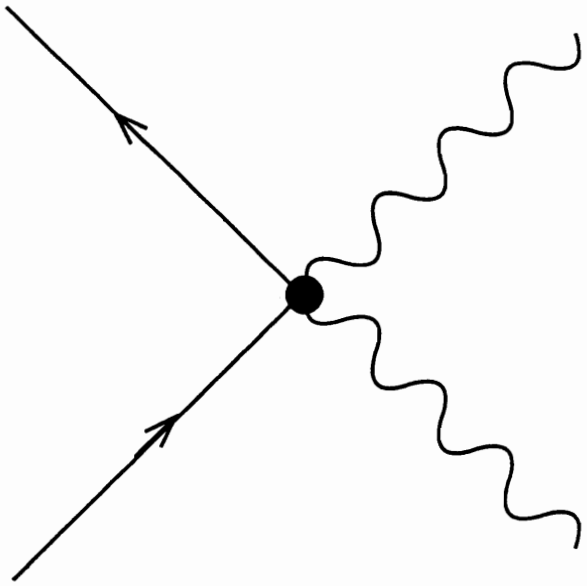

Figure 1-9: Contact diagram for $e^+e^- \rightarrow \gamma\gamma$.

where Λ is determined by η_L and η_R. There are eight representative cases for Λ:

$$\begin{aligned}
\Lambda = \Lambda_{\pm}^{L} \quad & \text{for } (\eta_L, \eta_R) = (\pm 1, 0) \\
\Lambda_{\pm}^{R} \quad & \text{for } (\eta_L, \eta_R) = (0, \pm 1) \\
\Lambda_{\pm}^{L+R} \quad & \text{for } (\eta_L, \eta_R) = (\pm 1, \pm 1) \\
\Lambda_{\pm}^{L-R} \quad & \text{for } (\eta_L, \eta_R) = (\pm 1, \mp 1).
\end{aligned} \tag{1.37}$$

1.3.1 Excited Electron Intermediate State

Traditionally, the search for electron compositeness centers on the effects of an excited electron (e^*), wherein the preons have assumed an orbitally excited state. Such a state would be much heavier than the electron, and decay via $e^* \rightarrow e\gamma$. This interaction would add two additional tree-level diagrams to the $e^+e^- \rightarrow \gamma\gamma$ process. These diagrams would be identical to the diagrams in Figure 1-1, but mediated by the exchange of an e^* in the intermediate state.

The cross section for $e^+e^- \rightarrow \gamma\gamma$ with an unpolarized initial state, including the e^* exchange diagrams, would be given by a special case of Equation 1.36:

$$\begin{aligned}
\left(\frac{d\sigma}{d\Omega}\right)_{\gamma\gamma} = \frac{\alpha^2}{4s} \Bigg\{ & \frac{(1+\cos\theta)^2}{1-\cos^2\theta} \left[\left(1 + \frac{(\eta_{e^*}^L)^2 s^2 \sin^2\theta}{4\Lambda_{e^*}^2 (m_{e^*} - u)} \right)^2 \left(1 + \frac{(\eta_{e^*}^R)^2 s^2 \sin^2\theta}{4\Lambda_{e^*}^2 (m_{e^*} - u)} \right)^2 \right] \\
+ & \frac{(1-\cos\theta)^2}{1-\cos^2\theta} \left[\left(1 + \frac{(\eta_{e^*}^L)^2 s^2 \sin^2\theta}{4\Lambda_{e^*}^2 (m_{e^*} - t)} \right)^2 \left(1 + \frac{(\eta_{e^*}^R)^2 s^2 \sin^2\theta}{4\Lambda_{e^*}^2 (m_{e^*} - t)} \right)^2 \right] \Bigg\},
\end{aligned} \tag{1.38}$$

where

$$\begin{aligned}
\Lambda_{e^*} = \Lambda_{e^*}^{L} \quad & \text{for } (\eta_{e^*}^L, \eta_{e^*}^R) = (1, 0) \\
\Lambda_{e^*}^{R} \quad & \text{for } (\eta_{e^*}^L, \eta_{e^*}^R) = (0, 1).
\end{aligned} \tag{1.39}$$

If we assume that $m_{e^*}^2 \gg s$, we note that

$$\begin{aligned} (\Lambda_+^{\rm L})^2 &= \Lambda_{e^*}^{\rm L} m_{e^*} \\ (\Lambda_+^{\rm R})^2 &= \Lambda_{e^*}^{\rm R} m_{e^*}. \end{aligned} \tag{1.40}$$

Note that the heavy excited electron propagator demonstrates only two of the eight contact interaction patterns. It merits our attention, however, since the effects of an excited electron can appear in many other signatures, and our results can be more easily combined with previous limits. We should also remark that the overall sign of the interaction is not observable, i.e. that $(\eta_{e^*}^{\rm L}, \eta_{e^*}^{\rm R}) = (-1, 0)$ is indistinguishable from $(\eta_{e^*}^{\rm L}, \eta_{e^*}^{\rm R}) = (1, 0)$.

Chapter 2

TRISTAN and AMY

2.1 TRISTAN

TRISTAN [24] is a colliding beam electron-positron storage ring located at KEK, the National Laboratory for High Energy Physics in Tsukuba, Japan. This accelerator, commissioned in October, 1986, produces collisions at interaction points in four experimental halls. Three general-purpose physics experiments, AMY, VENUS, and TOPAZ, are currently in progress (SHIP, a special-purpose experiment designed to search for heavily ionizing particles, was completed in 1989). Before the SLC and LEP accelerators came online in 1989, TRISTAN was the highest-energy e^+e^- collider in the world.

TRISTAN consists of four accelerator subsystems, shown in Figure 2-1: the positron generator, the Linear Accelerator (LINAC), the Accumulation Ring (AR), and the Main Ring (MR). Electron beams are initially produced at 30 MeV by a Van de Graaf accelerator; positron beams are produced by a 200 MeV electron beam incident upon a tantalum target. The resulting electron (positron) beam is accelerated to an energy of 2.5 GeV by the LINAC, and stored in the AR. When a current of 10 mA is achieved, the beam is accelerated by the AR to an energy of 8 GeV, and then injected into the MR. When two bunches

each of electrons and positrons are stored in the MR, the beam is then accelerated to the collision energy.

The sustained operation of TRISTAN commenced in May, 1987 [25]. Beams in the MR were accelerated by 64 nine-cell APS cavities[1] located in the straight sections around the Fuji and Tsukuba experimental halls, providing a maximum beam energy of 26 GeV. During the summer shutdown of 1987, 40 more cavities were installed around the Oho experimental hall. This provided a maximum beam energy of 28 GeV. In the summer of 1988, 16 five-cell superconducting cavities were installed around the Nikko experimental hall, providing a maximum beam energy of 30.7 GeV. The final cavity upgrade came in the summer of 1989, with the addition of 16 superconducting cavities around Nikko Hall. In November, 1989, TRISTAN achieved its maximum energy of 32 GeV per beam.

During the summer shutdown of 1990, superconducting quadrupole magnets (QCS) were installed at every interaction region. The improved focusing resulted in roughly a factor of two increase in luminosity. Since that upgrade, TRISTAN has achieved a sustained luminosity of $1\,\mathrm{pb}^{-1}$ per day per interaction point at $\sqrt{s} = 58\,\mathrm{GeV}$.

TRISTAN's RF cavities operate at a frequency of 508.58 MHz, which produces 5120 standing electromagnetic waves around the 3018.08 m circumference of the MR. Only four of these contain electron or positron bunches at any one time.

2.2 The AMY Detector

AMY is a general-purpose particle spectrometer, located in the Oho experimental hall of TRISTAN [26]. Momentum resolution is provided by a 3 Tesla superconducting magnetic solenoid. This high field allows AMY to be smaller in size than many detectors with similar capabilities.

[1] APS stands for "Alternating Periodic Structure". These are conventional (i.e. non-superconducting) RF cavities composed of alternately placed long and short cells. This arrangement improves acceleration efficiency.

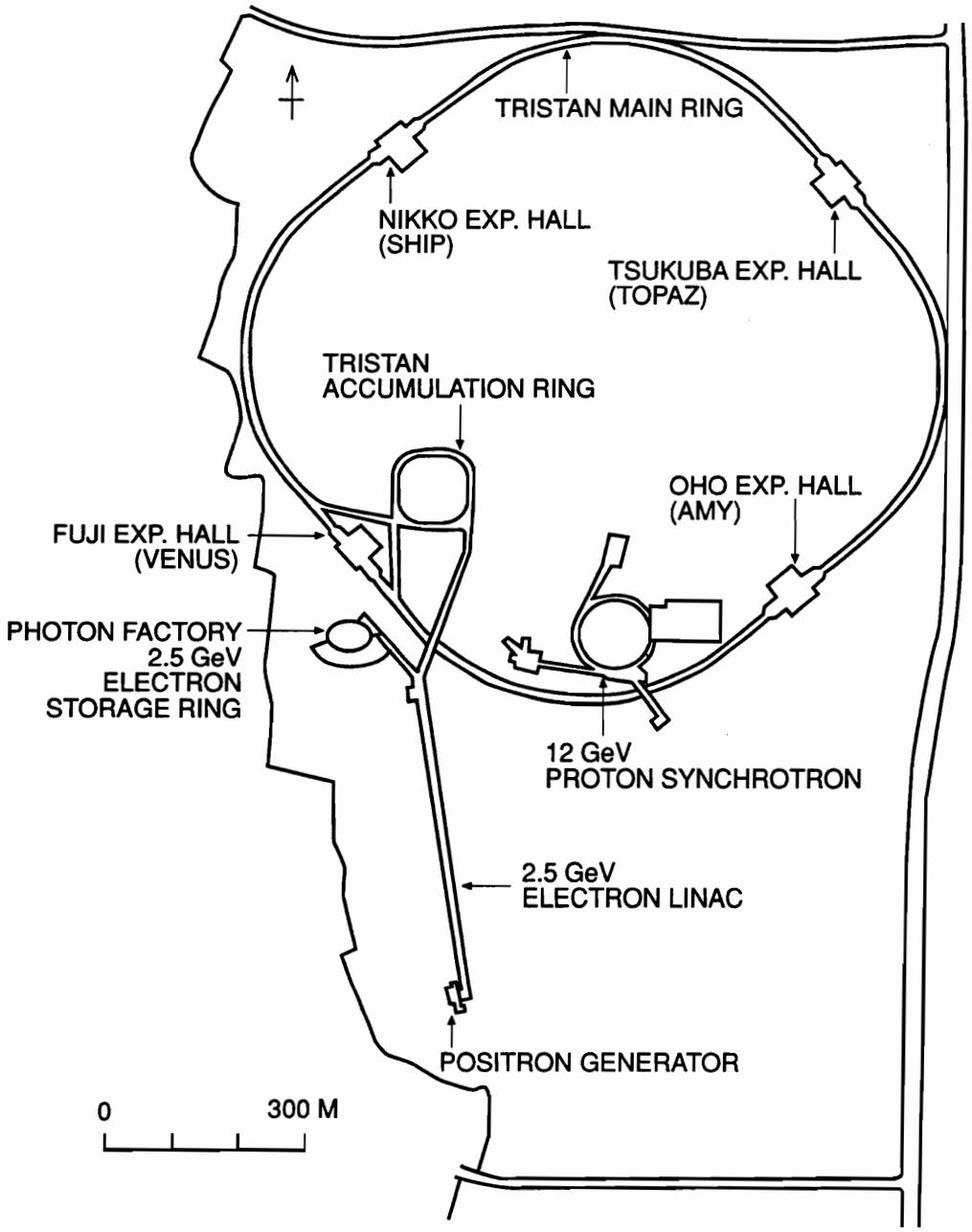

Figure 2-1: Overview of the TRISTAN accelerator complex.

The original design of AMY, now called AMY 1.0, is shown in Figure 2-2. Two detectors, the Inner Tracking Chamber (ITC) and the Central Drift Chamber (CDC), were used for tracking charged particles. Electromagnetic calorimetry was performed by the barrel Shower Counter (SHC). The region between the CDC and the SHC was filled with trigger scintillation counters. Muon identification was performed by the Muon Detector (MUO), located outside the magnetic yoke. The Pole Tip Shower Counter (PTC) and the Ring Veto Counter (RVC) covered the endcap regions. The small angle Luminosity Monitor (LUM) was fixed to the beam pipe outside of the endcaps. The beam pipe was 23 cm in diameter, and was composed of 1.5 mm thick aluminum with an inner liner made of copper.

The detector was upgraded to AMY 1.5 (shown in Figure 2-3) in the summer of 1989. Changes included the replacement of the endcaps, along with the PTC and RVC, with endcaps covered by two new detectors, the Endcap Shower Counter (ESC) and the Forward Tracking Chamber (FTC). The X-Ray Detector (XRD), inserted between the CDC and the SHC, was designed for the identification of electrons. The LUM was replaced by a similar detector, the Small Angle Counter (SAC). A new tracking chamber, the Vertex Detector (VTX), was installed after the 1990 run period in the barrel region inside the ITC. The VTX was mounted on a new beryllium beam pipe of 1 mm thickness and 9.5 cm diameter.[2] Finally, a new triggering system was installed.

The most important detectors for this thesis are the calorimeter and the endcap calorimeters and tagging counters; these will be described in detail. Tracking and muon detectors are used primarily for the rejection of backgrounds; a detailed description of these detectors would, as Gibbon would say, be devoid of both instruction and amusement.

2.2.1 The AMY Coordinate System

The coordinate system for the AMY detector is as follows:

[2]During the fall, 1989 run period, a prototype VTX (known as the pVTX) was installed with a new aluminum beam pipe of 1 mm thickness and 10 cm diameter. The old 23 cm aluminum beam pipe was used without the VTX during the 1990 run period.

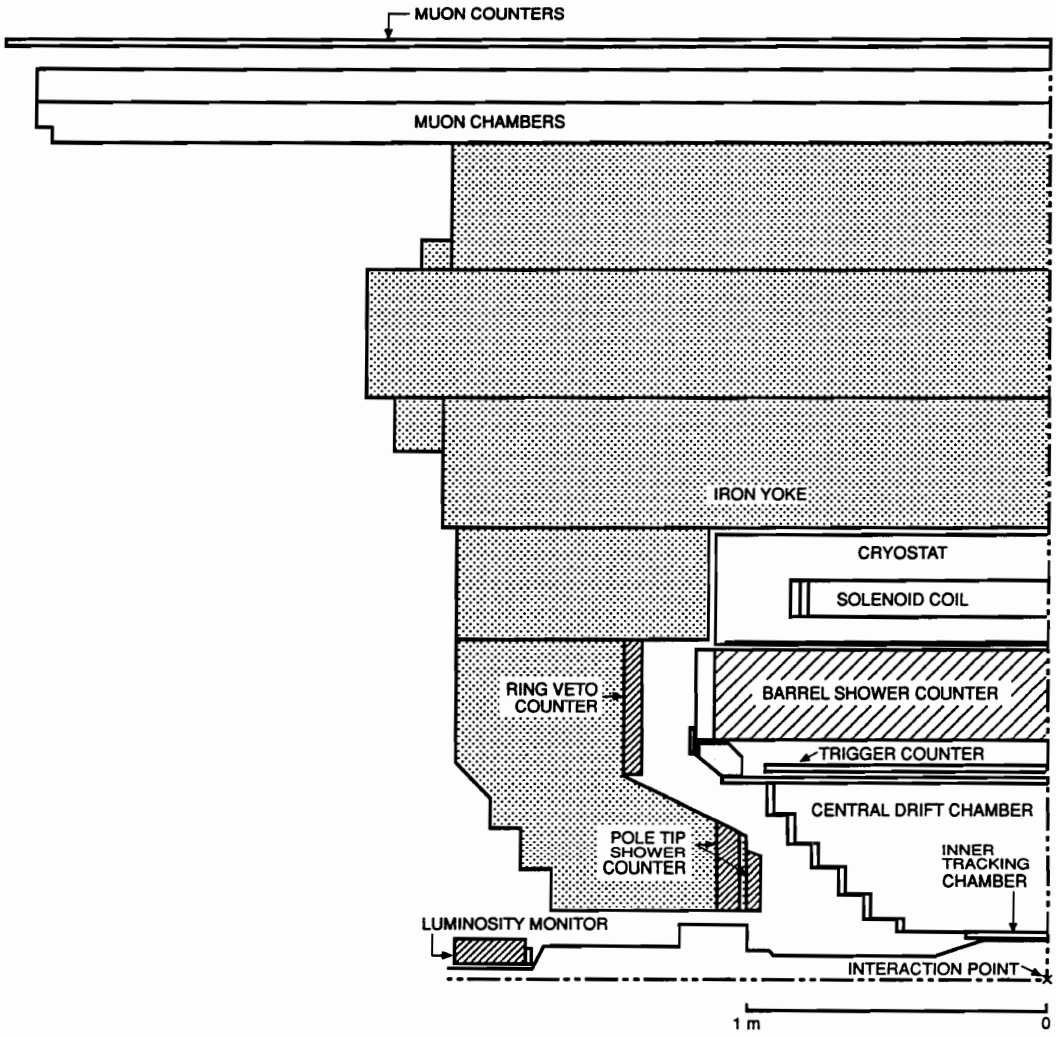

Figure 2-2: Cutaway view of AMY 1.0.

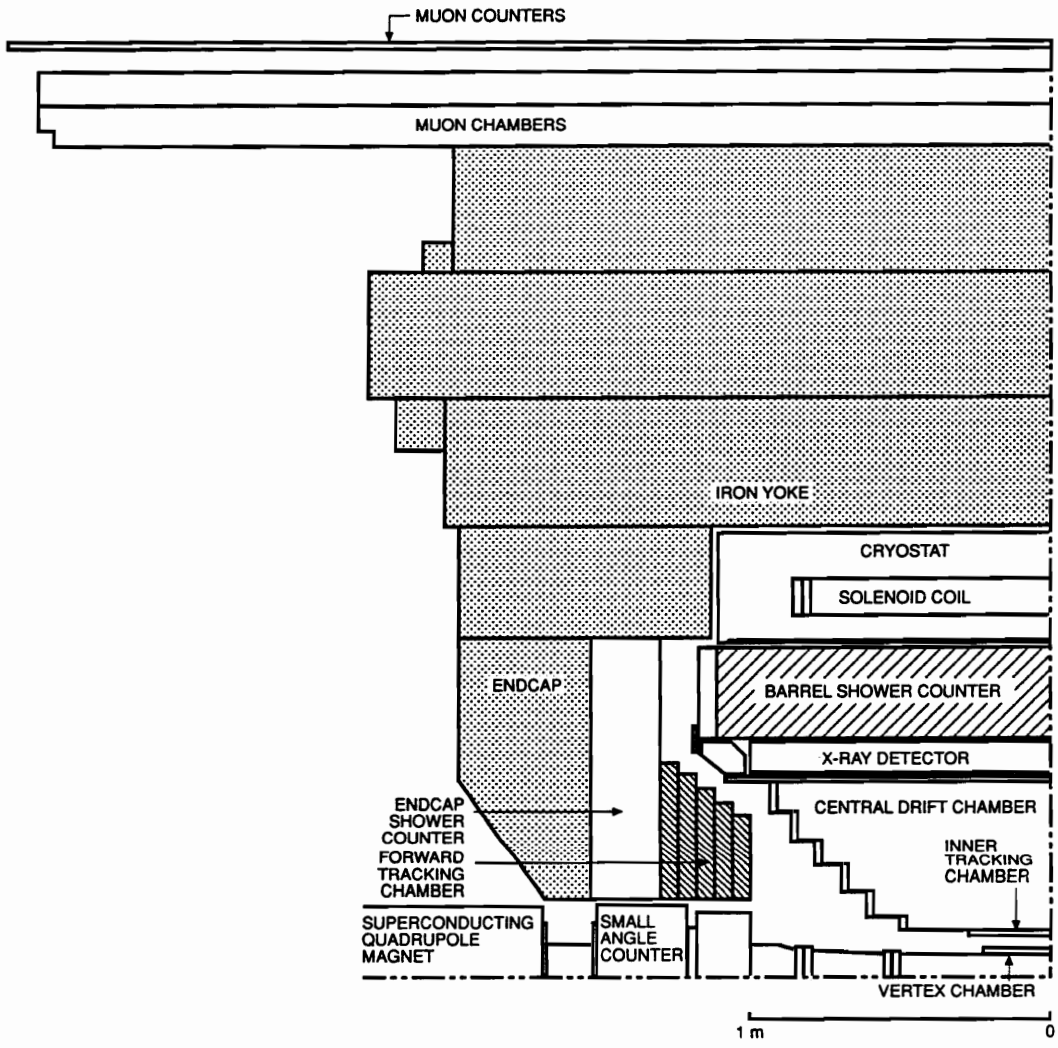

Figure 2-3: Cutaway view of AMY 1.5.

- The $+z$ direction is defined as the direction of electron bunches in TRISTAN, which travel clockwise as they move around the Main Ring.
- The $+x$ direction is defined as pointing horizontally away from the center of the TRISTAN MR.
- The $+y$ direction is defined as pointing upwards.
- θ angles are measured from the $+z$ axis.
- ϕ angles are measured clockwise from the $+x$ axis, as viewed from the $+z$ direction (i.e. looking in the $-z$ direction).
- "Fuji" side is the side of the detector in the $+z$ direction from the interaction point.
- "Tsukuba" side is the side of the detector in the $-z$ direction from the interaction point.

2.2.2 The Superconducting 3T Magnet and Yoke

The 3 Tesla magnetic field used to measure charged particle momenta is produced by a superconducting solenoid. The solenoid is housed in a cryostat filled with liquid helium at 4.4 K. The operating current is 5 kA [27].

The magnetic yoke, a hexagonal block of iron weighing 650 metric tons, serves several purposes for AMY. First, it provides flux return for the superconducting solenoid. Second, it provides the main structural support for the detector components. Third, it acts as a hadron filter for the muon detector.

The original design of AMY 1.0 called for a very low-β insertion magnet to be positioned very close to the interaction region. While this would have provided much better luminosity, these quadrupoles would have to be removed every time the endcaps were retracted to provide access. The quadrupole magnets could not, therefore, be used to support the beam

pipe and the ITC. To rectify this problem, it was decided that the pieces of the endcaps below the beam pipe on either side would remain fixed. These were called the endcap keys.

In order to improve the flux return for the AMY solenoid, and thus shield the low-β quadrupole from the intense magnetic field, the AMY 1.0 endcaps were indented near the beam axis. Unfortunately, this inner bulge reduced the space available for detectors: the PTC had to be split into two sections, and the RVC could only be 5 cm thick.

When the QCS magnets were installed, they were not placed as close to the interaction point as in the original design. This arrangement eliminated the need for an indented endcap; it also left "enough" room to retract the endcaps without removing the quadrupoles, obviating the need for a key. These design flexibilities are reflected in the AMY 1.5 endcaps [28].

The AMY 1.5 endcaps are 40 cm thick, compared to 55 cm for the AMY 1.0 endcaps. This provides more space for detector elements, but degrades the magnetic field somewhat. The magnetic field at the center of AMY 1.5 is 2.872 T, compared with 3.040 T for AMY 1.0. The uniformity of the field also suffers from the lack of an indented endcap.

2.2.3 The Inner Tracking Chamber (ITC)

The Inner Tracking Chamber [29] (ITC) is a straw chamber composed of 576 aluminized polycarbonate tubes arranged in four layers. This detector provides charged particle tracking in the transverse plane from a radius of 12.2 cm to 14.2 cm with a coverage from -27.5 cm to 27.5 cm in z. Each tube has an anode wire at its center, held at a voltage of 1.75 kV in an argon-ethane atmosphere (50% Ar, 50% C_2H_6 at 1.46 atm). The tube diameters increase from 0.53 cm at the innermost layer to 0.59 cm at the outermost layer. Each layer of 144 tubes is offset from adjacent layers by 1.25° in ϕ. The spatial resolution of the ITC is 80 μm.

2.2.4 The Central Drift Chamber (CDC)

The Central Drift Chamber [30] (CDC) is the main detector for tracking charged particles. Its fiducial coverage extends from 15.5 cm to 64.0 cm in cylindrical radius, with 2π coverage in ϕ. Coverage in θ starts at $|\cos\theta| \leq 0.87$ for the innermost layers, decreasing to $|\cos\theta| \leq 0.80$ for the outermost layers.

The CDC is composed of 25 layers of axial sense wires and 15 layers of stereo sense wires, banded into 6 axial and 5 stereo disks. The 9048 sense (or anode) wires are held at 1.8 kV in an atmosphere of HRS gas (89% Ar, 10% CO_2, 1% CH_4).[3] They are composed of 50 μm diameter gold-coated tungsten. The 22994 field shaping (or cathode) wires are grounded, and are composed of 160 μm diameter gold-coated aluminum.

The axial wires run parallel to the z-axis, and provide r-ϕ information with a spatial resolution of 125 μm. The stereo wires are canted at angles with respect to the z-axis, ranging from 4.1° in the first stereo disk to 4.9° in the fifth stereo disk. These stereo angles provide z information with a resolution ranging from 2.1 mm in the first stereo disk to 1.8 mm in the fifth stereo disk for well-separated tracks.

2.2.5 Trigger Scintillation Counters

The region between $r = 64$ cm and $r = 79$ cm was intended for the X-Ray Detector. Because this detector was not ready for installation in AMY 1.0, twelve scintillation counters (never graced with an acronym) were installed in its stead. These were intended to provide additional triggering capability, by (for example) correlating back-to-back hits.

[3] For the 26.73 pb^{-1} of data taken in 1990, the sense wires were held at a voltage of 2.1 kV in a neon-ethane atmosphere (50% Ne, 50% C_2H_6).

2.2.6 The Barrel Shower Counter (SHC)

The Barrel Electromagnetic Calorimeter [31] [32], or Shower Counter (SHC), is the detector component most relevant for this thesis. It is a gas sampling calorimeter designed to emphasize the angular and longitudinal resolution, rather than energy resolution, of electromagnetic showers. This decision, we will see, was particularly useful for this thesis.

SHC Structure and Fiducial Range

The SHC, shown in Figure 2-4, occupies a cylindrical volume of 220 cm in z from a radius of 79 cm to a radius of 110 cm. Its fiducial volume covers a range of ± 0.73 in $\cos\theta$ for reliable calorimetry, although it can tag electromagnetic showers down to $|\cos\theta| \sim 0.8$.

The SHC is composed of 19 layers of lead sandwiched between 20 layers of resistive plastic proportional tubes, which run the entire z-length of the detector. The tubes have inner dimensions of 7 mm in r and 10 mm in ϕ (some tubes at sextant boundaries have a ϕ width of 7 mm). At the center of each tube is an anode wire of 20 μm gold-plated tungsten in an ionizing atmosphere. Above each layer of proportional tubes is a layer of copper-clad G-10 plastic etched with ϕ-segmented cathode pads; below each layer of tubes is another layer of G-10 with cathode pads segmented in θ. The first 15 layers of lead are each 3.5 mm thick; the last 4 layers are each 7.0 mm thick. The longitudinal structure of the SHC is shown in Figure 2-5.

The SHC is azimuthally divided into six independant, ostensibly identical chambers called sextants. The inner and outer radii of the each sextant are bounded by stainless steel plates of thickness 2.4 and 10 mm, respectively. The sides of each sextant are bounded by 0.8 mm thick stainless steel. The endplates are composed of 13 mm thick aluminum. The sextants are attached, by means of the outer plates, to two stainless steel rings called the superrings, which in turn are attached to the magnetic yoke. Ideally, the SHC remains electrically isolated from the yoke.

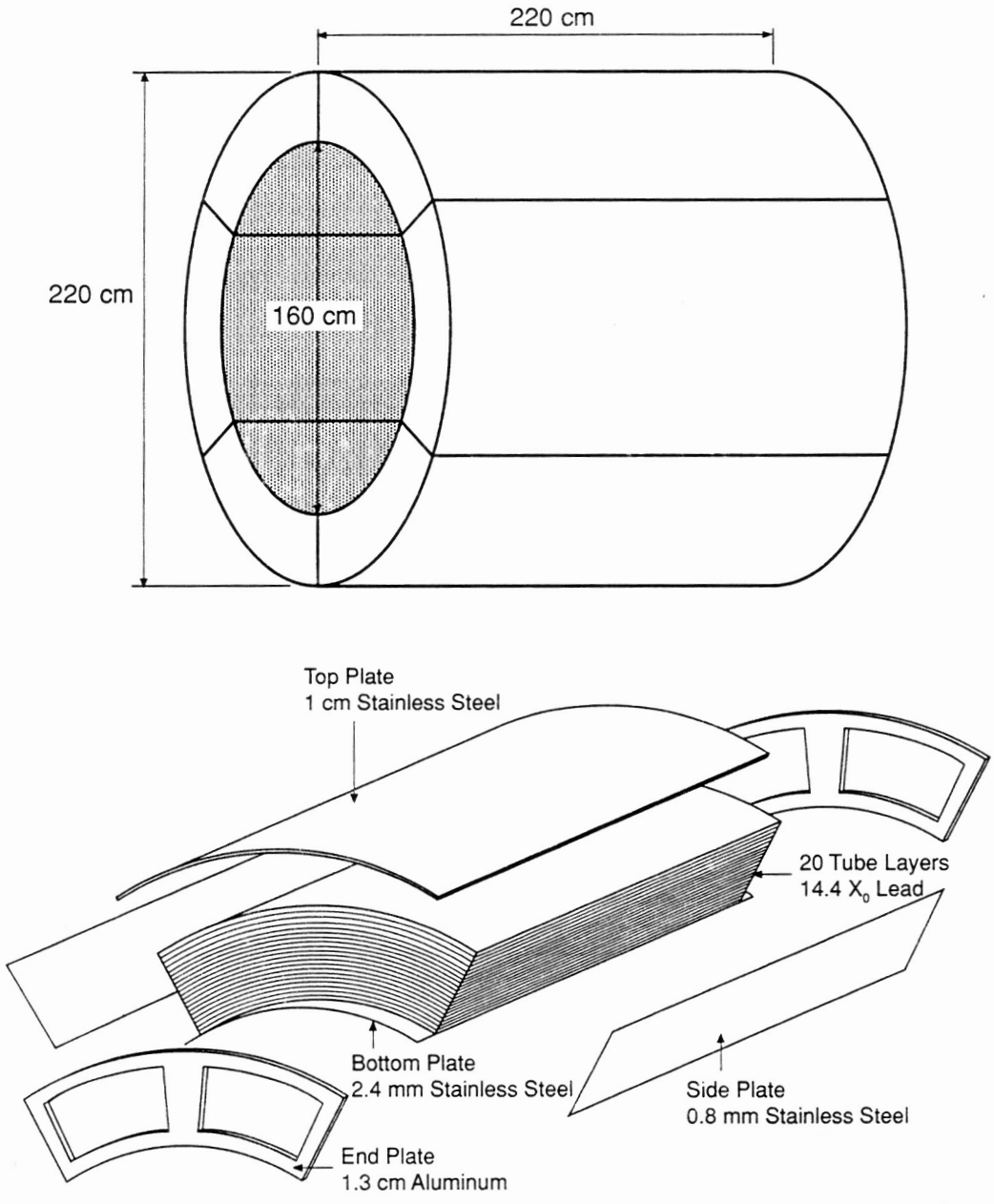

Figure 2-4: The AMY barrel shower counter.

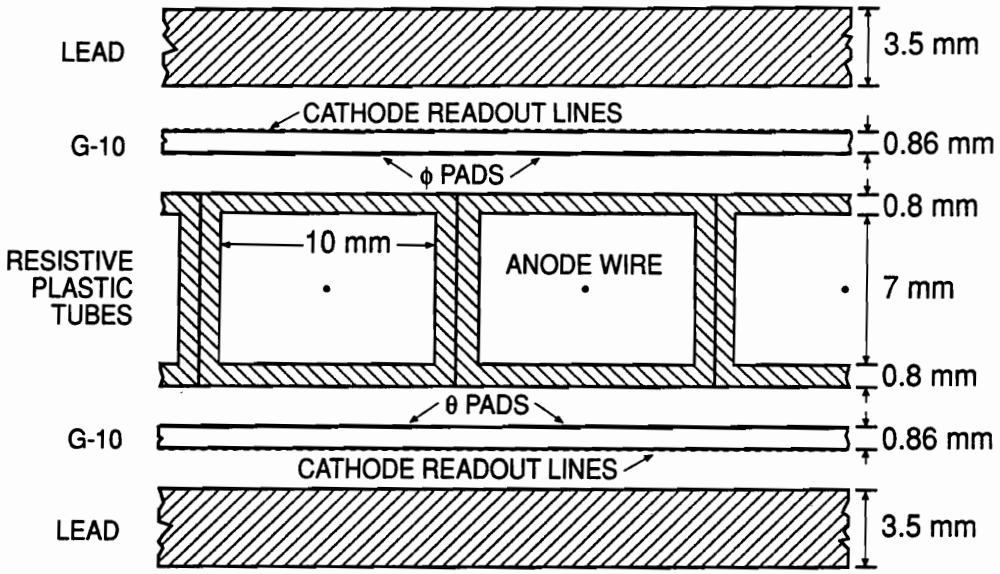

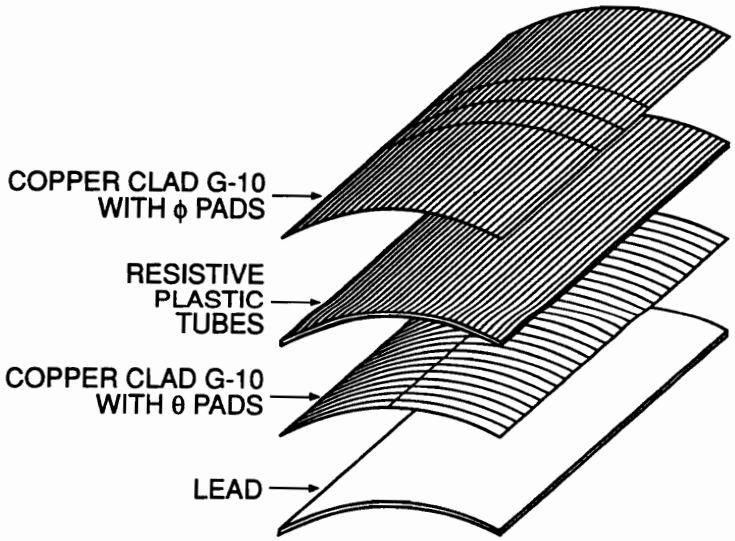

Figure 2-5: Longitudinal structure of the AMY SHC.

Environmental factors such as variations in the gas composition, pressure, and temperature are monitored by small proportional tubes similar to those in the anode layers. Each tube is painted on the inside surface with a ^{55}Fe source of 0.55 μCi. There are four such monitor tubes per sextant, with two just inside each endplate. Monitor tube gain data are read every 15 minutes during a run, and the average gain for each tube is recorded for each run.

SHC Segmentation

The anode wires of each layer in each sextant are ganged together, before readout, into 8 towers in ϕ, for a total of $20 \times 48 = 960$ anode signals. Each anode gang contains approximately 10 wires. The eight anode gangs in an anode layer are kept at operating voltage by one power supply.

The arrangement of the θ cathode pads is shown at the top of Figure 2-6. The widths of the θ pads vary in z and r, so that each pad covers a constant angular width in θ as viewed from the interaction point, i.e. they follow a projective geometry. The θ width of each pad is 0.7712° in the first 8 layers; the pads in the last 12 layers have twice this width. Each θ pad covers a ϕ range of 30°.

The arrangement of the ϕ cathode pads is shown at the bottom of Figure 2-6. Each ϕ pad covers an angular width of 0.9367° in ϕ for the first 8 layers, twice as much for the last 12 layers. The θ range is covered by four phi pads, with breaks at $\theta = 68.42°$, 90.0°, and 111.58°.

Each ϕ pad, along with any θ pad intersecting it, is contained within a rectangular area called a θ-ϕ block (also called a division). There are 8 such blocks in each sextant (2 in ϕ by 4 in θ). Each ϕ (θ) pad intersects every θ (ϕ) pad in its block, and none other.

SHC Numbering Scheme

The numbering scheme for the various SHC segments is as follows:

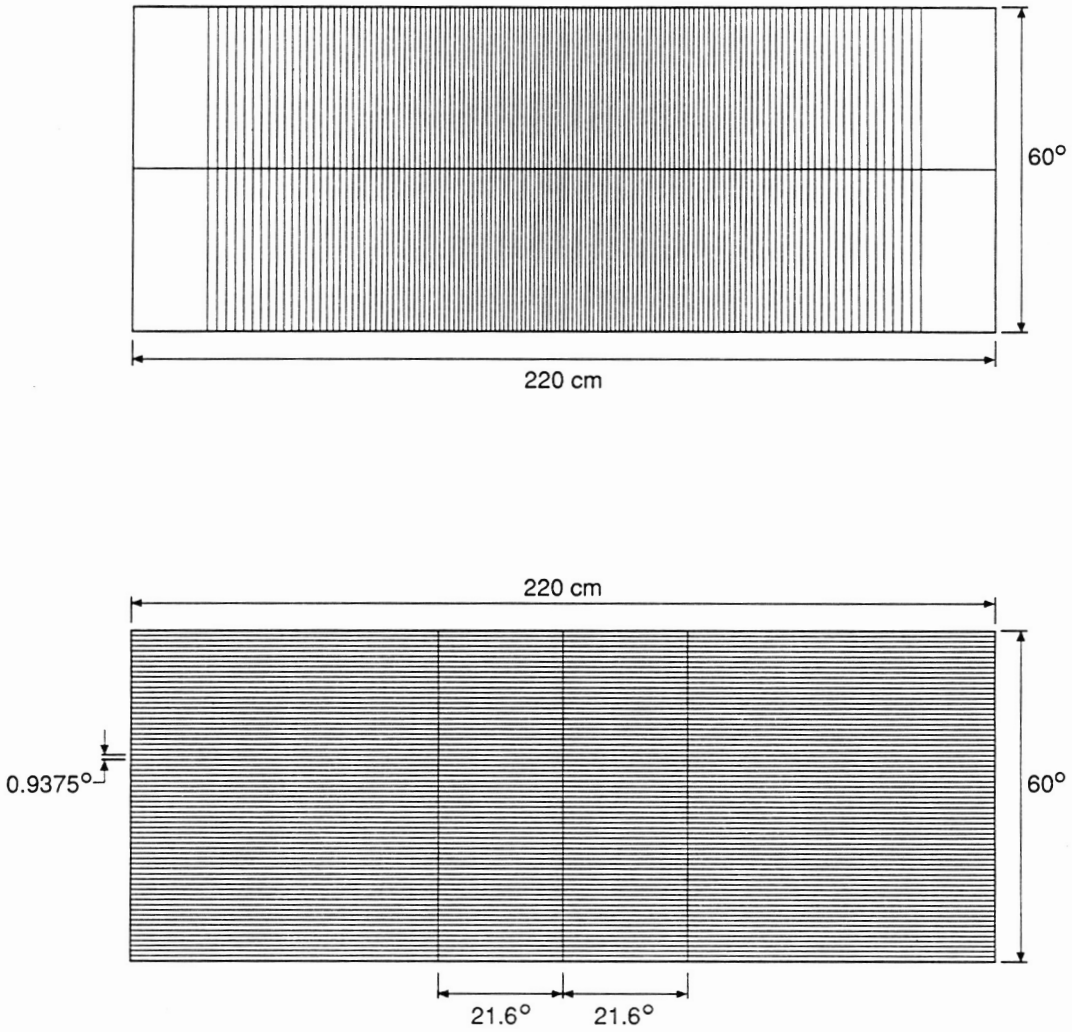

Figure 2-6: Arrangement of SHC θ and ϕ pads in layer 1 of one sextant.

- Sextants are numbered from 1 to 6, starting at $\phi = 90°$ and going clockwise.
- Anode towers are numbered from 1 to 48, starting at $\phi = 90°$ and going counter-clockwise, as viewed from the $+z$ direction.
- Anode layers are numbered from 1 to 20, starting with the innermost layer.
- Cathode layers are numbered from 1 to 5, starting with the innermost layer.
- Divisions are numbered from 1 to 12 in ϕ, and from 1 to 4 in θ, (i.e. each θ or ϕ division is one block wide).

A diagram of the AMY coordinate system and the SHC numbering scheme is shown in Figure 2-7.

SHC Performance

The energy resolution of the SHC is empirically measured to be $\sigma/E = 23\%/\sqrt{E} + 6\%$, where E is the energy of an incident electron, measured in GeV. This was obtained by measuring the width of the Bhabha scattering energy spectrum, and by measuring the widths of the E/P distributions for acollinear e^+e^- pairs.

The angular resolution is given as $\sigma_\theta = 0.3°$ and $\sigma_\phi = 0.1°$. Angular resolution is worse in θ than in ϕ because the charges around the anode wires are well-localized in ϕ, but not in θ.

SHC Operating Parameters and History

High voltage is supplied to the SHC anode wires by several automatic HV power supplies built by OSU. These wires were held at 2150 V, until fall, 1989, when the voltages were reduced to 2100 V to reduce saturation. From time to time an anode wire will break, and

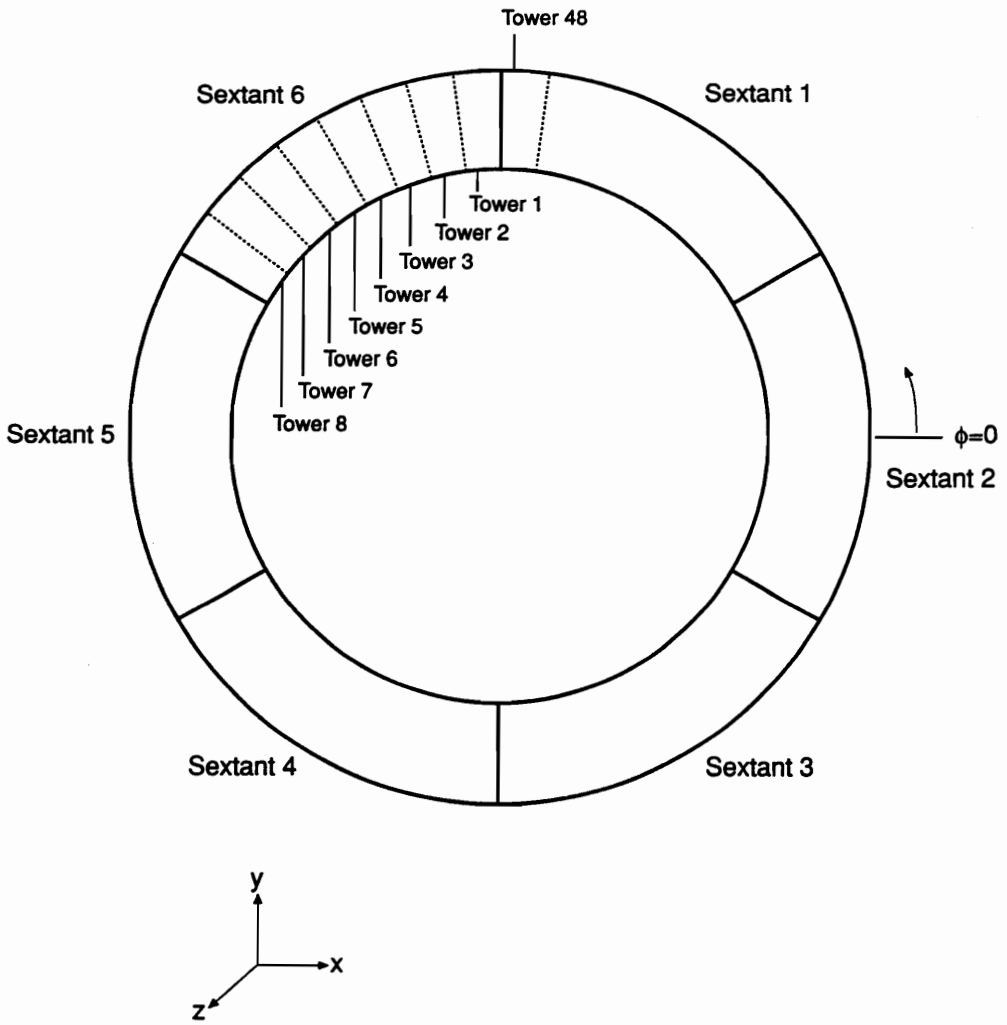

Figure 2-7: SHC numbering scheme and coordinate system.

make contact with its proportional tube. The resulting current drain cannot be supplied by the OSU HV unit. In this case, the anode layer containing the bad wire is removed from that sextant's power supply. Voltage is supplied to that layer by a separate HV supply, at some lower level.

The ionizing gas used in the SHC is primarily an argon-ethane-alcohol mixture (49.25% Ar, 49.25% C_2H_6, 1.5% C_2H_5OH). HRS gas was used for the 55 GeV data set taken in fall, 1987, but this was found to cause discharges.

In the summer of 1988, the SHC was accidentally damaged by an inappropriate application of RF power. As a result, $\sim$ 17% of the wires in sextant 1 and $\sim$ 20% of the wires in sextant 6 were destroyed. Some of the other sextants were also damaged. The resulting energy resolution for sextants 1 and 6 was $\sigma/E = 36\%/\sqrt{E} + 17\%$. Repairs could not be performed until the summer of 1989. At this time sextants 1 and 6 were replaced, and sextants 3, 4, and 5 were restrung. After repair, the SHC was restored to its original capabilities.

SHC Electronics

During an electromagnetic shower, electrons passing through the anode tubes ionize the SHC gas. The resulting ionization electrons are accelerated toward the anode wire, producing more ions in turn. The ionization electrons are carried away on contact with the anode wire. The remaining positive ions induce an image charge on the anode wire and on the cathode pads. This signal is read out by the ADC modules.

A circuit diagram for the anode wiring is shown in Figure 2-8. The signal voltages from the anode gangs in the first (i.e. innermost) 16 layers are passed directly to SUM/BUFFER cards by shielded twisted pair cables; signals from the last 4 anode layers are first preamplified by a factor of 5.5. The SUM/BUFFER cards pass the analog signals to both the triggering system and LeCroy 1885N FASTBUS ADC modules. Cathode signals are not used for

triggering, and are passed directly from the sextants by shielded twisted-pair cables to the FASTBUS ADC modules.

The ADC modules do not produce a linear response for very small signals. In order to push small signals up into the linear range, each ADC module injects a tiny amount of charge to its input while logging data. Before the digital signal is read out, the ADC module subtracts a user-specified number of counts (called a pedestal value) to compensate for the injected charge. It is important that the pedestal values be accurately specified; unfortunately, these can change with time.

After every few runs, a pedestal run is taken while TRISTAN is in fill mode. Around 100 events are taken, and the average number of uncorrected ADC counts is measured for each channel. These values are compared to the stored pedestal values. If too many channels have changed by too much, the ADC modules are reloaded with the new pedestal values.

SHC Triggers

A complete list of the AMY 1.0 and AMY 1.5 triggers can be found in Section 2.2.16; here we will consider only the shower counter triggers. There are two types of SHC triggers: energy triggers and minumum ionizing triggers. All SHC triggers fire on the basis of the SHC anode signals. The energy triggers use information from the first 16 anode layers, whereas the minimum ionizing triggers use the information from the last 4 anode layers. The important triggers for this thesis are the three main energy triggers, whose data bits are numbered 8, 9, and 19.

Trigger bit 8 represents the total shower energy trigger. The raw signals from the first 16 layers of all 48 towers are summed together, and compared to some threshold voltage. This threshold varies, but it typically represents around 8 GeV of energy deposited in the SHC.

Trigger bit 9 was activated in February, 1992 as an upgrade of the AMY 1.5 triggering system [33]. It represents the single shower cluster trigger. First, the anode signals of the

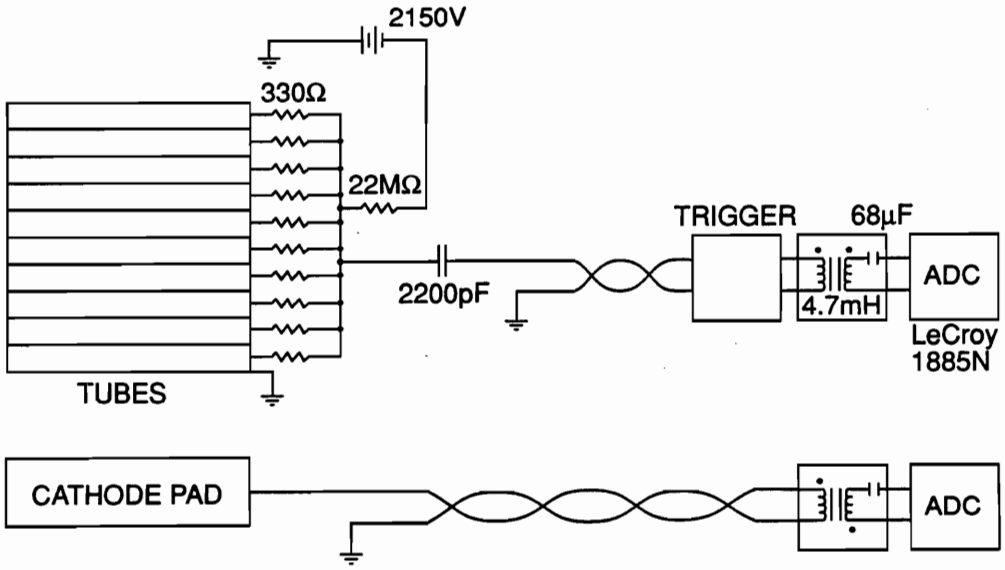

Figure 2-8: High voltage and signal readout for SHC anodes and cathodes.

first 16 layers are summed longitudinally into four gangs of four in each sextant. Each summed gang is paired in turn to the next higher and next lower summed gangs in its own sextant, and in neighboring sextants. If each of the summed gangs in a pair exceed 30% of their combined ADC counts, the combined signal is compared to a threshold voltage. This threshold usually corresponds to a shower of around 5 GeV.

Trigger bit 19 represents the multiple shower cluster trigger. The anode signals from the first 16 layers are summed for each tower. Each tower signal is compared to two threshold voltages, one high and one low. If two or more of the towers pass the low threshold, AND one tower passes the high threshold, the event is triggered. The event can also be triggered if no towers pass the high threshold, provided that three or more of the towers pass the low threshold. The high and low thresholds correspond to around 5 and 3 GeV, respectively.

2.2.7 The Muon Detector (MUO)

The Muon Detector (MUO) lies outside of the magnetic yoke. It is composed of two types of detector: muon chambers (drift tubes) and muon counters (scintillation counters). The MUO is arranged into six planar sextants, each composed of two layers of drift tubes providing z information, two layers of drift tubes providing r-ϕ information, and a layer of muon counters providing timing information.

2.2.8 Small Angle Luminosity Monitor (LUM)

The small angle Luminosity Monitor [34] (LUM) was used to measure the instantaneous luminosity by counting low-angle Bhabha scattering events. It covered an angular range of $4° \leq \theta \leq 6°$ at a distance of 1.73 m from the interaction point on either side.

Each unit of the LUM was composed of four calorimeter quadrants on each side; each quadrant consisted of a barium flouride (BaF_2) crystal, read out by photodiodes. In front of

each quadrant was a scintillation counter (known as a defining counter). Fourfold coincidence between two diametrically opposed LUM quadrants and their defining counters was necessary to trigger an event.

2.2.9 Pole Tip Shower Counter (PTC)

The Pole Tip Shower Counter [35] (PTC) was the primary offline luminosity monitor for AMY 1.0. Each PTC, mounted on one of the endcaps, comprised three components: a front calorimeter, a single-layer proportional counter, and a rear calorimeter. Each PTC is divided into eight cells, of which two are mounted on the fixed key. Axial and side views are shown in Figure 2-9.

The front calorimeter was composed of three layers of plastic scintillator plate interspersed with layers of lead, corresponding to a thickness of 5.7 radiation lengths (X_0). It covered the angular range of $14.6° \leq \theta \leq 24°$.

The rear calorimeter had the same basic design as the front calorimeter, except that it had eight layers of scintillator and lead. It covered the angular range of $14.6° \leq \theta \leq 26.6°$.

The proportional counter was located between the front and rear calorimeter, and consisted of a single layer of the same proportional tubes and anode wires used in the SHC, arranged vertically. In front of the tubes was a layer of G-10 plastic etched with 30 concentric θ cathode strips of width 7.5 mm. Behind the tubes was another layer of G-10 plastic, etched radially with ϕ cathode strips of 3° width. The fiducial range of the proportional counter was $14.6° \leq \theta \leq 26.6°$. The arrangement of ϕ and θ strips is shown in Figure 2-10.

2.2.10 Ring Veto Counter (RVC)

The Ring Veto Counter (RVC) was a tagging counter made of two layers each of lead and scintillator, mounted on the endcaps of AMY 1.0. The total thickness amounted to 3.6

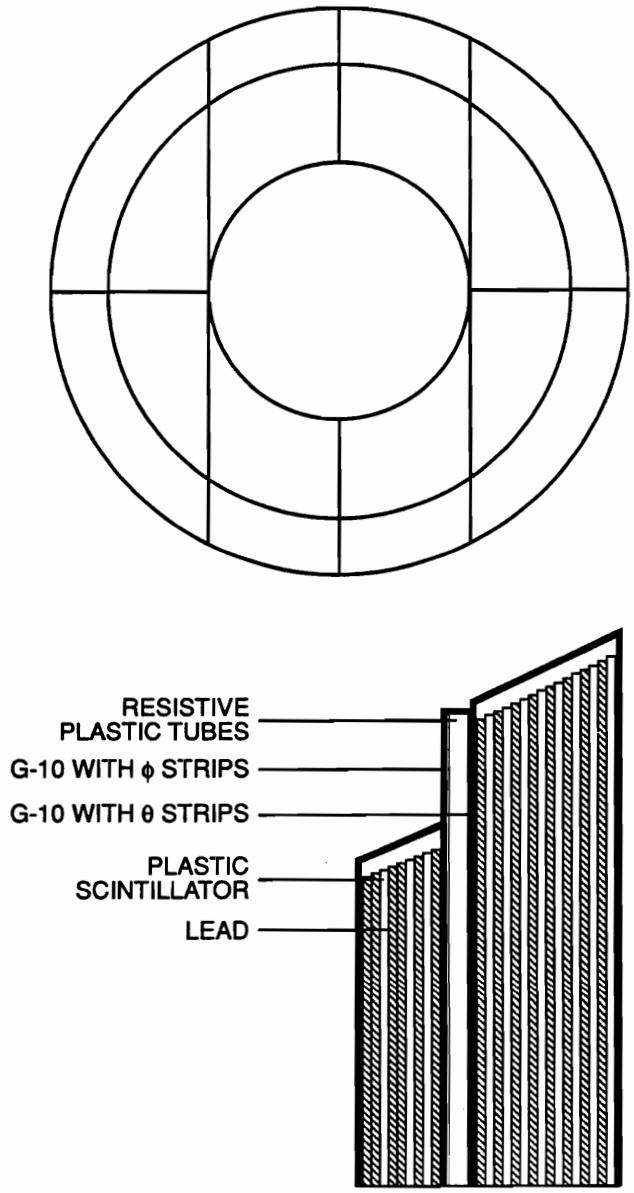

Figure 2-9: The Pole Tip Shower Counter.

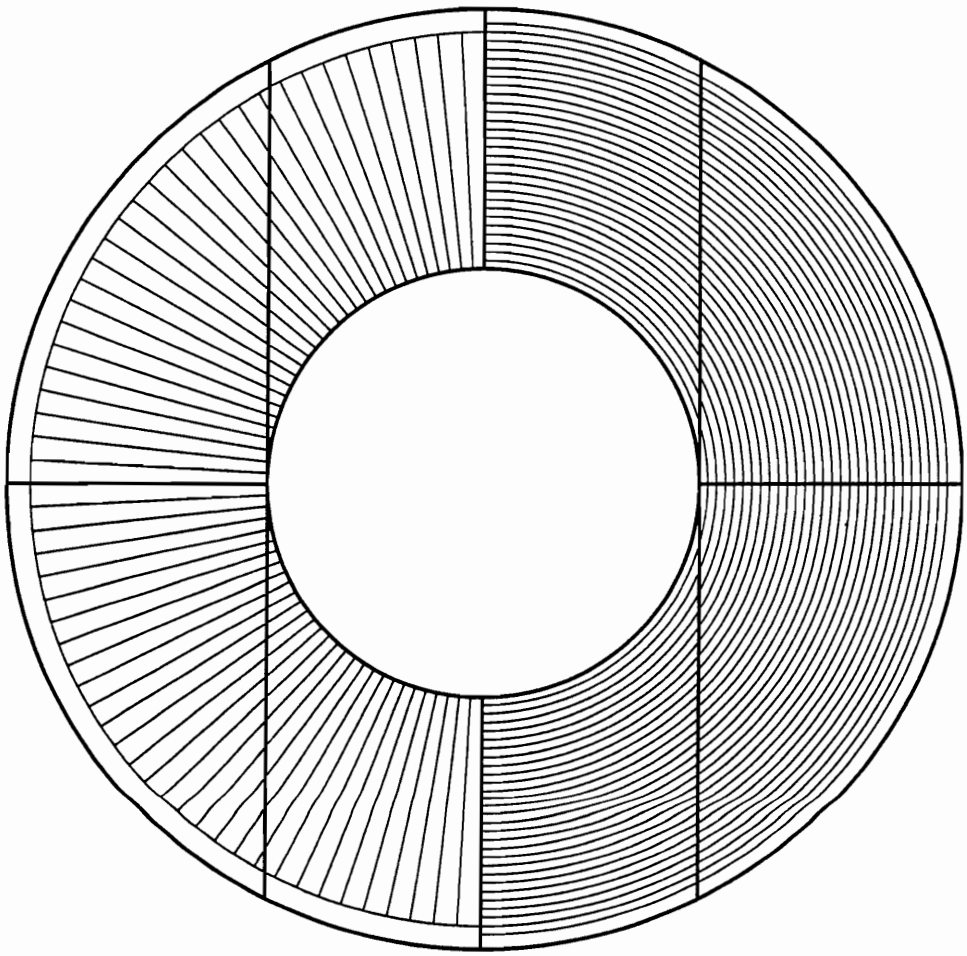

Figure 2-10: ϕ-pad (left) and θ-pad (right) arrangement for the PTC.

radiation lengths at the center of the detector. It was used to provide veto tagging for photons, electrons, and hadrons in the polar region $26° \leq \theta \leq 39°$.

The RVC on each endcap was divided into 7 "azimuthal" detector elements, shown in Figure 2-11. The ϕ range covered by each detector element corresponded to the position of an SHC sextant, except for the area in front of the key, which had its own detector element. Other than the knowledge of which element was hit, no position information was provided.

2.2.11 The X-Ray Detector (XRD)

The X-Ray Detector [36] (XRD) is a one-layer drift chamber designed for electron identification. It was originally designed for AMY 1.0, but was not ready for installation until AMY 1.5. It occupies the region between the CDC and the SHC.

Each of the three chamber modules has a fiducial range of 67 to 79 cm in r, 120° in ϕ, and from -100 to $+100$ cm in z. The chambers are strung with alternating sense and field wires which run parallel to the z-axis at a radius of 73 cm. The sense and field wires are held at 6 kV and 4.5 kV, respectively, in a Xenon-Propane atmosphere (95% Xe 5% C_3H_8). The inner and outer radii of each chamber are grounded.

The XRD was designed to detect the synchrotron radiation emitted by incident electrons in the 3 Tesla magnetic field. It was installed in 1989, and took data during 1990. During this period the CDC was filled with Neon gas to provide X-ray transparency.

2.2.12 Endcap Shower Counter (ESC)

The Endcap Shower Counter [37] (ESC) is the primary offline luminosity monitor for AMY 1.5. Each ESC, mounted on an endcap, extends from a cylindrical radius of 26 cm to a

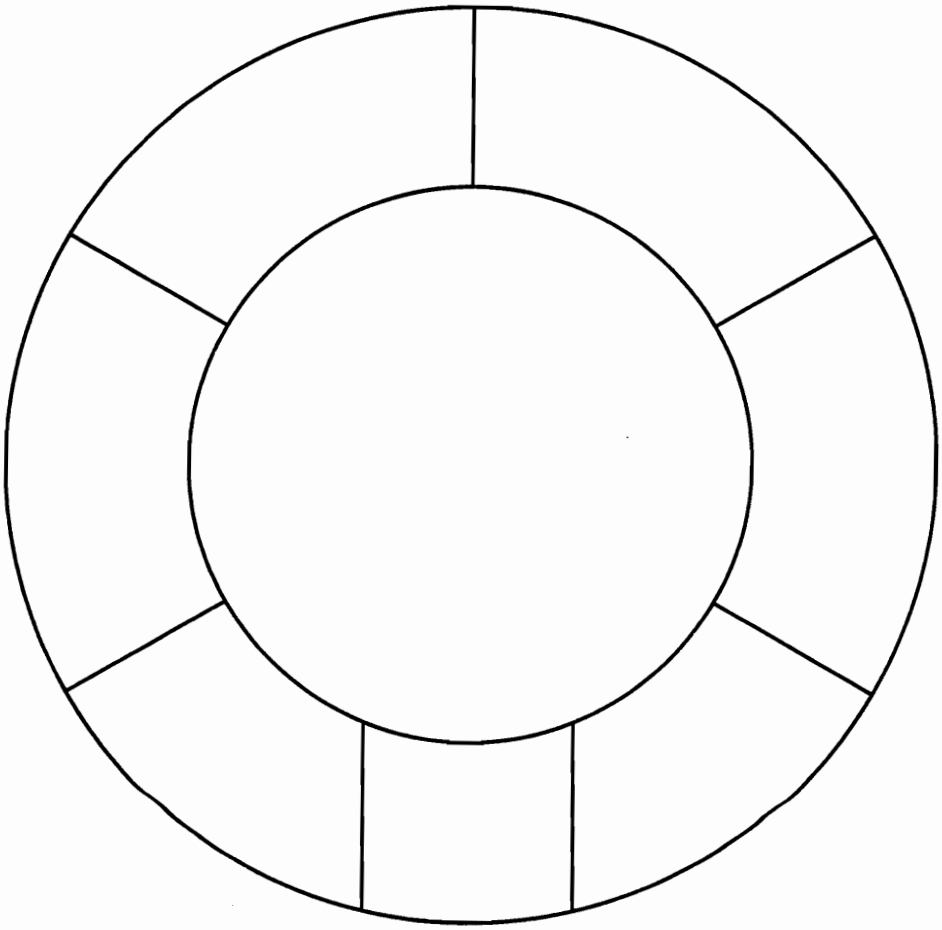

Figure 2-11: The Ring Veto Counter.

radius of 111 cm, corresponding to a polar range of $9.4° \leq \theta \leq 36.5°$; it also extends from 137 cm to 157 cm in z.

Like the PTC, the ESC comprises three layers: a forward lead/scintillator calorimeter, a two-layer proportional counter, and a rear lead/scintillator calorimeter. All three layers cover the same cylindrical radius. Together they have a z-thickness of 20 cm and contain 15 radiation lengths of lead.

The scintillating plates in both the forward and rear calorimeters are divided into 24 sections, each of which subtends 15° in ϕ. Timing and ADC data are read out for each of the 96 scintillator channels.

The cathode pad arrangements for the ESC proportional counter are shown in Figure 2-12. As in the PTC, each ESC has one layer of ϕ cathode pads and one layer of θ cathode pads. Unlike the PTC, each ESC has two proportional tube layers, one for each pad layer.

Each ESC has 192 θ-pads and 192 ϕ-pads, with pad coverage extending from a cylindrical radius of 28.7 cm to 107 cm. Each θ-pad covers a polar angle of 0.79° and an azimuthal angle of 60°. Each ϕ-pad covers an azimuthal angle of 1.88°.

The energy resolution of the ESC is $\sigma_E/E = 15\%/\sqrt{E} + 6\%$, where E is measured in GeV. The proportional counter has a θ resolution of 0.14° and a ϕ resolution of 0.46°.

2.2.13 Small Angle Counter (SAC)

The Small Angle Counter (SAC) is a lead/scintillator calorimeter that covers a polar range of $3.0° \leq \theta \leq 10.0°$, at a distance of 1.32 m from the interaction point on either side. It replaces the LUM of AMY 1.0.

Each SAC calorimeter is divided into 24 sectors in ϕ. Each sector is composed of 22 alternating layers of lead and scintillator (17.2 radiation lengths), read out by photodiodes.

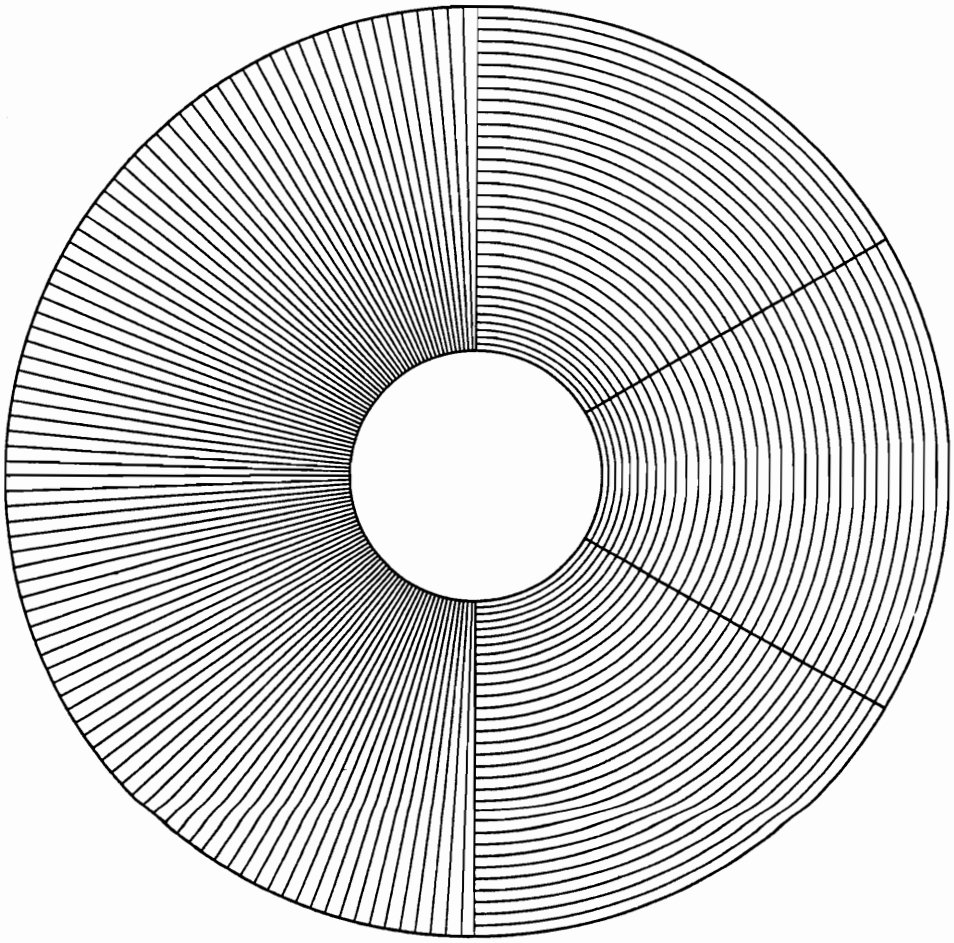

Figure 2-12: ϕ-pad (left) and θ-pad (right) arrangement for the ESC.

Each calorimeter sector has a silicon pad detector at the location of shower maximum, to provide θ information in the region $3.6° \leq \theta \leq 9.4°$. In addition, there are defining counters in front of each calorimeter ϕ sector. These are designed for instantaneous luminosity measurement.

2.2.14 Forward Tracking Chamber (FTC)

The Forward Tracking Chamber (FTC), mounted on the ESC of each endcap, is designed to provide charged particle tracking in the range $12° \leq \theta \leq 27°$. Each FTC comprises five independent chambers, each containing three layers of ~ 60 sense wires. The fifteen layers of wires are variously oriented at $\phi = 30°$, $90°$, and $150°$.

Each layer of sense wires is bounded in the z direction by two layers of Rohacell foam laminated with resistive Kapton plastic, which in turn is printed with conductive epoxy paint. The wires of a given layer are separated by field shaping strips of copper-clad G-10. Layers are electrically isolated from each other by grounded sheets of aluminized mylar.

2.2.15 Vertex Detector (VTX)

The Vertex detector (VTX) is a straw chamber mounted within the ITC on the beam pipe of AMY 1.5. It provides charged particle tracking from a cylindrical radius of 5.3 cm to 7.7 cm, with a polar fiducial volume of $13° \leq \theta \leq 167°$. Like the ITC, it consists of four staggered layers of straws.

Each layer contains 80 aluminized mylar straws of length 56 cm. The straws range in diameter from 4.5 mm in the innermost layer to 5.6 mm in the outermost layer. They are pressurized at 2 atm with HRS gas, and are strung with 15 μm Stablohm resistive anode wire. The 2.7 kΩ resistance of the wires gives the VTX the ability to measure the z-coordinate of each hit, by comparing the charges accumulated at both ends of each wire. The z-resolution of the VTX is about 6 mm.

2.2.16 Triggering

Electron and positron bunches pass through each other at the AMY interaction point 200,000 times every second. Several times each second, an electron and a positron will actually collide. A few of these collisions result in physically interesting events (a tiny fraction of which is included in this work). Spurious events also appear from sources such as cosmic rays, collisions with residual gas molecules in the beam line, or stray electrons striking the beam pipe. The interesting events are further diluted by the inevitable noise from AMY's tens of thousands of channels. Because a finite amout of time is required to read out one event, and because the readout electronics cannot accept new events until it processes the current one, a high event rate can lead to an unacceptable amount of "dead time". It is therefore essential to improve the minute signal-to-noise ratio. This requires some sophistication.

The first method is to require some coincidence between an event and a beam crossing. The second is to require some combination of the signals to resemble some of the properties of potentially interesting physics events. The various signal combinations are called event triggers. It is important that the triggers be highly redundant for good efficiency.

AMY 1.0 Triggering

The event triggers for AMY 1.0 are listed in Table 2-1. The most important triggers are the those for the SHC (described in Section 2.2.6) and those for the ITC and CDC. As noted earlier, the SHC triggers use analog signals passed through a discriminator. The CDC and ITC triggers digitally combine the hits from individual wires to form track segments. The AMY 1.0 triggering system had a processing time of about 1.2 μs per event, and could operate at around 2 Hz with less than 1% dead time.

Table 2-1: Event triggers for AMY 1.0.

Trigger bit	Name
5	PTC trigger
8	SHC total energy
10	Cosmic ray
11	RVC + PTC rear inclusive
13	ITC 2 track + CDC + SHC min I
14	ITC 2 track back-to-back + CDC
15	ITC 2 track + CDC + SHC low majority 1
16	ITC multi-track
17	CDC multi-track
18	CDC looser multi-track + SHC min I
19	(SHC high majority 1 + SHC low majority 2) or (SHC low majority 3)
20	(SHC low majority 2 or SHC high majority 1) + CDC + not (Trigger 19)
21	ITC + CDC 2 track
22	CDC 3 or 4 track
23	ITC 2 track + MUO
24	ITC 2 track + CDC + SHC min I
26	CDC + RVC dimuon
27	ITC + RVC dimuon
28	ITC 2 track + CDC + RVC
30	CDC perfect 2 track
31	CDC perfect 1 track, bachelor V

AMY 1.5 Triggering

The event triggers for AMY 1.5 are listed in Table 2-2. Several triggers were added and several were modified from AMY 1.0; the most important addition for this thesis was trigger bit 9. The logic of the CDC triggering was upgraded to make use of azimuthal information to find radial tracks.

2.2.17 Data Acquisition and Storage

Once an event has been accepted by the triggering system, the gated information is transferred to a VAX 11-780, known as AMYVAX.[4] FASTBUS data are transferred by a FASTBUS Processor Interface (FPI) module, and CAMAC data are handled by a JORWAY module. Once the data from one event have been collated, they are transferred to a FACOM M-780 mainframe via a VMEbus link (prior to 1991, the data were transferred using an IBM DACU link). The FACOM then stores the transferred data from one event in the TRISTAN Bank System (TBS) format used for data analysis, and records them onto magnetic tape.

2.3 Luminosity Measurement

Specific luminosity is determined by the frequency of low-angle Bhabha scattering events; integrated luminosity is proportional to the total number of low-angle Bhabhas counted in a specified time.[5] Bhabha scattering has an advantageously large cross section at small angles, which reduces the statistical error of a luminosity measurement.

[4]The XRD data are transferred separately to a VAXStation II GPX that is clustered with AMYVAX.

[5]This number is divided by the known Bhabha cross section at the collision energy; thus the integrated luminosity is expressed in units of inverse area.

Table 2-2: Event triggers for AMY 1.5.

Trigger bit	Name
1	ESC dimuon
3	Prescaled beam crossing
4	$\geq$ 2 CDC + $\geq$ 1 CDC/SHC min I radial tracks + ITC
5	ESC Bhabha
6	2 CDC/SHC min I back-to-back radial tracks
8	SHC total energy
9	SHC cluster energy
11	ESC 2 photon + CDC
13	ITC 2 track + CDC + SHC min I
14	ITC 2 track back-to-back + CDC
15	ITC 2 track + CDC + SHC low majority 1
16	ITC multi-track
17	CDC multi-track
18	CDC looser multi-track + SHC min I
19	(SHC high majority 1 + SHC low majority 2) or (SHC low majority 3)
20	Looser SHC cluster + CDC + not (Trigger 19)
21	CDC 2 track + ITC + SHC min I
22	CDC 3 or 4 track
23	ITC 2 track + MUO
24	ITC 2 track + CDC + SHC min I
26	ESC + CDC dimuon
27	ESC + FTC dimuon
28	SAC + CDC
29	ESC 2 photon (prescale)
30	CDC perfect 2 track
31	CDC perfect 1 track or bachelor V, later CDC perfect 1 track or bachelor V or acoplanar CDC 2 track

Unfortunately, the cross section is also precipitously steep: the accuracy with which one measures the low-angle Bhabha cross section is limited by the uncertainty of the detector placement, and by the distribution of interaction points about $z = 0$.

The systematic uncertainty for the PTC luminosity measurements of AMY 1.0 was 2.4%; that for the ESC luminosity measurements of AMY 1.5 was 1.8%. These estimated errors appear as a systematic uncertainty in every other cross section we wish to measure.

A summary of the measured integrated luminosities for the run periods included in this analysis is given in Tables 2-3 and 2-4. The run period 6226-6286 was taken during the Spring, 1989 energy scan. This is represented in the ninth entry in Table 2-3, which is a weighted sum of the next nine entries. The sum of the scan data has an effective energy of 58.5 GeV.

We can check the long-term behavior of this systematic uncertainty by examining the frequency of large-angle Bhabha events vs. the frequency of small-angle Bhabha events. The large-angle Bhabha cross section is smaller than the small-angle cross section, but not nearly so steep. Barrel Bhabha counts are given in Tables 2-3 and 2-4.

2.3.1 Anomalous Run Periods

A small number of runs have been excluded from the AMY luminosity measurements. The luminosity for run period 10983-11805 in Table 2-4 reflects the removal of runs 10992, 11100-11102, 11122-11123, 11186-11207, 11289, and 11664-11668. These runs had either high background rates or difficulties with ESC high voltage. In either case, luminosities could not be measured accurately, so the runs were discarded.

In addition, a small section of data (runs 9158-9172) were not included in the present analysis, due to suspect SHC triggering (see Section 6.4.2). The integrated luminosity for these runs ($170\,\mathrm{nb}^{-1}$) is subtracted from the $26.73\,\mathrm{pb}^{-1}$ of data taken in the spring of 1990, for an effective integrated luminosity of $26.56\,\mathrm{pb}^{-1}$.

Finally, the luminosities for the spring, 1991 data and the spring, 1992 data are shown with two errors: the first is statistical, and the second is an additional systematic error reflecting uncertainties due to dead ESC phototubes.

Table 2-3: Luminosities for AMY 1.0 run periods.

Run Period	Date	$\sqrt{s}$	PTC $\int \mathcal{L}\, dt$	# SHC BB
2733 - 2987	Spring 1987	50.00	0.636 ± 0.016	246
3048 - 3568	Summer 1987	52.00	3.976 ± 0.080	1506
3712 - 4416	Fall 1987	55.00	3.266 ± 0.039	1189
4511 - 5170	Spring 1988	56.00	5.993 ± 0.053	2074
5173 - 5361	Summer 1988	56.50	0.994 ± 0.022	349
5369 - 5692	Summer 1988	57.00	4.398 ± 0.046	1482
5816 - 6121	Fall 1988	60.00	2.465 ± 0.037	764
6134 - 6223	Spring 1989	58.50	0.801 ± 0.016	231
6226 - 6286	Spring 1989	(scan)	(0.721 ± 0.015)	(222)
6226 - 6230	Spring 1989	57.25	0.0582 ± 0.0043	15
6231 - 6237	Spring 1989	57.50	0.0803 ± 0.0050	21
6238 - 6243	Spring 1989	57.75	0.0781 ± 0.0050	32
6244 - 6250	Spring 1989	58.00	0.0772 ± 0.0050	17
6251 - 6256	Spring 1989	58.75	0.0865 ± 0.0054	23
6257 - 6265	Spring 1989	59.00	0.0939 ± 0.0056	29
6266 - 6272	Spring 1989	59.25	0.0984 ± 0.0058	42
6274 - 6279	Spring 1989	59.50	0.0724 ± 0.0050	19
6280 - 6286	Spring 1989	59.125	0.0755 ± 0.0050	24
6290 - 6332	Spring 1989	59.05	0.505 ± 0.013	146
6334 - 6410	Spring 1989	60.00	0.757 ± 0.020	213
6423 - 6674	Spring 1989	60.80	1.376 ± 0.059	461
6676 - 6697	Spring 1989	59.00	0.178 ± 0.010	64
6698 - 6703	Spring 1989	60.80	0.0575 ± 0.006	20
6705 - 6740	Spring 1989	59.00	0.371 ± 0.014	129
6744 - 6822	Spring 1989	60.80	0.708 ± 0.020	237
6906 - 6997	Spring 1989	60.00	0.347 ± 0.013	109
7006 - 7176	Spring 1989	60.80	1.181 ± 0.028	370
7192 - 7629	Summer 1989	61.40	4.287 ± 0.060	1194
7662 - 7795	Summer 1989	54.00	0.531 ± 0.017	146

Table 2-4: Luminosities for AMY 1.5 run periods.

Run Period	Date	$\sqrt{s}$	ESC $\int \mathcal{L}\, dt$	# SHC BB
7889 - 8245	Fall 1989	64.00	1.097 ± 0.026	241
8246 - 8351	Fall 1989	63.60	0.440 ± 0.011	72
8353 - 8356	Fall 1989	60.00	0.0164 ± 0.0014	3
8378 - 10896	Spring 1990	58.00	26.56 ± 0.10	7434
10983 - 11805	Spring 1991	58.00	$8.10 \pm 0.08 \pm 0.04$	2317
11821 - 12639	Fall 1991	58.00	25.73 ± 0.10	7275
12650 - 14579	Spring 1992	58.00	$62.92 \pm 0.15 \pm 0.12$	17800
14594 - 15259	Fall 1992	58.00	19.44 ± 0.08	5396
15260 - 15292	Fall 1992	59.70	0.97 ± 0.02	219
15293 - 15330	Fall 1992	58.20	1.38 ± 0.02	379
15331 - 15373	Fall 1992	59.20	1.36 ± 0.02	375
15374 - 15412	Fall 1992	58.45	1.31 ± 0.02	341
15413 - 15458	Fall 1992	58.70	1.32 ± 0.02	403
15459 - 15519	Fall 1992	58.95	1.72 ± 0.03	468
15520 - 15562	Fall 1992	59.45	1.20 ± 0.02	342
15563 - 15630	Fall 1992	57.60	2.03 ± 0.03	554

Chapter 3

Monte Carlo Techniques

Experimental science lies in the comparison between the data and a theory. When a theory is complicated, however, or involves more than a few variables, it becomes difficult to calculate exact predictions from it analytically. These difficulties are greatly worsened when the data are to be taken by a complicated, imperfect apparatus.

Fortunately, since the advent of computers analytical solutions are no longer necessary. Enormous numbers of variables can be handled by the technique of Monte Carlo integration. In this method, an integrated solution is estimated from a number of randomly selected sample points. The price for the ease of calculation is accuracy: the statistical uncertainty of a calculation from N sample points is proportional to $1/\sqrt{N}$ [40].

The first requirement for a successful Monte Carlo integration is that the distribution of sample points should closely follow the function to be integrated. This is typically accomplished by the method of Von Neumann rejection (VNR). For example, suppose we are integrating a function f over some range in one variable, say x. We start by randomly distributing our intended sample points uniformly over the integration range. We then discard sample points by the following prescription: for each point generate a uniform random

number between 0 and 1, and compare that number to the value of the function at that point, divided by the maximum function value in the integration range. The distribution of the remaining sample points will follow the function. The average of $f(x)$ over sample points, multiplied by the length of the integration range, approximates the integral.

This method becomes very inefficient if there are any high peaks in the integration range, or if the function is steep. In a case where we have a narrow peak a thousand times higher than the average function value, we will typically throw away 99.9% of our sample points. We can improve this efficiency by distributing our initial sample points according to some generating function g, which has the following properties: 1) that $g(x)$ be greater than $f(x)$ over the integration range, 2) that $g(x)$ follow $f(x)$ closely, and 3) that $G^{-1}(x)$, where $G(x) = \int_0^x g(t)dt$, be defined over the integration range. If $f(x)$ is poorly behaved over the integration range, we can naturally break up the range, and assign to each section a different generating function $g_i(x)$.

The integration scheme is then as follows: 1) In each integration range, say from a_i to a_{i+1}, produce a number of uniform random numbers from 0 to 1. For the j^{th} uniform random number r_j, we calculate a point x_j in the range a_i to a_{i+1}:

$$x_j = a_i + \frac{G^{-1}(r_j)}{\int_0^{a_{i+1}-a_i} G^{-1}(t)dt}. \tag{3.1}$$

2) We then perform VNR at the point x_j: if another uniform random number r'_j is greater than $f(x_j)/g_i(x_j)$, the sample point is rejected, otherwise it is kept. Clearly, the efficiency of calculation depends on how closely $g_i(x)$ follows $f(x)$.

In high energy physics, the large set of integration variables is separated into two classes: those related to the underlying physics, and those related to the experimental apparatus. The first phase of a Monte Carlo study is called *generation.* In this phase, artificial events of a particular interaction are generated according to the theoretical cross section of that

interaction. The second phase is called *simulation.* In this phase, the response of the experimental apparatus is simulated for the events generated in the first phase.

3.1 $\gamma\gamma$, $\gamma\gamma\gamma$ Production

The process $e^+e^- \rightarrow \gamma\gamma, \gamma\gamma\gamma$ presents some difficulties for Monte Carlo generation. As was seen in Chapter 1, the cross section becomes infinitely large as the energy of the softest photon is decreased to zero, or as the polar angle of either of the hardest photons is decreased to zero.

Fortunately, an adaptive Monte Carlo package called BASES/SPRING has been developed by Kawabata [41] to deal with singular cross sections. The first phase of generation, the program BASES, divides the cross section into subregions, and computes a set of generating functions. The second phase, the program SPRING, uses these generating functions to produce sample events.

BASES and SPRING have been applied to the $\gamma\gamma, \gamma\gamma\gamma$ cross section by Fujimoto, Igarashi, and Shimizu [13], [5]. The theoretical results presented in this thesis, particularly the radiative corrections to $e^+e^- \rightarrow \gamma\gamma$, rest squarely on this implementation.

For the purposes of simulation, we have used an angular cut of 1° for the hardest photons, and a cut of 100 MeV to separate the soft photon real correction from the hard photon real correction. For the purposes of calculating the 58 GeV radiative correction as a function of angle, we have used a soft/hard photon cut of 10 MeV.

3.2 Unstable Photino Production

Monte Carlo events from the pair production and decay of unstable photinos have been calculated using the program PHASER,[1] developed by this author. The prompt cross section (Equation 1.31) has a complicated dependence upon polar angle, but it is everywhere free from singularities. The subsequent decay (Equation 1.32) is isotropic in its rest frame. These properties make event generation an almost trivial programming exercise (the author's abilities notwithstanding).

The general algorithm makes no use of any generating functions. The differential cross section (1.31) is integrated, and the maximum value of the function is found.[2] Sample points are chosen by randomly selecting points uniformly on $-1 \leq \cos\theta \leq 1$, and rejecting points where a second random deviate (uniform on $[0,1)$) is greater than the function at that point divided by the function maximum. The ϕ angle for the photinos is chosen uniformly over $0 \leq \phi_{\tilde{\gamma}} \leq 2\pi$.

Once the prompt scattering angle has been chosen, we consider the decay of each photino in its rest frame. As was shown in Section 1.2, the decay lifetime is dependent on the photino mass and on the SUSY breaking scale. For each of our photinos, we randomly choose a specific decay length according to the lifetime given by Equation 1.33, where we have chosen a SUSY breaking scale parameter of $d = (300\,\mathrm{GeV})^2$. (In the case of SUGRA models, this is well below the scale where the gravitino mass would begin to affect the decay kinematics.) If the decay length is any longer than a few centimeters (which is possible for $M_{\tilde{\gamma}} \lesssim 0.7$ GeV) the acceptance factors are likely to change, thus each daughter photon is propagated from its secondary vertex.

We choose an angle θ'_γ for the daughter photon by randomly selecting $\cos\theta'_\gamma$ uniformly over $[-1,1)$. We realize that the ϕ direction of the photon in this frame is completely

[1] PHotino And Scalar Electron Randomizer—the program admittedly homespun, the title admittedly whimsical.

[2] The maximum of the differential cross section depends upon $M_{\tilde{e}}$, $M_{\tilde{\gamma}}$, and s, but it typically occurs at either $\cos\theta = \pm 1$ or $\cos\theta = 0$. The overall size of the cross section decreases with $M_{\tilde{e}}$.

random, but arbitrarily choose a coordinate system in this frame such that $\phi'_\gamma = 0$. The Goldstino/gravitino is emitted in the opposite direction, escaping detection and our concern.

The momentum vector for the daughter photon, in the coordinate system we have chosen in the photino rest frame, we will call $(x''_\gamma, y''_\gamma, z''_\gamma)$. We will transform it, via a Lorentz boost, to another coordinate system in the laboratory frame:

$$\begin{pmatrix} x''_\gamma \\ y''_\gamma \\ z''_\gamma \end{pmatrix} = \begin{pmatrix} \frac{1}{2}M_{\tilde{\gamma}} \sin\theta'_\gamma \\ 0 \\ \frac{1}{2}M_{\tilde{\gamma}} \cos\theta'_\gamma \end{pmatrix} \overset{\text{boost}}{\longrightarrow} \begin{pmatrix} x'_\gamma \\ y'_\gamma \\ z'_\gamma \end{pmatrix} = \begin{pmatrix} \frac{1}{2}M_{\tilde{\gamma}} \sin\theta'_\gamma \\ 0 \\ \frac{1}{2}(1-\beta^2)^{-1/2} M_{\tilde{\gamma}} \cos\theta'_\gamma \end{pmatrix} \tag{3.2}$$

where $\beta = \sqrt{1 - 4(M_{\tilde{\gamma}}^2/s)}$ is the velocity of the photino.

Finally, we must calculate the direction of the photon by rotating the (x', y', z') coordinates back into the usual detector coordinates. We accomplish this by using the inverse Euler angle transformation. For this we require three angles, commonly denoted θ, ϕ, and ψ (We note here that the θ and ϕ angles in the AMY coordinate system are defined according to the y-convention). The first two have already been chosen as $\theta_{\tilde{\gamma}}$ and $\phi_{\tilde{\gamma}}$; the last we can choose uniformly over $0 \leq \psi \leq 2\pi$. This randomization reflects the freedom we had in choosing ϕ'_γ.

The coordinate transformation is then given by:

$$\begin{pmatrix} x_\gamma \\ y_\gamma \\ z_\gamma \end{pmatrix} = \begin{pmatrix} M_{11} & M_{12} & M_{13} \\ M_{21} & M_{22} & M_{23} \\ M_{31} & M_{32} & M_{33} \end{pmatrix} \begin{pmatrix} x'_\gamma \\ 0 \\ z'_\gamma \end{pmatrix}, \tag{3.3}$$

where the matrix M_{ij} is given by

$$\begin{pmatrix} \cos\theta_{\tilde{\gamma}}\cos\phi_{\tilde{\gamma}}\cos\psi - \sin\phi_{\tilde{\gamma}}\sin\psi & -\cos\theta_{\tilde{\gamma}}\cos\phi_{\tilde{\gamma}}\sin\psi - \sin\phi_{\tilde{\gamma}}\cos\psi & \sin\theta_{\tilde{\gamma}}\cos\phi_{\tilde{\gamma}} \\ \cos\theta_{\tilde{\gamma}}\sin\phi_{\tilde{\gamma}}\cos\psi + \cos\phi_{\tilde{\gamma}}\sin\psi & \cos\phi_{\tilde{\gamma}}\cos\psi - \cos\theta_{\tilde{\gamma}}\sin\phi_{\tilde{\gamma}}\sin\psi & \sin\theta_{\tilde{\gamma}}\sin\phi_{\tilde{\gamma}} \\ -\sin\theta_{\tilde{\gamma}}\cos\psi & \sin\theta_{\tilde{\gamma}}\sin\psi & \cos\theta_{\tilde{\gamma}} \end{pmatrix}.$$

Repeating this process for the second photino (which has a direction of $\theta = 180° - \theta_{\tilde{\gamma}}$, $\phi = 360° - \phi_{\tilde{\gamma}}$), we have the four-momenta of two photons in the detector frame for each event.

3.2.1 Acceptance Factors and Radiative Corrections

The shape and size of the $e^+e^- \to \tilde{\gamma}\tilde{\gamma}$ cross section is different for every choice of $M_{\tilde{\gamma}}$ and $M_{\tilde{e}}$, making full detector simulation impractical. In order to correct for detector acceptance, several systematic effects were added to the Monte Carlo, effectively calculating the acceptance factors through Monte Carlo integration.

SHC resolution is emulated by smearing the final state energies and angles. Energy smearing is done by changing each photon energy by a random amount generated from a Gaussian of width $0.23\sqrt{E} + 0.06E$, where E is in GeV. Angular smearing is done with Gaussians of width 0.1° in ϕ and 0.3° in θ.

The z-coordinate of the event vertex is shifted by a random length, generated from a Gaussian of width 1 cm. This shift is added to the photino decay points from which the photons are propagated.

In the case of the lighter photino masses, photon energies can be soft. It is thus necessary to include some realistic trigger emulation in the analysis of the photino Monte Carlo. This is done by empirically histogramming the trigger thresholds (as a function of energy) using prehadronic data for AMY 1.0 and AMY 1.5, fitting each threshold to the sigmoid function $a + b\tanh(cE - d)$ (where a, b, c and d are the fitting parameters), and performing Von

Neumann rejection for each event against each trigger. An event is discarded if it fails all triggers.

Photons are also given some probability to convert into an e^+e^- pair. The conversion probability for each photon is $0.0278/\sin\theta_\gamma$ for AMY 1.0 and $0.0187/\sin\theta_\gamma$ for AMY 1.5 (see Appendix B). If either photon converts, the event is rejected.

Each photon is given a randomly generated punch-through distance $x = -\frac{1}{\mu}\ln(u)$ into the SHC, where x is the thickness of lead the photon has punched through, $\mu = 1.4854\,\mathrm{cm}^{-1}$ is the linear attenuation coefficient for lead, and u is a uniform random deviate on $[0,1)$. If either photon penetrates beyond anode layer 14 (again remembering the $\sin\theta$ dependence), the event is considered to be lost.

We have not attempted to calculate the radiative corrections to $\tilde{\gamma}\tilde{\gamma}$ production. We note in Section 6.3 that the $\mathcal{O}(\alpha^3)$ radiative corrections for $e^+e^- \to \gamma\gamma$ decrease the cross section by as much as 10% at $\theta = 90°$ in the TRISTAN energy range. We therefore conservatively reduce the $e^+e^- \to \tilde{\gamma}\tilde{\gamma}$ cross section by 10% overall to account for radiative corrections.

3.3 Singly Radiative Bhabha Production

The primary source of inefficiency for the detection of $e^+e^- \to \gamma\gamma$ is the conversion of one (or both) photons into an e^+e^- pair. These events are disqualified by the most powerful selection criterion: that there be no charged tracks in the event. In principle this requirement can be relaxed somewhat, if we realize that the $\gamma \to e^+e^-$ pair tends to have a very small opening angle. Other experiments typically recoup lost events by selecting for a highly acollinear e^+e^- pair back-to-back with a high-energy photon.

Unfortunately, this topology can be closely imitated by the prompt process of singly radiative Bhabha scattering, $e^+e^- \to e^+e^-\gamma$. In the case where there is a very hard (i.e. beam energy) photon radiated from an initial state electron, and a virtual photon in the s-channel,

the virtual photon is nearly on-shell, causing a singularity in the cross section (referred to as the s' channel singularity). The virtual photon couples to the final state electrons, which are produced in an extremely boosted frame and are therefore highly acollinear in the detector frame.

It is therefore necessary to produce a Monte Carlo estimate of the contribution from this process. To this end we employed an event generator by Tobimatsu and Shimizu [42], which produces radiative Bhabha events using an implementation of BASES and SPRING.

3.4 Doubly Radiative Bhabha Production

As was mentioned in Section 1.2, the second most important background for the acoplanar $\gamma\gamma$ signature of photino decay is $e^+e^- \rightarrow (e^+e^-)\gamma\gamma$, where the final state electrons escape detection. This presents some difficulty if we want to proceed from the perturbative expansion: there are 48 $\mathcal{O}(\alpha^4)$ diagrams to consider, and the cross section can be expressed in no fewer than seven dimensions.

The Yennie-Frautschi-Suura exponentiation technique provides a way around this difficulty. This method is non-perturbative, in the sense that it sums to infinite order the contributions from soft virtual and real photons. As a by-product, it can produce correct distributions for arbitrary numbers of real radiated photons.

For the purposes of accurate luminosity measurement at LEP, a YFS-based Monte Carlo program, BHLUMI 2.01, was developed by S. Jadach, E. Richter-Wąs, B.F.L. Ward, and Z. Wąs [43]. Because this program was optimized for low-angle Bhabha scattering, it was particularly suitable for this thesis. We are also assured that the photon distributions would be accurate for the estimation of the background for photino decay [44]. The up-to-100 photons generated in the final state are more than sufficient for this purpose.

3.5 Doubly Radiative $\nu\bar{\nu}$ Production

The last background to $e^+e^- \to \tilde{\gamma}\tilde{\gamma} \to \tilde{G}\tilde{G}\gamma\gamma$ is $e^+e^- \to \nu\bar{\nu}\gamma\gamma$. Because this process contains two massless particles in the final state, such an event is *a priori* indistinguishable from an example of unstable photino pair production. With an appropriate Monte Carlo, however, we might hope statistically to distinguish *event samples* of the two processes. Even if a statistical separation is not possible, such a Monte Carlo would provide an estimate of the expected number of background events.

The radiative pair production of neutrinos is a vitally important process at LEP, where it is used to measure the invisible width of the Z resonance. Higher order radiative corrections add approximately half the number of events one would expect from an additional light neutrino species; thus at LEP energies the $e^+e^- \to \nu\bar{\nu}\gamma\gamma$ process cannot be neglected.

For this purpose a Monte Carlo for $e^+e^- \to \nu\bar{\nu}\gamma$, $\nu\bar{\nu}\gamma\gamma$ was developed by Mana and Martinez [45]. Since LEP produces real Z bosons, the program emphasizes diagrams with s-channel Z propagators. The singly radiative generator includes all third-order diagrams (including those with a t-channel W propagator), plus the fifth-order virtual corrections with an s-channel Z propagator. The doubly radiative generator includes only the lowest-order diagrams with an s-channel Z.

Because this program neglects the 12 diagrams for $\nu_e\bar{\nu}_e\gamma\gamma$ production mediated by a W, it is not perfectly suited for estimating the background to $e^+e^- \to \tilde{\gamma}\tilde{\gamma} \to \tilde{G}\tilde{G}\gamma\gamma$ at TRISTAN energies. Nevertheless, we would expect this Monte Carlo to give reliable order-of-magnitude predictions for several reasons. First, the contribution from W-exchange diagrams to the lower-order processes is maximal at the W-pair production threshold ($\sqrt{s} = 161$ GeV), where it is $\sim 20\%$. Second, the Z-exchange diagrams pick up a weighting factor of 3 from $Z \to \nu_e\bar{n}u_e$, $\nu_\mu\bar{n}u_\mu$, $\nu_\tau\bar{n}u_\tau$, whereas the W-exchange diagrams have only the ν_e channel available.

3.6 The AMY Simulator

Once a number of events have been produced with one of the above generators, the output file can be fed into the AMY simulator [46]. This program imitates the detector response. The resulting data sets have the same structure as real AMY data, and can be analyzed in the same way.

There are four main parts to the AMY simulation program:

- The steering routines handle data input/output operations, trace particles through the detector, and handle particle interactions.
- Block data specifies detector boundaries, material properties, and particle properties.
- Detector interface routines transfer control between the steering routines and the detector simulation routines.
- Detector simulation routines trace particles through the specific detectors, and produce detector signals.

For the purposes of this thesis, the most important parts of the AMY simulator are the SHC detector routines. Fortunately, the desire for accurate SHC simulation outweighed the cost of CPU time when the AMY simulator was being developed.

The SHC simulation code is an implementation of EGS4. Even a brief description of the EGS4 code system would be too lengthy to present here; the reader is referred to the EGS4 Code System manual ([47]) for details.

In the preparation of this thesis, full simulation was performed only for the processes $e^+e^- \rightarrow \gamma\gamma, \gamma\gamma\gamma$. The calculation of all other signatures depends on generator-level samples, smeared to be consistent with the energy and angle resolutions of the SHC.

Chapter 4

SHC Analysis

In this chapter we will discuss how electromagnetic showers deposit energy in the AMY SHC, and how the information from the SHC is used to reconstruct them.

4.1 Energy Distribution in Electromagnetic Showers

When a photon with energy above $2m_ec^2$ passes through matter, it naturally has some probability to interact and form an electron-positron pair. These will in turn interact with the medium, producing photons through bremsstrahlung or annihilation. This process continues until the energy is so subdivided that no more pairs can be produced. The resulting electrons will shed their remaining energy by the excitation and ionization of the medium.

The development of an electromagnetic shower is an inherently random process. Because a typical shower develops unevenly, it is impossible to predict the energy deposition in any given shower. The average behavior, however, is well understood.

The empirical relationship describing average longitudinal shower development is given by

$$\frac{dE}{dt} = E_0 \frac{\beta^{\alpha+1}}{\Gamma(\alpha+1)} t^{\alpha} e^{-\beta t}, \tag{4.1}$$

where $t = (x - x_0)/X_0$ is the radiative depth of the shower in radiation lengths, x_0 is the point where the shower begins, E_0 is the incident photon energy, and α and β are free parameters. The position of shower maximum is at $t_{\max} = \alpha/\beta$.

The transverse development of an electromagnetic shower is dominated by multiple scattering effects, although there is a small (albeit broader) contribution from the propagation of less-attenuated photons.[1] These processes can be described by a sum of two Gaussians; here it is sufficient to note that the average energy distribution is symmetric about the axis of the incident particle [48].

4.2 General Method of SHC Analysis

The first step in SHC analysis is the correction of the raw ADC counts from the cathode strips. These corrections, including variations in the high voltage, dead cathode and anode channels, crosstalk and noise supression, abnormal pedestal subtraction, and gain variations, are described in the following section. Second, the cathode information from all five layers is summed, and clusters are reconstructed in each θ-ϕ block. Third, clusters straddling block boundaries are merged together. Fourth, the energy, θ, and ϕ values for each cluster are reconstructed. Fifth, the energy, θ, and ϕ for each layer of each cluster are reconstructed, using the θ- and ϕ-pads assigned to each cluster. Finally, calibration corrections are applied to ensure a flat response from the SHC.

[1] By this we mean the lowest energy photons. The photon attenuation length in lead peaks between 1 and 10 MeV, for example.

4.3 Corrections to SHC Raw Data

4.3.1 High Voltage Correction

Occasionally an anode wire will break, and the piece being held at high voltage will make contact with its tube. It will typically draw more current than can be supplied by the automatic HV power supplies. In this case, the damaged layer will be supplied by a manually operated HV power supply, typically at a lower operating voltage. This naturally affects the gain of that anode layer, and the signal from its cathode layer. To compensate, a gain correction factor is calculated by averaging the HV gains of all four anode layers in the ganged cathode layer. Gain factors are computed for each ganged cathode layer in each of the 12 ϕ divisions.

4.3.2 Dead Cathode Channel Correction

Cathode signals can be lost through bad connections, severed or damaged cables, or cracked traces on a cathode G-10 layer. These dead cathode channels can be easily mapped by applying square-wave voltage pulses to the layers of lead in the SHC, and monitoring the output of each channel. They can also be detected in the offline analysis by examining the cathode signals from Bhabha events.

Dead cathode channels are corrected by replacing any residual ADC counts with the average of the signals from the same pad in the next higher and next lower cathode layer, and from the pad's nearest neighbors in the same cathode layer. If there are adjacent dead channels in one layer, only the information from the layers above and below is used [49].

4.3.3 Noise Subtraction

As the SHC ages, the tension on the anode wires is thought to cause the tungsten core to slip relative to the gold coating at the soldered ends. In some wires, the tungsten slips

far enough to cause the wire to sag. Electrostatic attraction between the wire and its resistive tube increases the sagging; when the wire gets close enough to the resistive tube, it discharges. The sudden release of tension causes the wire to snap back, where it is attracted by and discharges against the opposite side of the tube.[2]

Such discharges produce enormous anode and cathode signals. While this does not pose a great problem for triggering (as a signal line can be easily disconnected from the triggering system), it does pose an analysis problem. While AMY is running, the only way to stop a noisy channel from discharging is to disconnect the HV line to that layer. It is preferable not to do this, particularly if several layers are already disconnected. The noise signals must therefore be removed prior to analysis. This is done by setting the channel to zero, and interpolating as if it were a dead channel [50].

Noise clusters from random or sporadic discharges can also be identified in the analysis. A discharge cluster in a given anode tower will typically have over 80% of its anode and cathode ADC counts in the discharging layer. If a cluster (over 1 GeV) meets either of these criteria, a noise flag is set.

4.3.4 Dead Anode Channel Corrections

There are two ways for an anode channel to be dead. First, a channel can be "merely dead" if the wires are intact and holding high voltage, but the anode signal is interrupted by a bad connection. This mainly affects triggering, and is corrected offline by averaging the ADC counts from signals in the same tower within ± 2 layers. Second, a channel can be "really-most-sincerely dead" if the anode wires are not being supplied with high voltage. This is a serious problem, as it affects the cathode signals.

In such cases, it is necessary to correct the cathode signal from that ganged layer by dividing

[2]This produces an audible hum or rattle. Loose wires can be indentified *in situ* by using a piece of surgical tubing as a stethescope.

it by the fraction of live anode wires in that layer. As is done for the high voltage correction, one correction factor is used for each ganged layer in each ϕ division.

4.3.5 Crosstalk Subtraction

In each θ-ϕ block, each θ-pad intersects every ϕ-pad, and vice-versa. The anode wires induce image charges on each of the pads. This is what we want to measure; however, an image charge on a given pad will capacitively induce a secondary image charge on every intersecting pad.

The correction for this effect is simple. For each block, a ϕ-sum (θ-sum) is made by adding together the ADC counts from each ϕ-pad (θ-pad), multiplied by their respective pad widths. Each θ-pad (ϕ-pad) pulse height is then corrected, by subtracting the ϕ-sum (θ-sum) times the θ-pad (ϕ-pad) width, times a capacitive constant of 0.0015.

4.3.6 Abnormal Pedestal Subtraction

Pedestal subtraction (described in Section 2.2.6) is performed online by the SHC electronics. In some cases this is not properly executed, making it necessary to subtract the pedestal values offline. If a section of data with erroneous pedestal values is detected (for example, by anomalously large numbers of SHC clusters), the pedestal values can be estimated by determining the most frequent number of ADC counts for each channel over a large number of events. These values +5 ADC counts are subtracted when the data are reanalyzed.

4.3.7 Monitor Tube Gain Correction

The gas gain of the SHC depends upon external factors such as atmospheric pressure and gas composition. Rather than measure these factors independently and calculate the gas gain, the monitor tubes described in Section 2.2.6 are used to measure the gas gain empirically.

Inside each monitor tube is a 0.55 μCi ^{55}Fe source. The ^{55}Fe nucleus decays via K-shell electron capture to ^{55}Mn. The subsequent L-K atomic transition emits an x-ray photon of 5.9 keV, which in turn ionizes the argon gas.

Monitor tube cathode and anode signals are read out with a separate CAMAC data acquisition system. The tube gains are determined in the offline analysis, and averaged to determine a correction factor for each run. This correction factor is applied to both the cathode and anode signals from the SHC.

4.4 Cluster Finding in Strip Geometries

We start by considering one θ-ϕ block. Each block consists, in each of the first two ganged cathode layers, of 32 ϕ strips intersecting 28 (inner block) or 36 (outer block) θ strips. These numbers are halved for cathode layers 3 to 5. As a first step, the information from each strip is summed vertically over the five layers.

As a shower proceeds through the block, the energy it deposits in each layer has an approximately Gaussian distribution in both ϕ and θ. The first step in shower reconstruction is finding the Gaussian peaks. This is performed in the following manner in each view:

1. The strip with the highest ADC counts is selected as the center of a peak, provided that posesses more than 3% of the ADC hits in that view.
2. The strips within three strips from the center are assigned to that peak. This is consistent with the typical RMS width of a shower.
3. The unassigned strip with the highest ADC counts is selected as the center of the next peak, subject to the 3% threshold.

This process is repeated until all the strips above the threshold have been assigned. If there are more than three peaks in any one view, the number of peaks is reduced by either

discarding the smallest peak (if it contains fewer than 10% of the ADC counts in that view), or merging the two closest peaks [51].

4.4.1 (1×0) and (1×1) Cases

Once the peaks have been selected in each view, they must be matched with the selected peaks in the perpendicular view. In the case where there is one peak in one view and no peak in the other view, the peak is attributed to noise and is discarded. The case with one peak in each view is just as trivial: the θ and ϕ peaks are combined, and promoted to the rank of cluster.

4.4.2 (1×2) and (1×3) Cases

The case where there is one hit in one view and two hits in the other view is somewhat more complicated.[3] We must distinguish between instances where there are two physical showers lined up in one view, and instances where there is one physical shower and one noise peak. To this end, we assign the following quantities, for example, for the (1×2) case:

$$\begin{aligned} C_1 &= |\mathrm{ADC}(\theta_1) - \mathrm{ADC}(\phi_1) - \mathrm{ADC}(\phi_2)| \\ C_2 &= |\mathrm{ADC}(\theta_1) - \mathrm{ADC}(\phi_1)| + \mathrm{ADC}(\phi_2) \\ C_3 &= |\mathrm{ADC}(\theta_1) - \mathrm{ADC}(\phi_2)| + \mathrm{ADC}(\phi_1), \end{aligned}$$

where $\mathrm{ADC}(\phi_1)$ represents the number of ADC counts assigned to the first ϕ peak, etc. C_1 corresponds to the case of two physical showers; C_2 corresponds to the case where the second ϕ peak is a noise peak; C_3 corresponds to the case where the first ϕ peak is a noise peak. The smallest quantity C corresponds to the correct choice.

[3] We distinguish cases with multiple peaks by labelling them "$(n \times m)$", where n is the number of θ peaks and m is the number of ϕ peaks. Thus the "(1×2) case" refers to one θ peak and two ϕ peaks, whereas the "(2×1) case" refers to two θ peaks and one ϕ peak.

The (1×3) and (3×1) cases are decided in exactly the same way as the (1×2) case, except that there are more possible combinations. Up to two peaks can be noise peaks, leading to seven quantities C to calculate.

4.4.3 (2×2) Case

The case (2×2) (and higher) presents an added difficulty: the possibility of matching the θ peaks with the wrong ϕ peaks, leading to a pair of "ghost" clusters. In an ideal detector, the number of ϕ and θ counts for a given cluster will be exactly the same, making identification easy. In a real detector they can be quite different, and even an ideal detector can be ambiguous when the incident energies are nearly the same.

We must also take into account the possibility of one noise peak in either the ϕ or the θ view.[4] Here there is the posibility of getting one ghost cluster: if one of the showers is very soft, there is some chance of mistaking the arrangement of hits for a (1×2) or (2×1) case.

For the (2×2) case there are thus six quantities C to calculate: two where there are no noise peaks, and four where there is one noise peak.

Figure 4-1 shows, for the (2×2) case, the percentage of events with ghost clusters as a function of photon energy, when the energy of a second photon in the same block is 5 GeV. A sample of 1000 events was fully simulated for each point, with the 5 GeV photon generated at ($\theta = 85°$, $\phi = 7.5°$), and the photon of varying energy generated at ($\theta = 75°$, $\phi = 22.5°$). Events with charged tracks from a photon conversion to e^+e^- were discarded. Rates for (2×2) misidentification (i.e. θ hits matched with wrong ϕ hits) is shown, along with the rate for (2×1) or (1×2) misidentification.

[4] We never consider cases where there are noise peaks in both views; they are too difficult to distinguish from real peaks, and not nearly as likely.

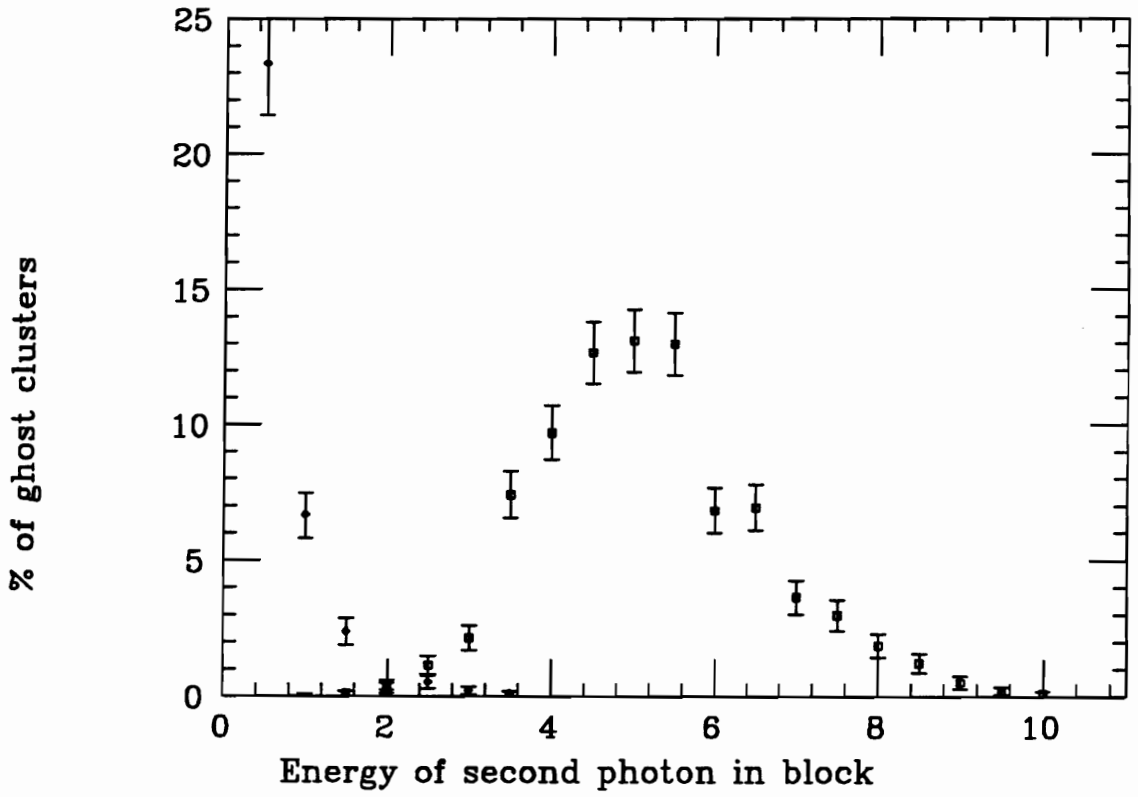

Figure 4-1: Percentage of ghost clusters vs. photon energy ((2×2) case). Other photon has 5 GeV of energy. Square points denote (2×2) ghosts; diamonds denote (2×1) or (1×2) ghosts.

4.4.4 Higher Order Cases

The AMY clustering routines can handle up to the (3×3) case, for which there are 48 possible combinations. Any larger number of peaks would lead to hundreds of combinations per case. While this would be numerically tractable, the chances for getting a wrong combination with a lower C value than the correct combination increase dramatically.

In the case where the number of ϕ or θ peaks could not be adjusted to fewer than four, the clustering routines are not called. One cluster is assigned to the entire block. The energy of the cluster is the sum of the pad energies; the ϕ and θ values are the weighted mean values of the assigned peaks.

To reflect the increased ambiguity for higher-order cases, a quality value is assigned to each cluster based on its clustering case. Each case, with its combinatorics and quality value, is listed in Table 4-1.[5]

4.5 Boundary Matching

When a shower straddles one of the 84 block boundaries, the energy deposition on either side is reconstructed separately by the clustering routine. It is therefore necessary to recognize dismembered showers and reunite them.

For each cluster, we first determine whether any of its θ or ϕ pads is at a block boundary. We also record the distance from each cluster centroid to the nearest boundaries in the θ and ϕ directions.

If a cluster is at a block boundary, we attempt to merge it with any cluster in the adjacent block within 3° of the same boundary. Suppose our cluster is against a ϕ (θ) block boundary:

[5] Q_1 denotes the quality of the cluster under consideration. If it is merged with another cluster at a boundary (see Section 4.5), the quality of the second cluster is denoted Q_2.

Table 4-1: Clustering cases.

Case	Combinations	Quality
(1×1)	1	1
$(1 \times 2), (2 \times 1)$	3	2
$(1 \times 3), (3 \times 1)$	7	2
(2×2)	6	4
$(2 \times 3), (3 \times 2)$	17	8
(3×3)	48	16
$(\geq 4\times$ anything)	—	$32 + Q_1$
Boundary match	—	$64 + Q_1 + Q_2$
Noise cluster	—	$16384 + Q_1$

if any of its θ (ϕ) pads overlaps (in θ (ϕ) coverage) any of the θ (ϕ) pads in the neighboring cluster, the clusters are merged.

Examples of this procedure are shown in Figure 4-2. In Figure 4-2(a), two clusters are merged at a θ boundary. The highest θ and ϕ pads for each cluster are shown in black; the other pads assigned to each cluster are shown in grey. Figure 4-2(b) shows two clusters that are not merged at a boundary. The ϕ pads do not overlap.

4.6 SHC Calibration

Once clusters have been recognized in the SHC, additional corrections must be applied for the energy and position of a cluster to be accurately measured.

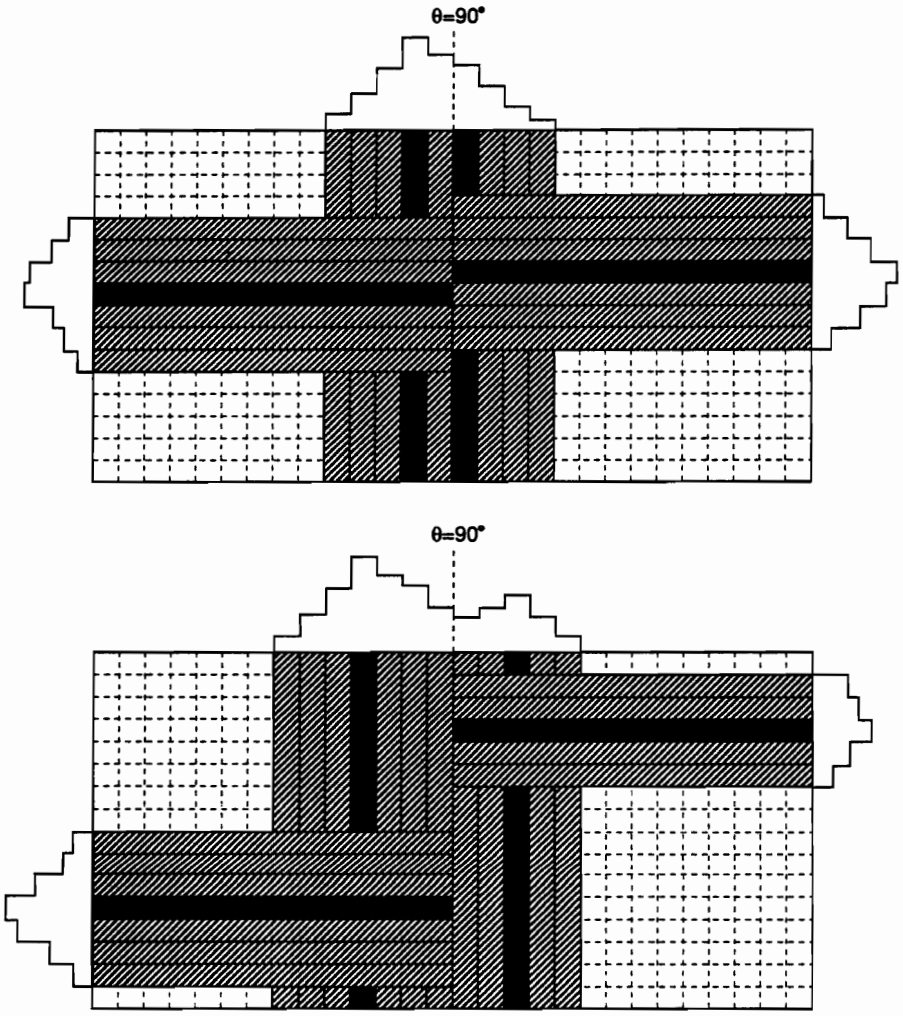

Figure 4-2: (a) Two clusters merged, (b) Two clusters not merged at a boundary.

4.6.1 SHC Magnetic Field Correction

Because showers are composed largely of charged particles, the shape of a shower in the AMY SHC is strongly affected by AMY's intense magnetic field. The non-parallel B-field components are understood to have a particularly distorting effect. Since these field components are strongest near the edges of the SHC, the magnetic field effects depend upon polar angle.

The magnetic field correction function has the curious form [52]

$$\delta\theta(\theta) = a \cdot \left[\mathrm{erf}\left(\frac{|\theta - 90°|}{b}\right) \mathrm{erf}\left(\frac{|\theta - 90°| - c}{d}\right) \frac{|\theta - 90°|}{90° - \theta} \right] - e, \tag{4.2}$$

where a, b, c, d, and e are constants (empirically determined for each ganged cathode layer as well as for the cathode sum), and we have employed the error function

$$\mathrm{erf}(x) = \frac{2}{\sqrt{\pi}} \int_0^x e^{-t^2} dt. \tag{4.3}$$

The physical mechanism for the distortion of showers in the AMY magnetic field is abundantly clear, but the inspiration behind this empirical functional form remains a mystery.

4.6.2 Leakage Correction

The SHC comprises 14.4 radiation lengths at $\theta = 90°$. High-energy showers will deposit some θ-dependent fraction R of their energy beyond the outer radius of the SHC, where it cannot be sampled. The more energetic the shower, the more leakage occurs. The amount of energy leakage also depends upon the polar angle: because the SHC has a constant cylindrical thickness, its apparent thickness varies as $1/\sin\theta$.

The amount of energy leakage has been determined using the EGS4 Monte Carlo, and parametrized by the following empirical relationship [53]:

$$\log_{10} R = c \log_{10} E + \log_{10}(a\theta - b) - c, \tag{4.4}$$

where E and θ are the incident energy and polar angle of a shower. The constants a, b, and c were determined from the Monte Carlo. They are given in Table 4-2.

Table 4-2: SHC leakage parameters.

θ (degree)	E (GeV)	a	b	c
$66.3 \leq \theta \leq 90.0$	$E \geq 10$	0.00139	0.0091	0.276
$66.3 \leq \theta \leq 90.0$	$E < 10$	0.00139	0.0091	0.380
$\theta < 66.3$	$E \geq 10$	0.00270	0.0960	0.276
$\theta < 66.3$	$E < 10$	0.00270	0.0960	0.380

4.6.3 Saturation Correction

As a shower passes through a layer of the SHC, the electric field around the anode wires becomes shielded by the ions produced in avalanche discharges. The more primary (i.e. shower) electrons pass through a given tube, the greater the shielding of the anode wire. The amount of ions produced in each avalanche depends upon the local ion density; the resulting signal induced on the anode wire is thus not strictly proportional to the number of electrons passing through the layer. This saturation effect becomes important in the region of shower maximum for showers above 5 GeV.

The relationship between the true and measured energies can be expressed by the formula [53]

$$E_{\text{measured}} = C_1 E_{\text{true}} - C_2 E_{\text{true}}^2, \tag{4.5}$$

where $C_1 = 1/(1-S)$, $C_2 = C_1 S/E_{\text{true}}$, and S is the saturation ratio for the energy E_{true}. The saturation ratio can be determined by comparing the actual and measured energies for acollinear electron and Bhabha events. The true energy can then be expressed as

$$E_{\text{true}} = \frac{C_1 - \sqrt{C_1^2 - 4C_2 E_{\text{meas}}}}{2C_2}. \tag{4.6}$$

Chapter 5

Event Selection

The AMY data sample is, by 1993 standards, gigantically large. AMYVAX feeds every single AMY trigger to the FACOM, where they are stored in the RAW database. The FACOM digests these data, selecting events to be analyzed (which are put in the SEL database), and reconstructing their shower and tracking information. Reconstructed events are placed in the REC database.

Five (partly overlapping) data samples are selected from the REC database: 1) The QED database, described in detail below, contains events likely to arise from QED processes. 2) The HAD database contains events likely to arise from hadronic production. 3) The ELW database contains events likely to arise from electroweak processes. 4) The LWM database contains events with a low multiplicity of charged tracks. 5) The PTC database contains events with large hits in the PTC or ESC. Any event selected for one or more of these data samples is also placed in the DST database, the basic physics data sample for AMY.

5.1 QED Analysis

Photon final state events are selected from the QED database; here we will review the QED selection criteria. There are four categories of events stored in this database, which we will describe in detail: CDC events, SHC events, ESC events, and two-photon[1] events.

1. A CDC event contains at least one and no more than ten "good" charged tracks. A "good" track is defined as having more than nine axial hits and more than six stereo hits, and passing within 5 cm of the beam axis and within 10 cm of $z = 0$. A CDC event must *not* be a cosmic ray event, which has at least one muon track with $-6\,\text{ns} < T_\mu < 40\,\text{ns}$.
2. An SHC event either has at least two SHC clusters with energies above 3 GeV, or at least one SHC cluster with energy above 5 GeV.
3. An ESC event has at least one ESC track with energy above 10 GeV.
4. A two-photon event has at least one ESC track with energy above 5 GeV and has at least one CDC track.

5.2 Photon Recognition

The cluster recognition software was described in Section 4.4. Any deposition of energy in the SHC can be reconstructed as a cluster. Since this includes many forms of SHC noise, it is necessary to impose a set of cuts on each cluster to distinguish SHC noise from real photons.

The following criteria were found to be effectively 100% efficient for recognizing simulated showers above 10 GeV:

[1]This unfortunately named process is not to be confused with the $e^+e^- \to \gamma\gamma$ process under study. "Two-photon" refers to the collision of two *virtual, intermediate state* photons, and not to the production of two real, final state photons.

- Its energy must be greater than 1.0 GeV.
- It must have at least three layers with both θ and ϕ hits.
- It may not be a complicated cluster (worse than 3×3 case).
- It may not have more than 70% of its energy in any of ganged cathode layers 1 to 4, nor more than 85% of its energy in ganged cathode layer 5.

The last criterion is looser for ganged cathode layer 5 in order to improve efficiency for late showers.

Any cluster passing these cuts is called a "good" cluster.

These cuts are not meant to recognize photons in arbitrary situations, but are merely meant to be highly efficient in events consisting of a few photons in the final state. Some real photons may fail these criteria (particularly very soft photons), but the analysis will not suffer: event selection does not require that all photons be recognized, and unidentified photons will usually be restored by eyescanning.

5.3 Event Preselection Criteria

Events are selected from the QED database by software, and placed into preliminary categories. After selection, every single event in every preselection sample is eyescanned on a VAXstation 3100 using the AMY display program. Eyescanning ensures that there are no unreconstructed CDC tracks, cosmic ray showers, or other gross irregularities. Individual clusters are also scanned to distinguish real photons from noise clusters and off-vertex background, by looking for Gaussian transverse profiles over several cathode layers that project from the interaction point in both θ and ϕ (soft photons failing the photon recognition criteria are reclaimed in this way). Over 38,000 events were scanned by the author in the preparation of this thesis.

Events containing only bona fide photons in the final state are listed in a large table, along with the energy and angles of each photon, status information about the detector, and MUO, CDC, and endcap hits. Final analysis is performed using information from this table, without making reference to (or being constrained by) the preselection categories or criteria.

5.3.1 General Event Filter

Once the photon clusters in one event have been recognized, the entire event is subjected to the following criteria:

- At least 25% of the total analyzed SHC energy must be assigned to "good" clusters.
- At least one of the two largest clusters must be "good", and have an energy of at least 4 GeV.
- Raw θ and ϕ total energies must agree to within a factor of three.
- Raw θ and ϕ total energies must each agree with the total raw anode energy to within a factor of four.

5.3.2 Photon Preselection Sample

Events containing only photons in the final state are preselected according to the following criteria:

- It must pass the general event filter.
- There may be no charged tracks.
- There must be at least two "good" clusters in the SHC.

- They must have energies of at least $E_{\rm beam}/3$ and $E_{\rm beam}/6$.
- If the clusters have an acoplanarity angle of $\geq 3°$, there may be no muon tracks in the event (to reject cosmic ray backgrounds).

5.3.3 Supplementary Event Samples

In order to ensure that no neutral final state events fail the event selection, several supplementary event samples are selected from the events not included in the photon preselection sample. These include:

- **Single photon monojet:** Any "good" cluster of at least $E_{\rm beam}/3$, with no charged tracks.
- **Loose Acoplanar event:** One "good" cluster of at least $E_{\rm beam}/3$, plus any other "good" cluster, with no charged tracks.
- **One track event:** Any event passing any set of main preselection criteria, with one charged track.
- **Loose $\gamma\gamma$ event:** One "good" cluster of at least $E_{\rm beam}/4$, plus another cluster of at least $E_{\rm beam}/20$. The clusters must have an acollinearity of no more than 15°. There must be no charged tracks with a transverse momentum greater than 4 GeV.

Events in these categories are not required to pass the general event filter.

5.3.4 $\gamma \rightarrow e^+e^-$ Sample

A $\gamma \rightarrow e^+e^-$ conversion candidate must satisfy the following criteria:

- It must pass the general event filter.

- There must be two opposite-sign charged tracks in the event.
- The charged tracks must have an opening angle of at most 10°.
- There must be one "good" neutral cluster of at least $E_{\text{beam}}/3$ in the SHC.
- The summed momentum of the tracks must have an acollinearity of at most 10° with the neutral cluster.

5.4 Final Event Selection Criteria

Once the preselection samples have been eyescanned and the relevant clusters identified, final selection samples are produced. Final selection $e^+e^- \to \gamma\gamma$ and $e^+e^- \to \gamma\gamma\gamma$ events are permitted to have charged tracks, provided that they are extraneous to the event (i.e. they are from downstream or cosmic sources). All photons in an accepted event are required to be within $45° \leq \theta \leq 135°$. The final selection criteria are as follows:

- $e^+e^- \to \gamma\gamma$ **events:** Two photons of at least $E_{\text{beam}}/3$, with an acollinearity of no more than 10°.
- $e^+e^- \to \gamma\gamma\gamma$ **events:** Three photons.
- **Acoplanar** $\gamma\gamma$**:** Exactly two photons with an acoplanarity of at least 3°. No endcap hits greater than 1 GeV.
- **Low Energy Collinear** $\gamma\gamma$**:** Two photons of at most $E_{\text{beam}}/2$, with an acoplanarity of less than 3°, and an acollinearity of less than 10°.

Note that individual events are permitted to be included in more than one final selection data sample. For example, an event with two hard, collinear photons and a third, soft photon will likely be included in both the $e^+e^- \to \gamma\gamma$ sample (provided the event passes the

energy and angle cuts) and the $e^+e^- \rightarrow \gamma\gamma\gamma$ sample (provided the third photon is tagged by the SHC).

Chapter 6

Analysis of $e^+e^- \rightarrow \gamma\gamma$

The process $e^+e^- \rightarrow \gamma\gamma$ is commonly used as a test of QED. Experiments at PEP (refs. [54] to [56]), PETRA (refs. [57] to [67]), TRISTAN (refs. [68] to [74]), and LEP (refs. [75] to [80]) have shown good agreement with QED; thus if we wish to search for deviations we must use very high integrated luminosities.

We must measure two basic properties for this process: the integrated and the differential cross sections. The integrated cross section, measured in units of area, can be thought of as the "size" of the interaction: it quantifies the average rate of event production at a given collision energy. The differential cross section describes the angular distribution of these events, and is analogous to the "shape" of the interaction.

The measurement of the integrated cross section for $e^+e^- \rightarrow \gamma\gamma$ is not as simple as counting up the events and dividing by the integrated luminosity. First, there are corrections we must take into account, representing the effect of the selection cuts, the infirmities of the detector and the inefficiencies in the data taking.

Second, the data must be corrected by dividing out the radiative deviations from the Born cross section calculated in Chapter 1, and comparing the results to the Born cross section.

This restores the simple $1/s$ scaling behavior of $\mathcal{O}(\alpha^2)$ QED, making it possible to compare the data to those of other experiments at different energies.

6.1 Correction of $e^+e^- \rightarrow \gamma\gamma$ Data

If the vacuum were content to produce $e^+e^- \rightarrow \gamma\gamma$ events using only $\mathcal{O}(\alpha^2)$ QED, and all events were produced at the exact center of an ideal detector, both measured photons in each event would be exactly back-to-back. In the real world, this is never the case. No matter how we bin the data, some events will cast their photons into bins that are not symmetric about a polar angle of 90°.

This presents an apparent problem for comparison to the Born cross section: the Born cross section as given in Equation 1.3 expresses the number of $e^+e^- \rightarrow \gamma\gamma$ *events* as a function of polar angle, but we cannot assign an unambiguous polar angle to any event in the data sample. On the other hand, simply multiplying the Born cross section by a factor of two gives us the distribution of *photons* from $\mathcal{O}(\alpha^2)$ QED, which is directly comparable to the distribution of photons in the data sample.

In order to compare our data sample to the Born cross section, we first correct our data with the following prescription prior to binning:

- Each photon is given a weight of one half, to convert the photon distribution to an effective event distribution.
- The weight is multiplied by one minus the fraction of events expected from background sources.
- The weight is divided by $(1 + \delta(\theta_\gamma))$ of Equation 1.21, to correct for radiative effects.
- The weight is then divided by a function $\epsilon(\theta_\gamma)$, to correct for the detection efficiency.

- The weight is finally divided by the integrated luminosity, to provide the correct normalization.

The expression for the measured cross section in the i^{th} bin is thus given by:

$$\frac{d\sigma_i}{d\Omega} = \sum_{j=1}^{n} \frac{1 - f_b}{2L\epsilon(\theta_j)[1 + \delta(\theta_j)]|\Delta \cos\theta_j|2\pi}, \tag{6.1}$$

where n indicates the number of photons in the i^{th} $\cos\theta$ bin, f_b represents the background fraction, and L denotes the integrated luminosity. The correction factors f_b, $\delta(\theta)$, and $\epsilon(\theta)$ are discussed in Sections 6.2 to 6.4.

6.2 Background Processes

6.2.1 Misidentified Bhabha Events

Misidentified Bhabha scattering events constitute the main background to $e^+e^- \rightarrow \gamma\gamma$. Occasionally, the high voltage power supplies to the CDC will trip while the detector is in operation. Other times, large amounts of CDC noise will prompt the removal of CDC information from an event. In either case, the showers in the unaffected SHC will typically pass the $e^+e^- \rightarrow \gamma\gamma$ selection criteria. Events with incomplete CDC information are easily tagged, since the HV status of the CDC is recorded in the AMY data. We would like to discard these events, but we would also like to keep the concurrent $e^+e^- \rightarrow \gamma\gamma$ events.

Fortunately, misidentified Bhabha events are not completely indistinguishable from $e^+e^- \rightarrow \gamma\gamma$ events. The Bhabha electrons, of course, are still bent by the magnetic field, which produces an acoplanarity of around 2.5° in the SHC, whereas $e^+e^- \rightarrow \gamma\gamma$ events tend to have an acoplanarity close to zero. Also, partial tracks are sometimes visible in the CDC, and tracks can sometimes be tagged by the ITC or VTX.

Any event with partial tracks is called a misidentified Bhabha event. Any event with low voltage or with no CDC information is also called a misidentified Bhabha event, if it has an acoplanarity of 1° or greater.

Based upon the acoplanarity distributions for $\gamma\gamma$, Bhabha, and radiative Bhabha events, and upon the number of misidentified Bhabha candidates, we estimate a net background of 5 events in the entire data sample. The background fraction due to Bhabha events is 0.1%.

6.2.2 Hadronic and Two-Photon Backgrounds

Hadronic backgrounds were estimated with a 247 pb^{-1} fully simulated sample of LUND 7.2 events. This sample was searched for events containing only neutral particles in the final state. The remaining events were searched for photons and π^0's, combining together any such showering neutrals with an opening angle of less than 3°. The surviving events were subjected to the $e^+e^- \to \gamma\gamma$ selection criteria; no candidate events survived.

Two-photon backgrounds (see footnote in Section 5.1) were estimated with a 200 pb^{-1} generated sample of HERWIG 5.5 events. No events were found to satisfy the $e^+e^- \to \gamma\gamma$ selection criteria.

Since no events were found from either process in 200 pb^{-1}, it is 95% certain that the expected signal is fewer than 3 events total. We therefore estimate the background fraction from hadronic and two-photon sources to be zero, and the total background fraction to be $f_b = 0.001$.

6.3 Radiative Corrections, Revisited

In Section 1.1.7 we represented the $\mathcal{O}(\alpha^3)$ cross section for $e^+e^- \to \gamma\gamma$ by writing each radiative correction as the Born cross section times some factor $(1 + \delta)$. These terms are

generally dependent upon polar angle and CM energy; thus, if we wish to remove the third-order effects from our data, we must calculate the radiative corrections for all relevant CM energies at all polar angles in the fiducial range.

Generator-level Monte Carlo studies were carried out at CM energies from 50 to 64 GeV at 2 GeV intervals. Approximately $10\,\mathrm{fb}^{-1}$ of data were generated at each energy. Differential cross sections were produced for each data set by subjecting the final state photons to an energy cut of $E_\gamma > E_{\mathrm{beam}}/3$, and an acollinearity cut of $\zeta < 10°$. Each generated cross section was then divided by the Born cross section, averaged pairwise over symmetric bins, and fit to a sixth-order polynomial using even powers only.

The resulting functions differed from the 58 GeV $(1 + \delta)$ function by less than .5% at any polar angle, and by .25% overall. The typical deviation at each point was around .3%. Since this is well below the statistical uncertainty for all data taken at energies other than 58 GeV, the 58 GeV radiative correction is used for all data.

The 58 GeV $(1 + \delta)$ function is given by:

$$(1 + \delta) = 0.893 + 3.434 \times 10^{-5}\vartheta^2 - 2.059 \times 10^{-8}\vartheta^4 + 6.312 \times 10^{-12}\vartheta^6, \qquad (6.2)$$

where $\vartheta \equiv \theta - 90°$ is measured in degrees. This function is shown in Figure 6-1, along with the generator-level $\mathcal{O}(\alpha^3)/\mathcal{O}(\alpha^2)$ ratio.

6.4 The Efficiency Function ϵ

There are several reasons why we might fail to recognize an $e^+e^- \to \gamma\gamma$ event. Many of these, including late photon conversion to e^+e^- in the SHC, early photon conversion to e^+e^- in the beam pipe, and angular smearing at the fiducial limit are faithfully reproduced by the AMY simulator. We express these with a single efficiency function ϵ_0.

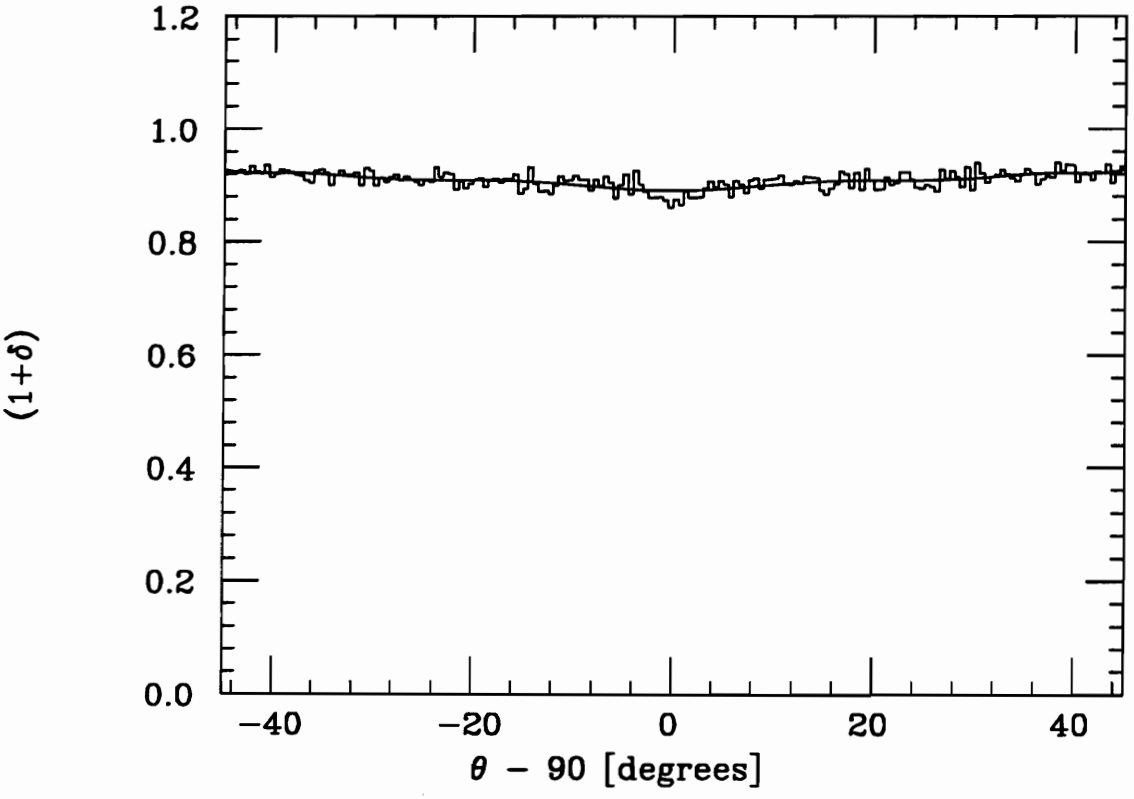

Figure 6-1: Radiative correction function $(1 + \delta)$ at 58 GeV.

Other sources of inefficiency have to be put in "by hand". These include trigger inefficiency, event losses to external sources such as cosmic ray crossings and spurious downstream tracks, SHC inefficiency and longitudinal event vertex smearing. AMY 1.0 data have an additional source of inefficiency: the thicker beam pipe causes more events to be lost to $\gamma \rightarrow e^+e^-$ conversions.

The total efficiency function ϵ is then a product of ϵ_0 and five other efficiency factors, which are discussed in the next several sections.

6.4.1 Monte Carlo Efficiency Function ϵ_0 for $e^+e^- \rightarrow \gamma\gamma$

A fully simulated sample of $1.820\,\mathrm{fb}^{-1}$ was produced for the $e^+e^- \rightarrow \gamma\gamma, \gamma\gamma\gamma$ process. After the analyzed data were filtered according to the final selection criteria for $e^+e^- \rightarrow \gamma\gamma$, they were divided by the Born cross section times $(1 + \delta)$. The resulting distribution was then averaged pairwise over opposite bins (to symmetrize the distribution about $\theta = 90°$), and fit to a sixth-order polynomial using even powers only. The resulting efficiency function is

$$\epsilon_0 = 0.93734 - 9.60426 \times 10^{-6}\vartheta^2 + 1.13004 \times 10^{-7}\vartheta^4 - 7.01408 \times 10^{-11}\vartheta^6, \qquad (6.3)$$

where ϑ is measured in degrees. The Monte Carlo sample has a statistical uncertainty of 0.4% overall.

6.4.2 Trigger Efficiency ϵ_{trig}

SHC Trigger Efficiency from $e^+e^- \rightarrow \gamma\gamma$

Triggering for neutral final states is performed using the signals from the SHC anode wires. These signals are combined to produce triggers 8, 9, and 19, discussed in Section 2.2.6.

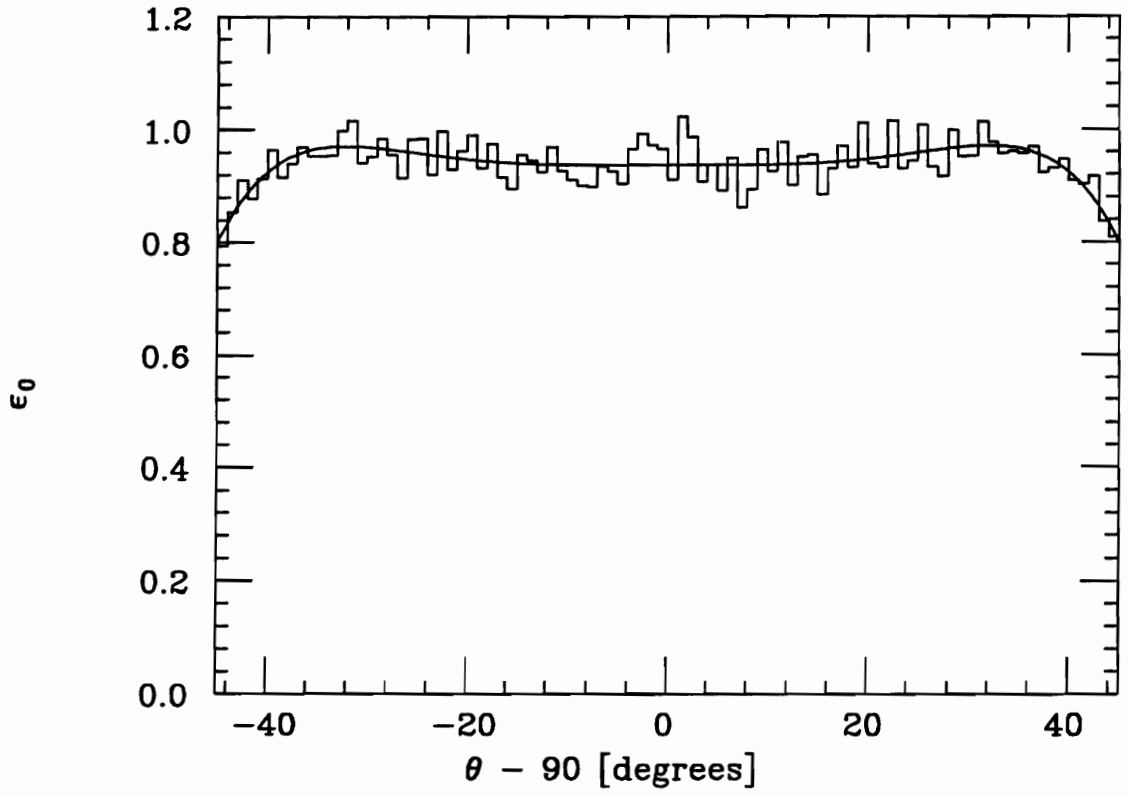

Figure 6-2: Efficiency function for simulated data.

We have seen that these triggers are highly redundant, i.e. that events satisfying one of these triggers are likely to satisfy one or both of the others. Table 6-1 shows the relative efficiency of these triggers for $e^+e^- \rightarrow \gamma\gamma$ events in various running periods. Of all the events found with missing SHC triggers, three were found with no SHC triggers activated (for some unknown reason, ESC triggers were activated in each case). These events were recorded prior the activation of trigger 9.

Table 6-1: $e^+e^- \rightarrow \gamma\gamma$ SHC trigger efficiency.

Run Period	Trigger 8	Trigger 9	Trigger 19
2733 - 7795	0.999	N.A.	0.994
7889 - 10896	1.000	N.A.	0.983
10983 - 11805	0.989	N.A.	0.975
11821 - 12639	1.000	N.A.	0.987
12650 - 14579	1.000	1.000	0.983
14594 - 15631	0.999	1.000	0.996

SHC Trigger Efficiency from Bhabha Events

We must also have an accurate estimate of the total efficiency for all of these triggers combined. It is not sufficient to multiply the relative efficiencies of the triggers; failure rates for these three triggers could easily be strongly correlated. Bhabha scattering events, which trigger independently on the tracking triggers and have SHC signatures nearly identical to $e^+e^- \rightarrow \gamma\gamma$ events, are ideal for this purpose. We found 24 Bhabha events out of a sample of 54,744 events inside $|\cos\theta| \leq 0.73$ that had no SHC triggers activated, 19 of which fall into a brief set of runs (9158-9172). These runs (containing some $170\,\mathrm{nb}^{-1}$ of integrated luminosity) were for this reason not included in the present analysis.

Effect of Photon Punch-Through on Triggering

One potential inefficiency for $e^+e^- \rightarrow \gamma\gamma$ triggering that cannot be estimated using Bhabha events is the effect of photon punch-through. Electrons begin to shower immediately in the lead; photons will pass through some amount of material before converting to an e^+e^- pair.

In order for photon punch-through to cause an event to fail trigger bit 8, we estimate that both photons in an event would have to penetrate at least beyond anode layer 10.[1] At $\theta = 90°$, about 59.5% of the hard photons will penetrate each 3.5 mm layer of lead, thus there is about 1 chance in 12,000 of both photons passing through at least 9 layers of lead at 90°. Considering that at least one of the photons would have to penetrate even further, and that most of the events will be well away from the center of the SHC, we do not expect any trigger failures due to photon punch-through.

Total Trigger Efficiency

The only indication we have of possible event loss due to SHC trigger failure is the three $e^+e^- \rightarrow \gamma\gamma$ events observed with no SHC triggers activated. We will assume that there were another six events that went completely untriggered. We therefore assign a combined trigger efficiency for triggers 8, 9, and 19 of $\epsilon_{\text{trig}} = 0.999$, but conservatively assign an uncertainty to this value of 0.1%.

6.4.3 Effect of $\gamma \rightarrow e^+e^-$ Conversion in AMY 1.0

The preceding section noted the possibility that a photon might pass through a large portion of the SHC before converting to an e^+e^- pair and initiating an electromagnetic shower; in Appendix B we consider the effect of photon conversion to e^+e^- *before* entering the SHC.

[1] The amount of energy deposited in the first 6 anode layers of one shower after the initial conversion is typically above the threshold for trigger bit 8.

Photon conversion to charged tracks is the main source of inefficiency for neutral final states, other than fiducial cuts. We have already determined the efficiency function ϵ_0 for AMY 1.5 from the $1.82\,\mathrm{fb}^{-1}$ simulated sample; this implicitly includes the effect of photon conversion with the beryllium beam pipe. Data taken with AMY 1.0 (and the 1990 data of of AMY 1.5), on the other hand, have a higher conversion rate, due to the thicker aluminum beam pipe (see Appendix B). We must therefore include a supplemental efficiency function for these data. This function, ϵ_{conv}, is given by:

$$\epsilon_{\mathrm{conv}}(\theta) = \frac{1 - 2C_1/\sin(\theta) + C_1^2/\sin^2(\theta)}{1 - 2C_2/\sin(\theta) + C_2^2/\sin^2(\theta)}, \tag{6.4}$$

where $C_1 = 0.0278$ is the $\gamma \to e^+e^-$ conversion rate for AMY 1.0 and $C_2 = 0.0187$ is the conversion rate for AMY 1.5. We make the reasonable assumption that the photons in an $e^+e^- \to \gamma\gamma$ event will end up in nearly opposite angular bins. The value of this efficiency function ranges from 0.982 at $\theta = 90°$ to 0.974 at $\theta = 45°$. The error on these values is 0.05%.

For AMY 1.5 events, we define $\epsilon_{\mathrm{conv}} = 1.0$.

6.4.4 Effect of Longitudinal Event Vertex Distribution

Electron and positron bunches in TRISTAN are focused in the transverse directions at the interaction points; however, no focusing is performed in the longitudinal direction. Each bunch has a Gaussian profile with $\sigma = 1\,\mathrm{cm}$, which leads to a longitudinal distribution of event vertices with $\sigma = 1\,\mathrm{cm}$. This has been confirmed experimentally [81].

This shifting of the interaction point has a deleterious effect on event selection. Consider an event where two photons are produced back-to-back at a polar angle of 45°. If the actual event vertex is longitudinally shifted by $1\,\sigma$ in either direction, both photons will gain (or both will lose) 0.3° of polar angle as measured by the SHC. Either way, one photon will be

pushed outside of a fiducial cut of 45°, causing the entire event to fail the selection criteria.[2] Therefore, we would expect to lose events near the fiducial cut due to vertex shifting.

Let us consider also the effect of vertex shifting on those occasional events with an acollinearity of close to 10°. The acollinearity angle between the two hard photons is primarily due to the presence of a radiated photon, which is likely to be emitted close to the beam axis. If we displace the vertex along the z-axis, we will either increase or decrease the acollinearity of each event. Each event is as likely to lose as to gain acollinearity, but because there are more events just below 10° than just above 10°, we would expect a net loss of events. Furthermore, this effect on acollinearity would be greatest for events near $\theta = 90°$. We would thus expect a small inefficiency for events near 90° due to vertex shifting.

Since vertex smearing is not included in the AMY simulator, it is necessary to put it in "by hand", after the fact. For each event in a 10 fb^{-1} generated, smeared sample of $e^+e^- \to \gamma\gamma, \gamma\gamma\gamma$ events, a vertex displacement was randomly generated from a Gaussian with $\sigma = 1\,\text{cm}$. The impact point for each photon was then longitudinally shifted by that distance near the region of shower maximum (specifically, a cylindrical radius of 90 cm), and the photon θ-angle recalculated. The shifted sample was then subjected to the same cuts as the unshifted sample; the ratio of the two final samples is shown in Figure 6-3.

This ratio was then averaged pairwise over opposite bins, and fit to a eighth-order polynomial using even powers only. The resulting efficiency function is

$$\epsilon_{\text{vert}} = 0.9967 + 5.989\times10^{-5}\vartheta^2 - 1.989\times10^{-7}\vartheta^4 + 2.041\times10^{-10}\vartheta^6 - 6.402\times10^{-14}\vartheta^8, \quad (6.5)$$

where ϑ is again measured in degrees.

[2] Clearly, this argument would apply regardless of what specific fiducial cut is used. The effect on polar angle measurement is proportional to $\sin\theta$ in the ESC, however, so this does not pose a significant problem for luminosity measurement.

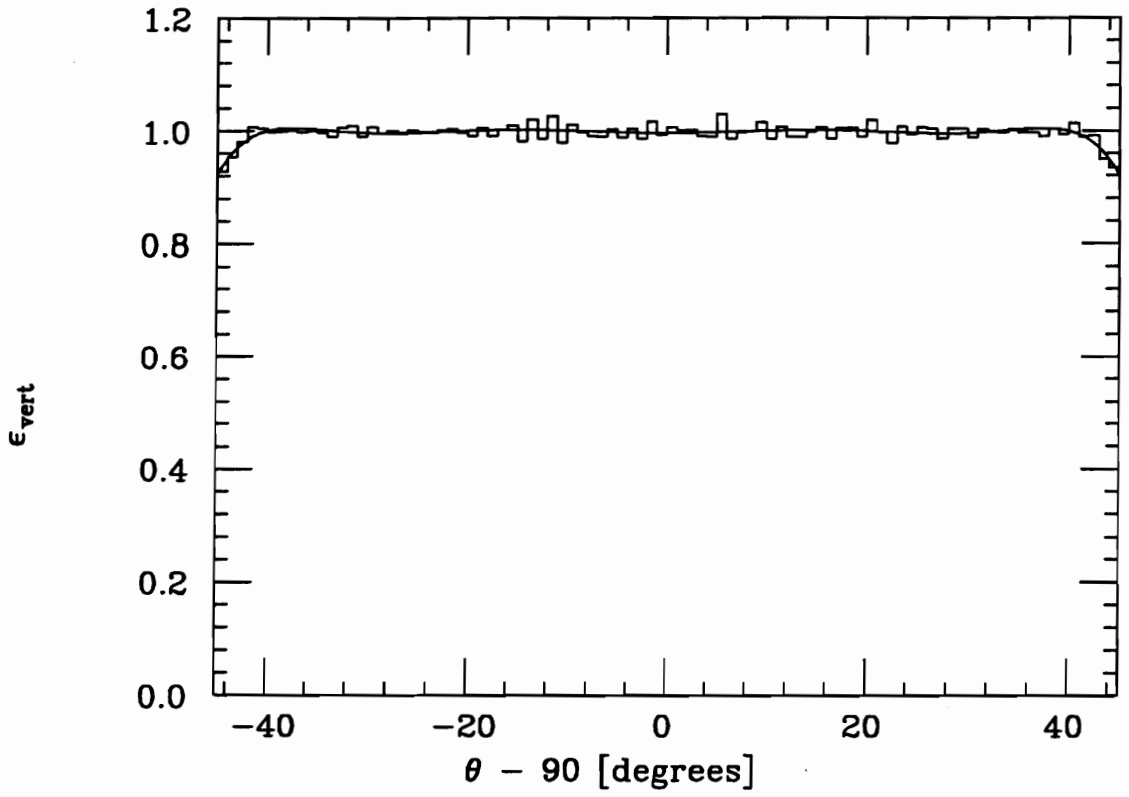

Figure 6-3: Efficiency function for vertex shifting.

6.4.5 SHC Hardware Inefficiency

We must consider the possibility of an $e^+e^- \rightarrow \gamma\gamma$ event failing the selection criteria due to SHC hardware failure. This is difficult to estimate: any lost events would be difficult to recoup, and Bhabha scattering events would likely be lost in the same way.

One known hardware effect not reproduced by the simulator is occasionally poor shower development at sextant boundaries in ϕ. In the real SHC, there are small ($\sim$ 3 mm) gaps between neighboring sextants. These gaps are filled with brass shim to initiate shower development; however, the incomplete cathode pad coverage makes these areas somewhat less sensitive than is represented in the simulator.

We found 17 events within $45° \leq \theta \leq 135°$ and $\zeta < 10°$, where at least one photon failed the energy cut of $E_{\rm beam}/3$ due to poor development, within 1° of a sextant gap.

We must also mention three events which will be described in Section 9.2.2. These events are apparently $e^+e^- \rightarrow \gamma\gamma$ events with inexplicably low anode pulse heights. We will assume that few events of this type eluded event selection or triggering.

We assign an efficiency factor of $\epsilon_{\rm SHC} = 0.997$ to compensate for events lost to SHC inefficiency. We estimate an error of 0.1% on this value.

6.4.6 External Sources of Inefficiency

Several external factors can lead to the loss of events. Most common is the presence of spurious charged tracks, which are caused by spent electrons passing through the detector during the gate time of an $e^+e^- \rightarrow \gamma\gamma$ event. A total of 14 such events were found; all were restored to the data set. It is unlikely that more than a few such events could escape selection; we therefore estimate the inefficiency to be less than 0.1%.

It is also possible that a cosmic ray might pass through the CDC during the gate time of an $e^+e^- \to \gamma\gamma$ event. One such event was found, although the CDC analysis program failed to reconstruct any tracks. In the event that tracks from a coincidental cosmic ray are recontructed, it is likely that the event will be selected in a supplementary event sample, provided that the γ showers pass the $e^+e^- \to \gamma\gamma$ criteria. We conclude that no events of this type would fail selection.

Finally, we consider the possibility of a second interaction during the same beam crossing as an $e^+e^- \to \gamma\gamma$ event. Averaged over the lifetime of AMY, fewer than about two out of every 100,000 beam crossings produces a trigger. Even if all of these triggers contained some sort of physics, there is only about an 11% chance that even one $\gamma\gamma$ event would be lost to a coincidental interaction.

The efficiency factor due to external sources of inefficiency is $\epsilon_{\rm ext} = 0.999$, with an error of 0.001.

6.4.7 Total Efficiency Function for $e^+e^- \to \gamma\gamma$

The total efficiency function for the process $e^+e^- \to \gamma\gamma$ is given by the equation:

$$\epsilon(\theta) = \epsilon_0 \cdot \epsilon_{\rm trig} \cdot \epsilon_{\rm vert} \cdot \epsilon_{\rm conv} \cdot \epsilon_{\rm SHC} \cdot \epsilon_{\rm ext}. \tag{6.6}$$

The total efficiency correction factor is about 8.5% near $\theta = 90°$, dropping to around 2.5% near $\theta = 60°$, and rising to around 35% at the fiducial extreme. We estimate an overall fractional systematic uncertainty of 0.7% for the efficiency function.

6.5 Comparison of Measured Cross Sections to QED

6.5.1 Cross Section for $e^+e^- \to \gamma\gamma$

The number of $e^+e^- \to \gamma\gamma$ events passing the selection criteria for each data set is shown in Tables 6-2 [3] and 6-3.[4] The measured cross section is also shown for each data set (having corrected each for efficiency and radiative effects), along with their statistical and systematic errors. These systematic errors reflect the 0.7% uncertainty in the efficiency function only; there is also an overall systematic luminosity uncertainty of 2.4% for AMY 1.0 data and 1.8% for AMY 1.5 data. The last column in each table shows the integrated Born cross section for the corresponding energy.

The integrated cross section for $e^+e^- \to \gamma\gamma$ as a function of energy is shown for AMY 1.0 in Figure 6-4, and for AMY 1.5 in Figure 6-5. The Born cross section is also shown. Several data sets have been combined in the plot for AMY 1.0: the 59.05 GeV data (runs 6290-6332) have been combined with the 59 GeV data; the energy scan data (runs 6226-6286) have been combined with the 58.5 GeV data. In the plot for AMY 1.5, the 63.6 GeV data have been combined with the 64 GeV data.

The χ^2 value for Figure 6-4 is 16.9 for 12 *dof*. Half of this value is contributed by the 57 GeV datum. The χ^2 value for Figure 6-5 is 9.8 for 10 *dof*.

One of the advantages of the process $e^+e^- \to \gamma\gamma$ is that, to a very good approximation, the $\mathcal{O}(\alpha^3)$ cross section scales as s^{-1}. Some of the angle-dependent δ terms in Equation 1.21 exhibit a slightly different s-dependence, but the variation of these terms over the TRISTAN energy range is far smaller than the statistical uncertainty in the $e^+e^- \to \gamma\gamma$ measurement. The data samples can therefore be combined into one differential cross section measurement

[3] The numbers in parentheses in Table 6-2 represent the effective CM energy, integrated luminosity, etc. for the weighted sum of the spring, 1989 energy scan data.

[4] We have removed the suspect 170 nb^{-1} of data discussed in Section 6.4.2 from the first 58 GeV run period.

by correcting for s dependence and dividing by the total integrated luminosity. This is shown in Figure 6-6, together with the Born cross section integrated over each bin. Data at different energies are scaled by $s/(58\,\mathrm{GeV})^2$. The χ^2 value for Figure 6-6 is 15.1 for 14 dof.

Table 6-2: Measured $e^+e^- \rightarrow \gamma\gamma$ cross sections for AMY 1.0.

Run Period	$\sqrt{s}$	PTC $\int \mathcal{L}\, dt$	# SHC $\gamma\gamma$	σ_{meas} (pb)	σ_{Born} (pb)
2733 - 2987	50.00	0.636	22	$41.8 \pm 9.0 \pm 0.3$	55.01
3048 - 3568	52.00	3.976	164	$49.9 \pm 4.0 \pm 0.4$	50.86
3712 - 4416	55.00	3.266	130	$48.1 \pm 4.3 \pm 0.4$	45.47
4511 - 5170	56.00	5.993	234	$47.3 \pm 3.1 \pm 0.4$	43.85
5173 - 5361	56.50	0.994	29	$35.0 \pm 6.5 \pm 0.3$	43.09
5369 - 5692	57.00	4.398	198	$54.6 \pm 3.9 \pm 0.4$	42.33
5816 - 6121	60.00	2.465	92	$45.1 \pm 4.7 \pm 0.4$	38.20
6134 - 6223	58.50	0.801	27	$40.5 \pm 7.8 \pm 0.3$	40.19
6226 - 6286	(58.52)	(0.721)	(29)	$(48.9 \pm 9.1 \pm 0.4)$	(40.16)
6290 - 6332	59.05	0.505	19	$45.8 \pm 10.6 \pm 0.4$	39.45
6334 - 6410	60.00	0.757	23	$37.2 \pm 7.8 \pm 0.3$	38.20
6423 - 6674	60.80	1.376	49	$43.0 \pm 6.4 \pm 0.3$	37.20
6676 - 6697	59.00	0.178	5	$33.4 \pm 15.0 \pm 0.3$	39.51
6698 - 6703	60.80	0.0575	1	$20.3 \pm 20.3 \pm 0.2$	37.20
6705 - 6740	59.00	0.371	11	$35.0 \pm 10.6 \pm 0.3$	39.51
6744 - 6822	60.80	0.708	32	$54.7 \pm 9.8 \pm 0.4$	37.20
6906 - 6997	60.00	0.347	18	$64.6 \pm 15.4 \pm 0.5$	38.20
7006 - 7176	60.80	1.181	30	$30.8 \pm 5.7 \pm 0.2$	37.20
7192 - 7629	61.40	4.287	130	$36.7 \pm 3.3 \pm 0.3$	36.48
7662 - 7795	54.00	0.531	19	$43.6 \pm 10.1 \pm 0.3$	47.17

Table 6-3: Measured $e^+e^- \rightarrow \gamma\gamma$ cross sections for AMY 1.5.

Run Period	$\sqrt{s}$	ESC $\int \mathcal{L}\, dt$	# SHC $\gamma\gamma$	σ_{meas} (pb)	σ_{Born} (pb)
7889 - 8245	64.00	1.075	31	$33.9 \pm 6.1 \pm 0.3$	33.58
8246 - 8351	63.60	0.431	5	$13.7 \pm 6.1 \pm 0.1$	34.00
8353 - 8356	60.00	0.0161	1	$72.8 \pm 72.8 \pm 0.6$	38.20
8378 - 10896	58.00	26.56	790	$35.95 \pm 1.29 \pm 0.29$	40.88
10983 - 11805	58.00	8.10	261	$37.99 \pm 2.37 \pm 0.49$	40.88
11821 - 12639	58.00	25.73	829	$38.18 \pm 1.33 \pm 0.31$	40.88
12650 - 14579	58.00	62.92	2163	$40.71 \pm 0.88 \pm 0.41$	40.88
14594 - 15259	58.00	19.44	636	$38.65 \pm 1.54 \pm 0.31$	40.88
8378 - 15259	58.00	142.75	4679	$38.93 \pm 0.60 \pm 0.36$	40.88
15260 - 15292	59.70	0.97	26	$31.5 \pm 6.2 \pm 0.3$	38.59
15293 - 15330	58.20	1.38	49	$42.4 \pm 6.1 \pm 0.3$	40.60
15331 - 15373	59.20	1.36	45	$39.4 \pm 5.9 \pm 0.3$	39.24
15374 - 15412	58.45	1.31	50	$45.5 \pm 6.5 \pm 0.4$	40.25
15413 - 15458	58.70	1.32	54	$48.6 \pm 6.7 \pm 0.4$	39.91
15459 - 15519	58.95	1.72	61	$41.5 \pm 5.4 \pm 0.3$	39.58
15520 - 15562	59.45	1.20	45	$44.4 \pm 6.7 \pm 0.4$	38.92
15563 - 15630	57.60	2.03	69	$40.4 \pm 4.9 \pm 0.3$	41.46

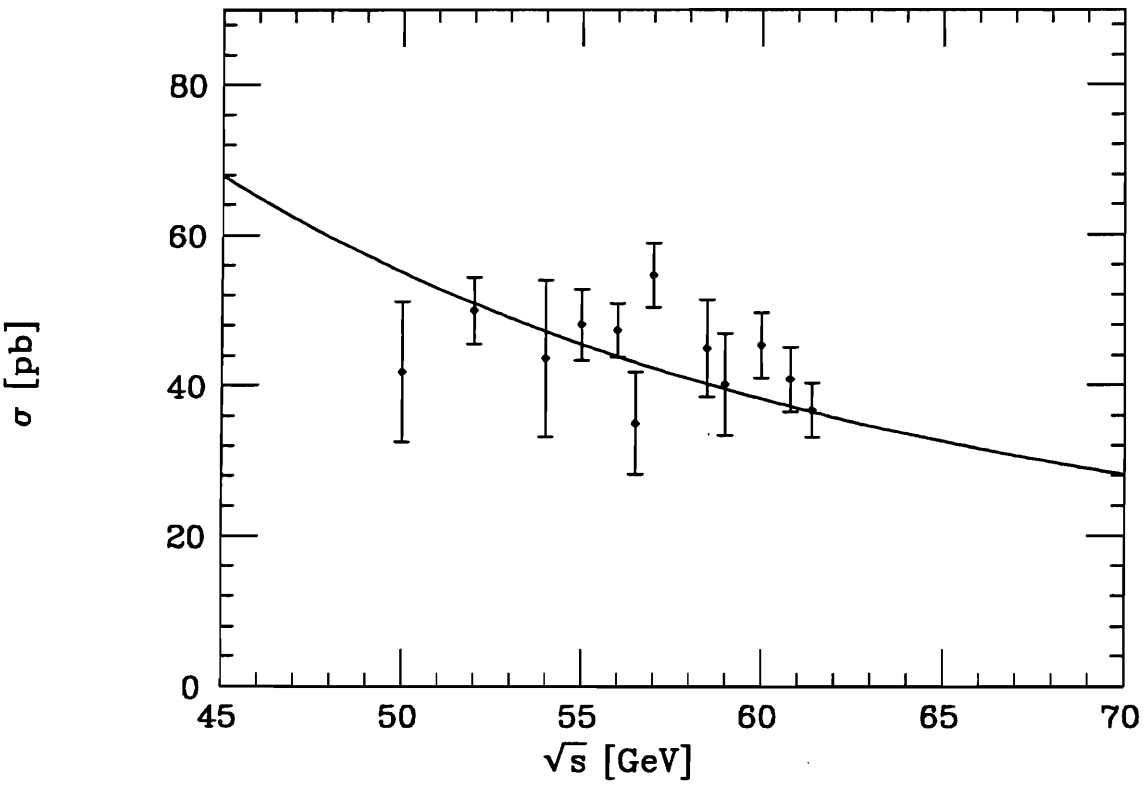

Figure 6-4: Integrated cross section vs. CM energy for AMY 1.0.

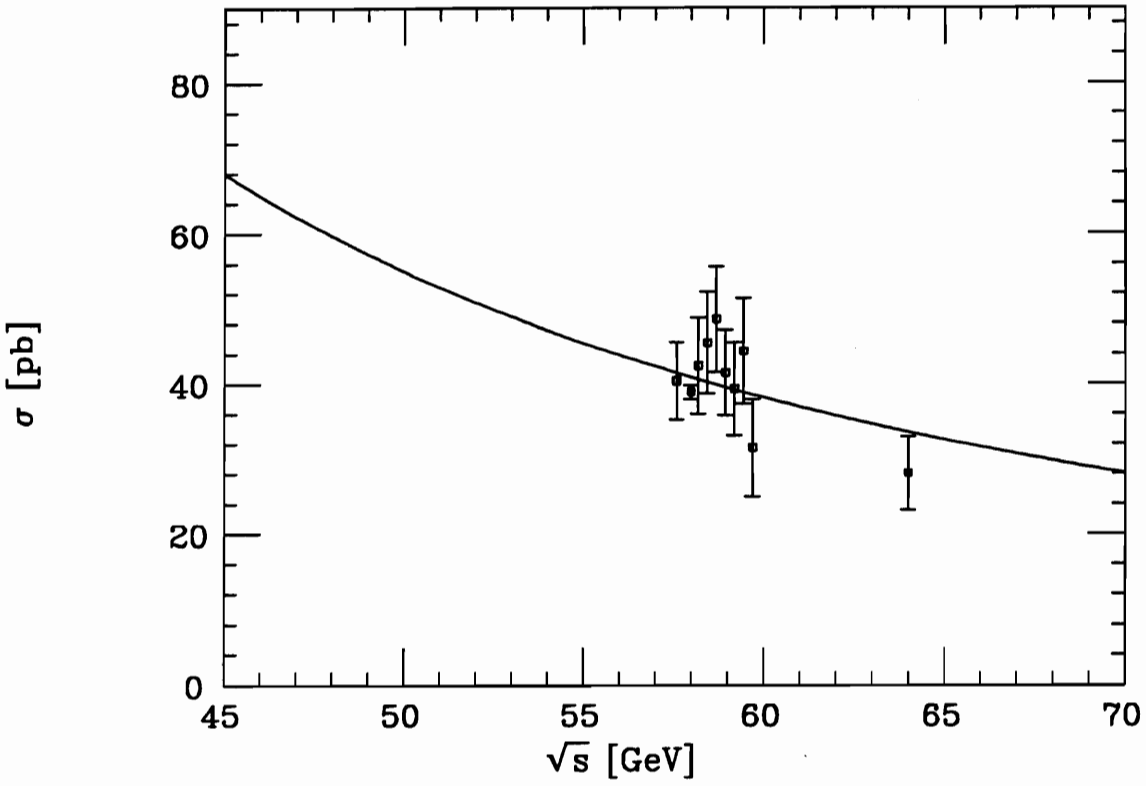

Figure 6-5: Integrated cross section vs. CM energy for AMY 1.5.

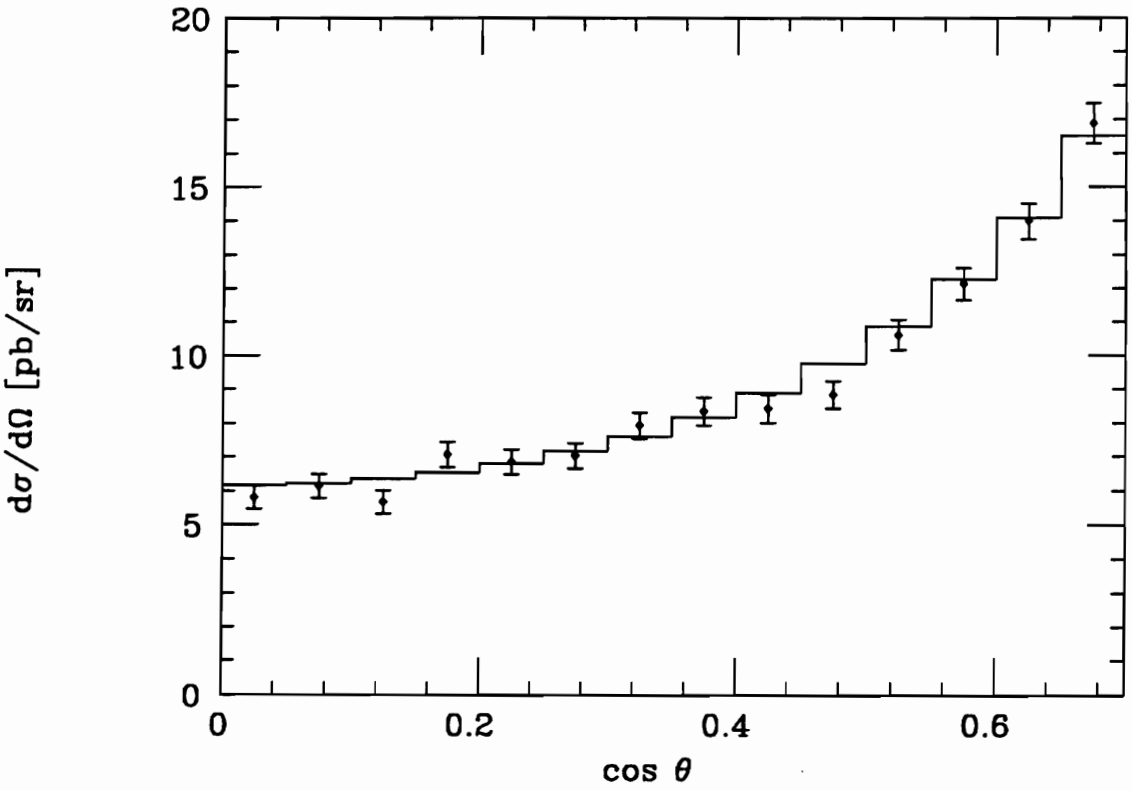

Figure 6-6: $d\sigma/d\Omega$ for all $e^+e^- \rightarrow \gamma\gamma$ data. Data at different energies are scaled by $s/(58\,\mathrm{GeV})^2$.

Chapter 7

Analysis of $e^+e^- \rightarrow \gamma\gamma\gamma$

The cross section for $e^+e^- \rightarrow \gamma\gamma\gamma$ is too complicated to present in one histogram. We can consider some of the variables individually, and then construct other useful kinematical variables to investigate how the cross section variables interrelate.

Combining data at various energies presents a problem for the $e^+e^- \rightarrow \gamma\gamma\gamma$ cross section. While it is clear that the total cross section will generally scale as s^{-1}, it is not immediately clear how the photon spectrum will change with s. We will therefore confine our discussion to a 123.31 pb^{-1} subsample of the 58 GeV data.[1]

A few comments are necessary regarding the efficiency function for $e^+e^- \rightarrow \gamma\gamma\gamma$. We are not (again, for reasons of complexity) going to attempt to correct the measured $\gamma\gamma\gamma$ distributions for direct comparison to the lowest order cross section, as we did with $e^+e^- \rightarrow \gamma\gamma$. Instead, we will compare the experimental results directly to the Monte Carlo results. We will not worry about triggering efficiencies *per se*, since any deviation from 100% will not be measurable at this statistical level. Efficiency losses due to vertex smearing will be compensated during $e^+e^- \rightarrow \gamma\gamma\gamma$ kinematical reconstruction.

[1] Only low acollinearity data are available from the Fall, 1992 sample at this time. They are therefore not included in this analysis.

7.1 Kinematical Reconstruction

Events with final states consisting of three photons have an additional property to aid in analysis. Because there are three[2] constraint equations, we can determine the photon energies (our three unknowns) by relying solely on the angular positions of the photons. Because the angular resolution of the SHC is better than its energy resolution, the energy spectrum can be substantially improved.

The main difficulty is that the measured photon momenta do not generally lie exactly in the same plane, due primarily to longitudinal vertex smearing (with some contributions from angular smearing and additional photon radiation along the beam axis). However, we do know that the primary interaction occurred very close to the z-axis. We can thus compensate for vertex smearing by choosing a new vertex point along the z-axis such that the photon directions relative to the new vertex lie in the same plane. Once we have established the new vertex and photon directions, we can solve the energy and momentum conservation equations to get the refitted photon energies.

First, we must choose a new interaction point. If we imagine the three measured photon momentum vectors pointing away from the center of the detector, we can construct a plane from the points where those vectors intersect the average region of shower maximum (a cylindrical radius of approximately 90 cm). The point where this plane intersects the z-axis is our new interaction point. The distribution of the reconstructed interaction points is shown in Figure 7-1, shown along with a best-fit Gaussian ($\sigma = 1.06 \pm 0.08$). This is agrees well with what we would expect from z vertex smearing, except for a few large values (which are probably due to additional photon radiation).

Once the final state plane has been assigned, new photon momentum directions are drawn from the reconstructed interaction point to each of the photon "hit" points used to construct

[2]In the case of three photons in the final state, we noted in Section 1.1.5 that the momentum vectors are constrained to lie in a plane. We can reduce the number of momentum conservation equations to two by assigning two new coordinates that span the plane.

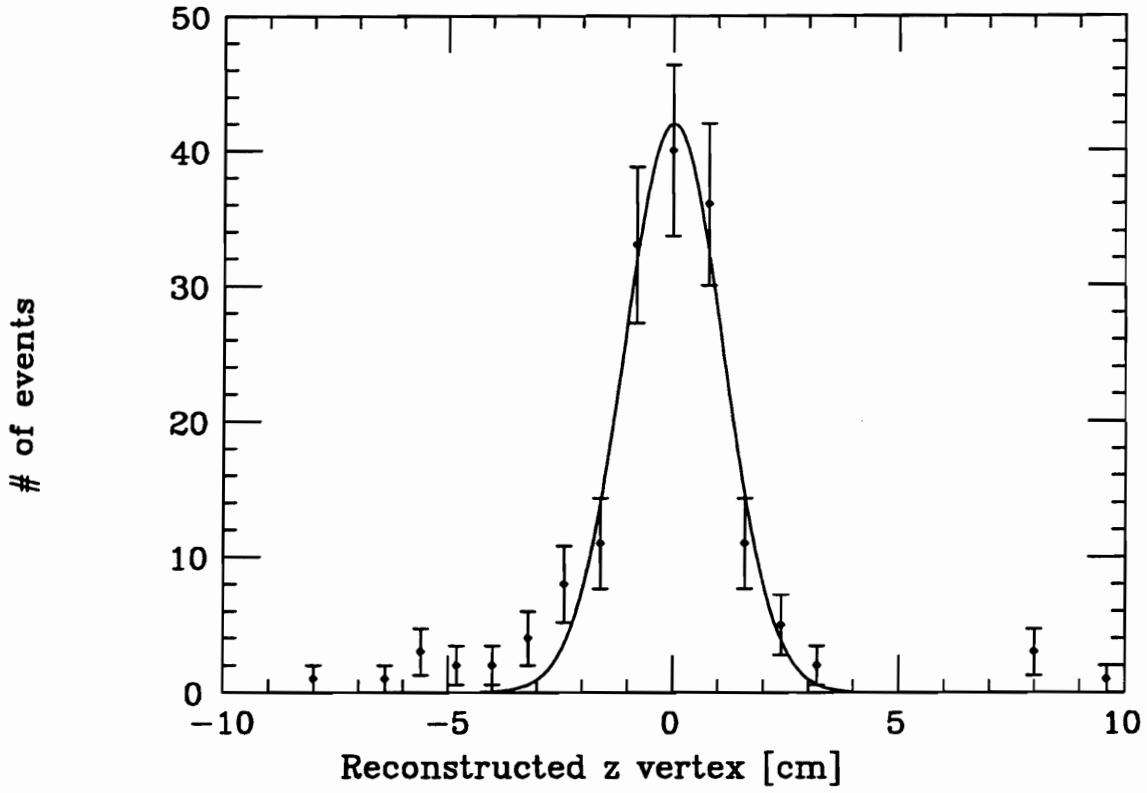

Figure 7-1: Reconstructed vertex distribution for $e^+e^- \to \gamma\gamma\gamma$.

the plane. In other words, the original photon directions are projected along the z-axis onto the plane. Photon opening angles ψ_1, ψ_2, and ψ_3 are recalculated as in Figure 1-7.

The final stage of reconstruction is a simple minimization. Two of the photon opening angles (ψ_2 and ψ_3) are varied. At each step, photon energies are recalculated by 4-momentum conservation, and a χ^2 function is calculated:

$$\chi^2 = \left(\frac{\psi_2 - \psi_2'}{\sigma(\psi)}\right)^2 + \left(\frac{\psi_3 - \psi_3'}{\sigma(\psi)}\right)^2 + \left(\frac{E_1 - E_1'}{\sigma(E_1)}\right)^2 + \left(\frac{E_2 - E_2'}{\sigma(E_2)}\right)^2 + \left(\frac{E_3 - E_3'}{\sigma(E_3)}\right)^2, \quad (7.1)$$

where ψ_i is the i^{th} original opening angle in the plane, ψ_i' is the new opening angle, E_i is the measured energy of the i^{th} photon, E_i' is its fitted energy, $\sigma(\psi) = \sqrt{\sigma^2(\theta) + \sigma^2(\phi)} = 0.316°$, and $\sigma(E_i) = 0.23\sqrt{E_i} + 0.06E_i$. This χ^2 is minimized, and the corresponding energies and opening angles are taken as the reconstructed values.

7.2 Results

There were 101 events in the surviving $e^+e^- \to \gamma\gamma\gamma$ sample from the 123.31 pb^{-1} data set. This gives us a total integrated cross section of

$$\sigma_{\gamma\gamma\gamma}^{\text{expt}} = (0.82 \pm 0.08 \pm 0.01)\,\text{pb}, \quad (7.2)$$

where the first error is statistical and the second error is the systematic error due to the luminosity measurement. The MC $e^+e^- \to \gamma\gamma\gamma$ sample contained 1381 events with an integrated luminosity of 1.82 fb^{-1}; thus the ratio of the observed to the predicted size of the integrated cross section is:

$$\frac{\sigma_{\gamma\gamma\gamma}^{\text{expt}}}{\sigma_{\gamma\gamma\gamma}^{\text{MC}}} = 1.08 \pm 0.11 \pm 0.04, \quad (7.3)$$

where the MC statistical error has been combined in quadrature with the luminosity error to produce the systematic error.

Figure 7-2 shows the refitted energy spectrum for photons in the 58 GeV $e^+e^- \rightarrow \gamma\gamma\gamma$ sample. Each photon in a refitted event was required to be within $45° \leq \theta \leq 135°$, and to have a refitted energy of at least $E_{\rm beam}/20$. Experimental data are shown with statistical errors; the histogram is from the Monte Carlo sample. The distribution has a χ^2 of 14.6 for 15 *dof*.

Figure 7-3 shows the distribution of opening angles for all photon pairs in the experimental and Monte Carlo $e^+e^- \rightarrow \gamma\gamma\gamma$ samples. The distribution has a χ^2 of 28.1 for 15 *dof*.

The distributions for two kinematical variables have been produced to examine the interrelationships between the photon energies and angles. Figure 7-4 shows the pairwise invariant mass distributions for the experimental and Monte Carlo samples (3 entries per event). Figure 7-5 shows the distributions of momentum transfer squared, given by

$$q^2 = \sqrt{s}E_\gamma(1 - \cos\theta_\gamma), \tag{7.4}$$

for all photons in the experimental and Monte Carlo samples. The χ^2 values for the distributions are 14.0/12 *dof* and 10.0/15 *dof*, respectively.

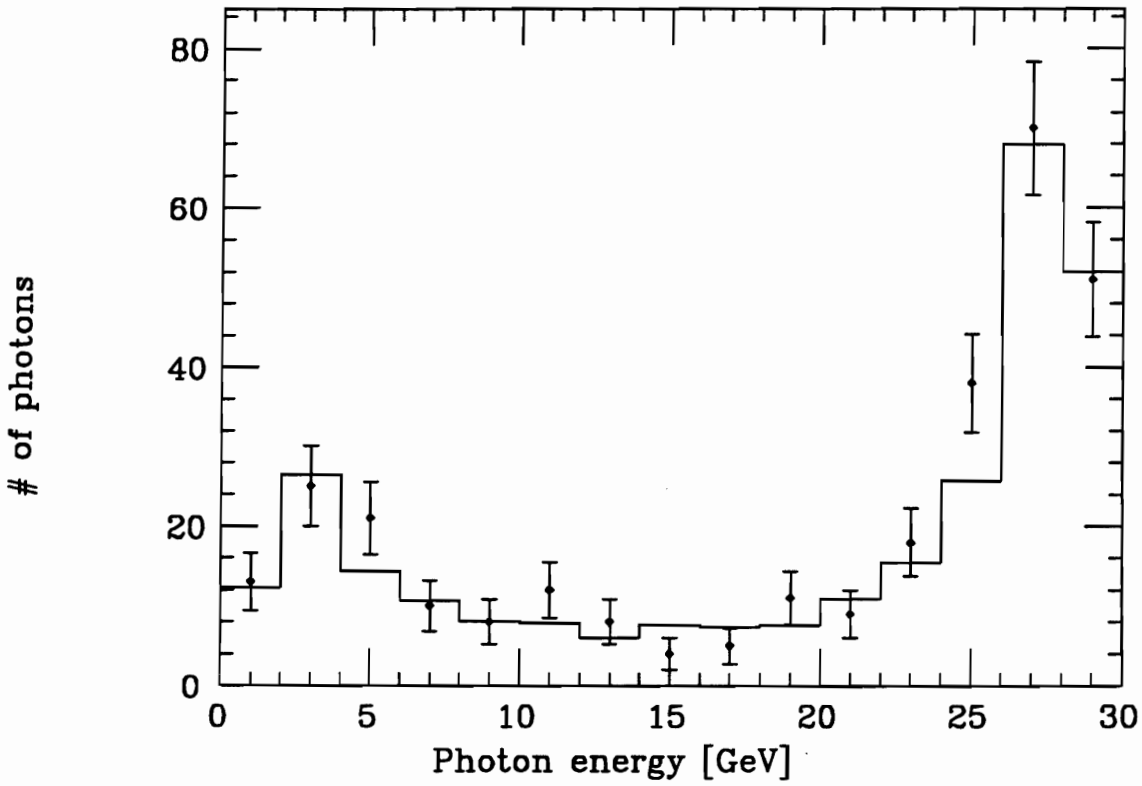

Figure 7-2: Data and Monte Carlo photon energies from $e^+e^- \to \gamma\gamma\gamma$.

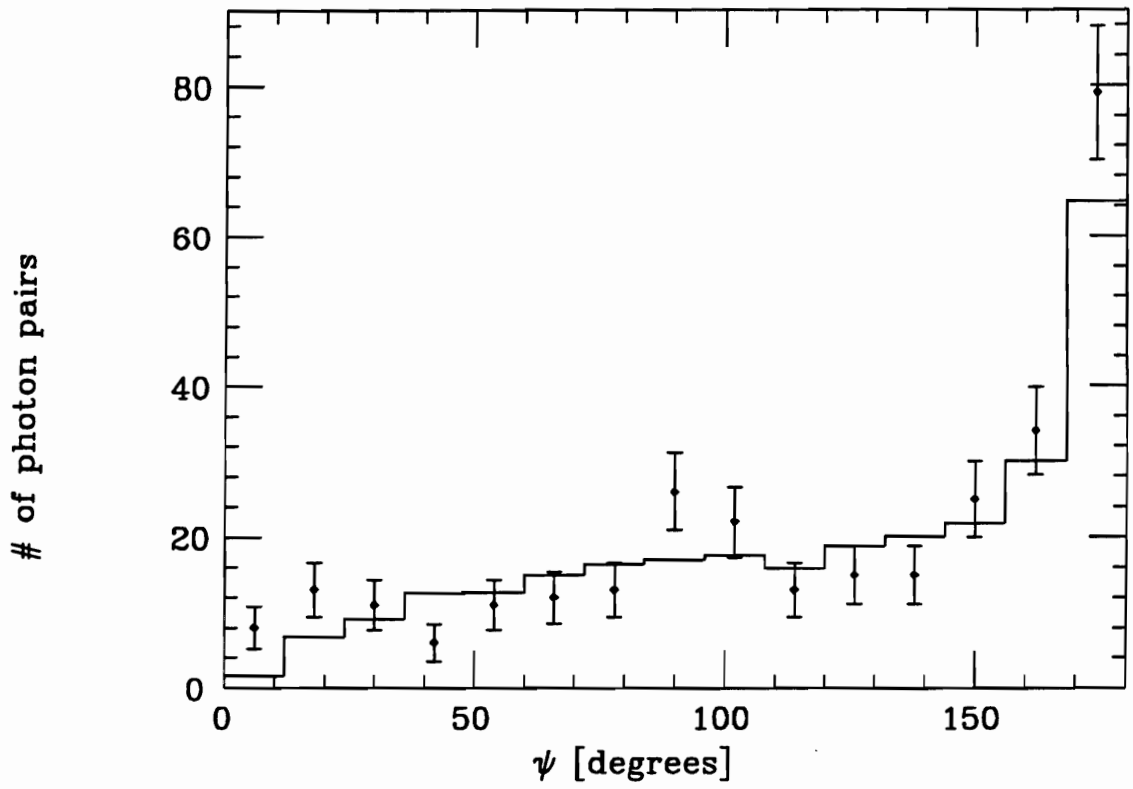

Figure 7-3: Photon opening angles for $e^+e^- \rightarrow \gamma\gamma\gamma$.

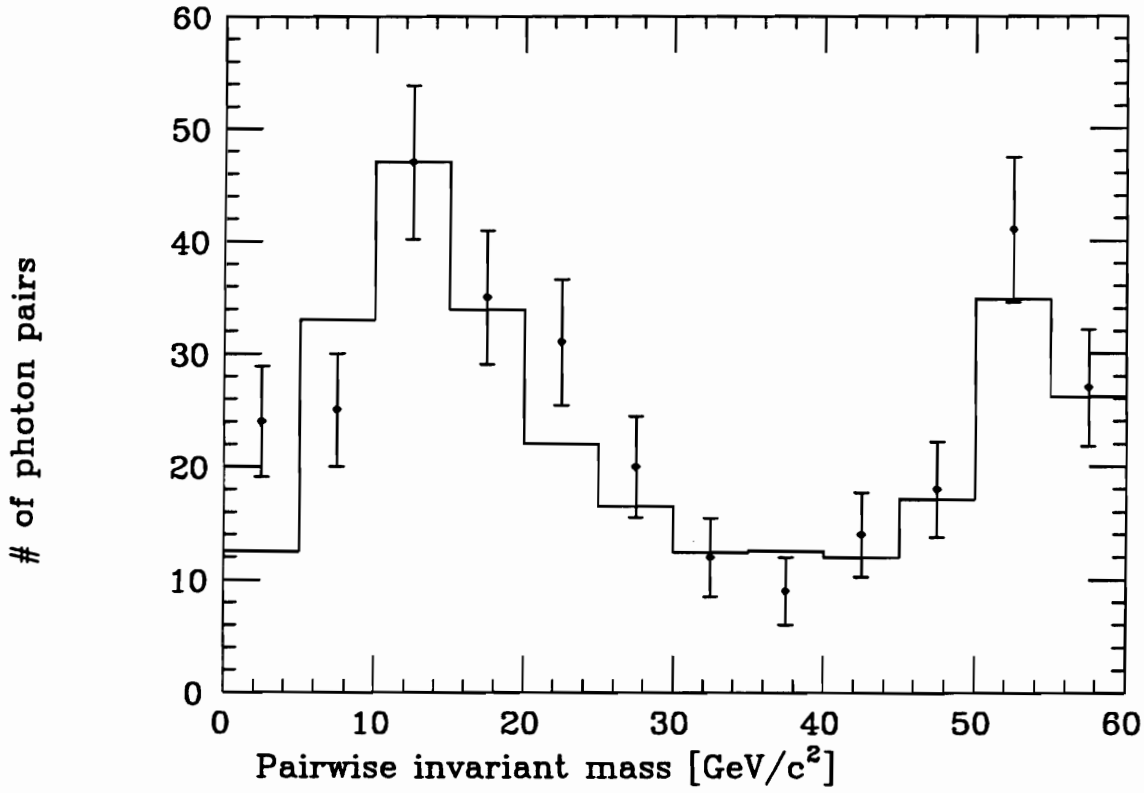

Figure 7-4: Pairwise invariant mass distribution for $e^+e^- \rightarrow \gamma\gamma\gamma$.

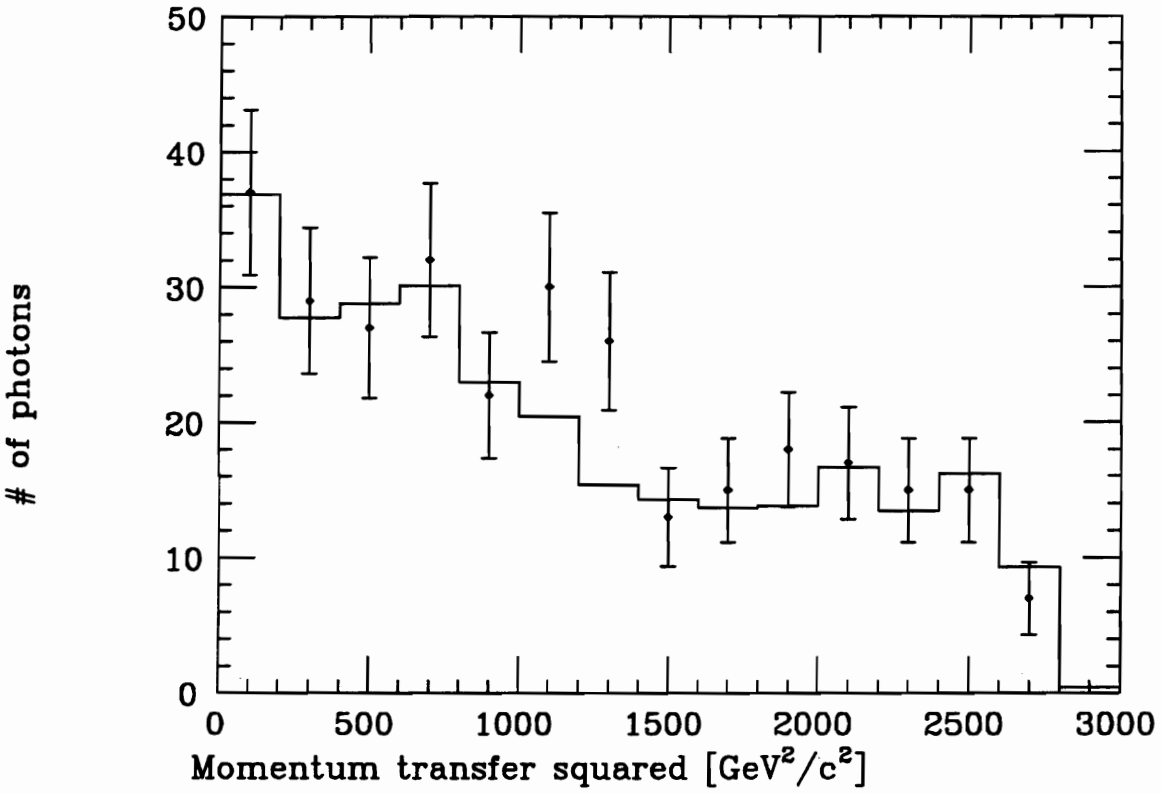

Figure 7-5: Momentum transfer squared for $e^+e^- \rightarrow \gamma\gamma\gamma$ photons.

Chapter 8

Comparison to Contact Models

In order to compare the measured $e^+e^- \to \gamma\gamma$ data samples to the several $e^+e^-\gamma\gamma$ contact interaction models presented in Section 1.3, we first divide the folded $\cos\theta$ distributions by the Born cross section. These are shown for four AMY 1.0 data samples (52, 55, 56, and 57 GeV) in Figure 8-1, and for the AMY 1.5 58 GeV data sample in Figure 8-2.

For each contact model, these data are compared to the expression

$$g(s,\Lambda) \;=\; 1 \;+\; \left(\frac{d\sigma}{d\Omega}\right)^{\text{contact}}_{\gamma\gamma} \Big/ \left(\frac{d\sigma}{d\Omega}\right)^{\text{Born}}_{\gamma\gamma}\,, \tag{8.1}$$

where the second term is given by one of the following expressions:

$$\left(\frac{d\sigma}{d\Omega}\right)^{\text{L,R}} \Big/ \left(\frac{d\sigma}{d\Omega}\right)^{\text{Born}} \;=\; \pm\frac{s^2}{4\Lambda_\pm^4}\left(1-\cos^2\theta\right) \;+\; \frac{s^4}{32\Lambda_\pm^8}\left(1-\cos^2\theta\right)^2 \tag{8.2}$$

$$\left(\frac{d\sigma}{d\Omega}\right)^{\text{L+R}} \Big/ \left(\frac{d\sigma}{d\Omega}\right)^{\text{Born}} \;=\; \pm\frac{s^2}{2\Lambda_\pm^4}\left(1-\cos^2\theta\right) \;+\; \frac{s^4}{16\Lambda_\pm^8}\left(1-\cos^2\theta\right)^2 \tag{8.3}$$

$$\left(\frac{d\sigma}{d\Omega}\right)^{\text{L-R}} \Big/ \left(\frac{d\sigma}{d\Omega}\right)^{\text{Born}} \;=\; \frac{s^4}{16\Lambda_\pm^8}\left(1-\cos^2\theta\right)^2 \tag{8.4}$$

$$\left(\frac{d\sigma}{d\Omega}\right)^{\text{cutoff}} \Big/ \left(\frac{d\sigma}{d\Omega}\right)^{\text{Born}} \;=\; \pm\frac{s^2}{2\Lambda_\pm^4}\left(1-\cos^2\theta\right). \tag{8.5}$$

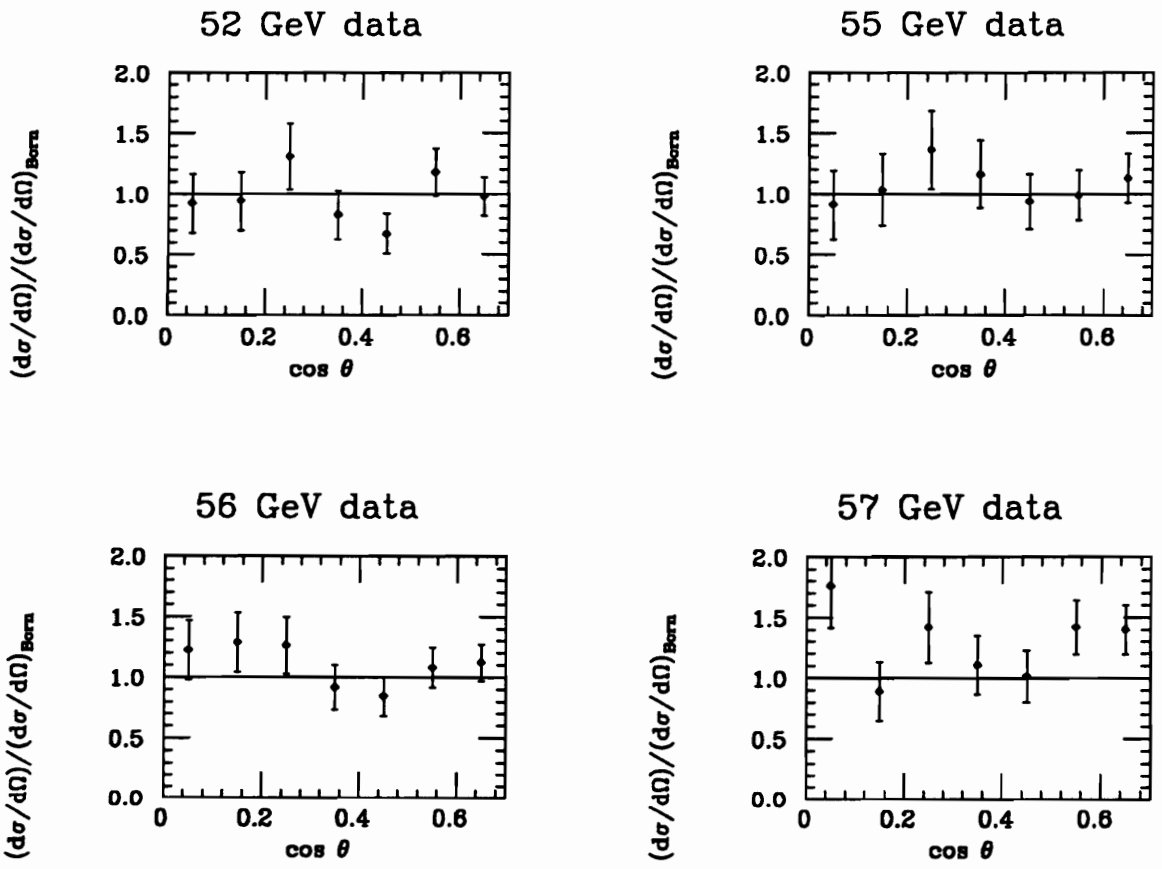

Figure 8-1: Measured cross section as a fraction of the Born cross section for four AMY 1.0 data sets.

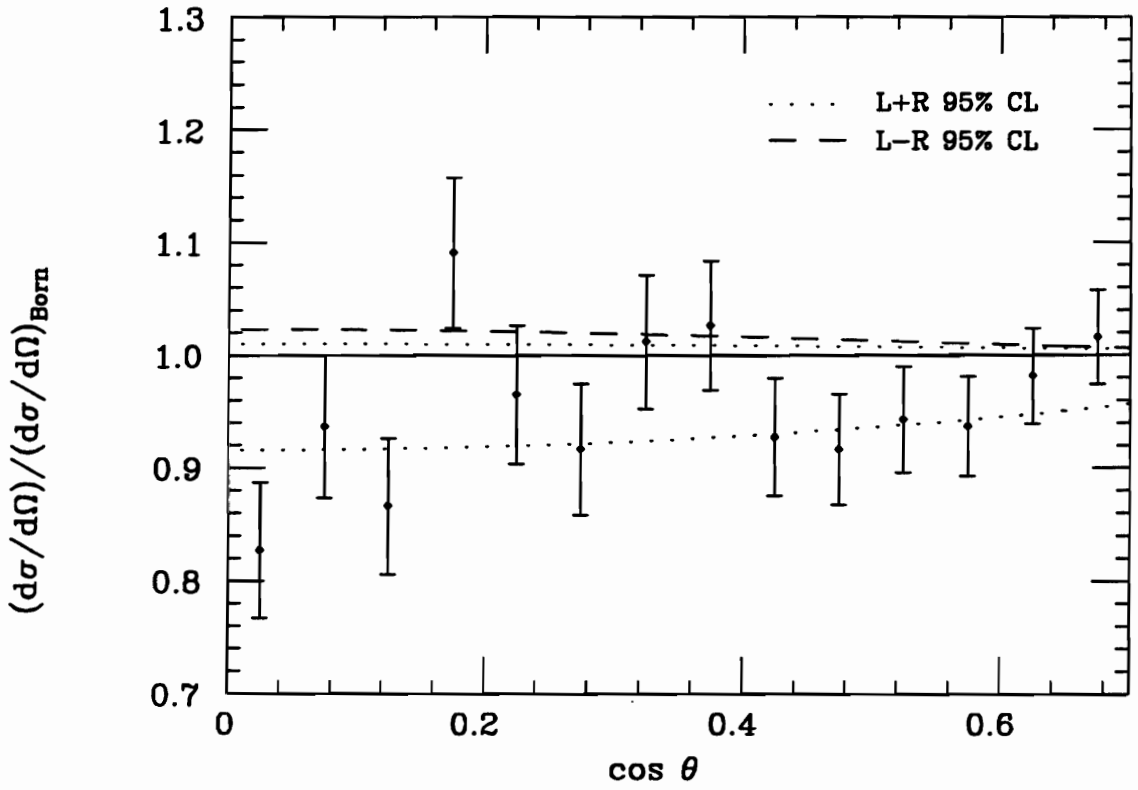

Figure 8-2: Measured cross section as a fraction of the Born cross section for the AMY 1.5 58 GeV data. Also shown are the 95% C.L. limits from the $L+R$ and $L-R$ contact models.

8.1 Fit to the Contact Models

To determine the goodness-of-fit for each contact model, we integrate the expression $g(s,\Lambda)$ over each angular bin, and compute a χ^2 value with respect to the experimental data points. Each value of Λ_+ and Λ_- will have a unique value for χ^2 for each model. This is complicated by the fact that each data set has an associated normalization parameter, reflecting the statistical uncertainties in their luminosity measurements. There is also an overall normalization parameter associated with the Monte Carlo, and a normalization parameter shared by the four AMY 1.0 data sets, representing the systematic uncertainty in the PTC luminosity determination.[1] These normalization parameters are allowed to float, but as they deviate from unity they also contribute to the χ^2.

The χ^2 function for the i^{th} data set is given by

$$\chi^2_i = \sum_{j=1}^{M_i} \left[\frac{f^i_j(\Lambda) - N_{\text{MC}} N_{\text{syst}} N^i y^i_j}{N_{\text{MC}} N_{\text{syst}} N^i \sigma^i_j} \right]^2 + \left[\frac{N^i - 1}{\sigma_{N^i}} \right]^2 , \tag{8.6}$$

where j denotes the bin number in $\cos\theta$; $f^i_j(\Lambda)$ is the integral of $g(s_i,\Lambda)$ over bin j; y^i_j is the measured cross section in that bin (expressed as a fraction of the Born cross section); σ^i_j is the statistical error on y^i_j; N^i and σ_{N^i} are the normalization parameter for the i^{th} data set and its statistical error, respectively; N_{MC} is the normalization parameter associated with the Monte Carlo; and N_{syst} is the normalization parameter associated with the PTC systematic uncertainty (this parameter is set equal to 1 for the 58 GeV data set).

The overall χ^2 function is thus given by

$$\chi^2 = \sum_{i=1}^{5} \chi^2_i + \left(\frac{N_{\text{MC}} - 1}{\sigma_{N_{\text{MC}}}} \right)^2 + \left(\frac{N_{\text{syst}} - 1}{\sigma_{N_{\text{syst}}}} \right)^2 , \tag{8.7}$$

[1] The 1.8% systematic uncertainty in the ESC luminosity measurement is combined with the statistical uncertainty of the 58 GeV data set, to avoid a numerically unstable degeneracy.

where $\sigma_{N_{MC}}$ and $\sigma_{N_{syst}}$ denote the errors in the MC normalization and the PTC normalization, which are 0.8% and 2.4%, respectively. The "unique" value of χ^2 assigned to a given value of Λ_+ or Λ_- for a given model is the *lowest possible* value of χ^2, which we determine in each case by minimization over the 7-dimensional normalization parameter space. This minimization is performed by the Nelder-Mead downhill simplex algorithm [82].

8.2 Assignment of Scale Parameter Limits

In order to determine 95% C.L. limits on the scale parameters $\Lambda_\pm$, we must first choose an appropriate parameter for fitting. It has been shown [83], [84] that Λ is not an appropriate fitting parameter; the errors on Λ do not have a Gaussian distribution, making it difficult to combine limits from different experiments.

We therefore define a parameter ϵ, such that

$$\epsilon = \pm(\Lambda_\pm)^{-4}, \tag{8.8}$$

where a negative value of ϵ corresponds to the Λ_- case, etc. In the case of the $L-R$ model, we use $\epsilon = (1/\Lambda)^8$ (we do not consider the case of $\epsilon < 0$ in the $L-R$ model, since the interaction carries the same overall sign for Λ_+ and Λ_-). The parameter ϵ can be considered as a measure of the deviation from QED.

The ϵ value with the minimum χ^2 is taken to be the best fit value $\epsilon_{\min}$. The 95% C.L. limits are placed at the values of ϵ where the χ^2 has increased by 2.706 from the minimum. These values correspond to $\epsilon \mapsto \epsilon_{\min} + 1.645\sigma^+$ in the case of Λ_+ models, and $\epsilon \mapsto \epsilon_{\min} - 1.645\sigma^-$ in the case of Λ_- models.

Plots of χ^2 as a function of ϵ are shown in Figures 8-3 and 8-4, together with the 95% C.L. limits on ϵ. The interpretation of the $\epsilon_{\min} + 1.645\sigma^\pm$ points as the 95% C.L. lower limits for

$\Lambda_\pm$ runs into difficulty with the $L-R$ model, where the supposed χ^2 minimum $\epsilon_{\rm min}$ falls into the unphysical region $\epsilon < 0$. In this case we can conservatively set an upper limit for Λ_+ by finding the point $\epsilon' > 0$ such that $\chi^2(\epsilon') = \chi^2(\epsilon = 0) + 2.706$.

Plots of χ^2 as a function of ϵ are shown in Figures 8-3 and 8-4, together with the 95% C.L. limits on ϵ. These results are also tabulated in Tables 8-1 and 8-2. The best fit normalization values for the various models are shown in Table 8-3.

8.3 Discussion and Comparison to Previous Limits

In all cases except the $L-R$ model, Λ_- models are favored. This is governed by the statistically dominant 58 GeV data set of AMY 1.5, which in Table 6-3 shows a systematic offset of around 4% (about 2σ away from the stated normalization error). Any contact model with a negative interference term will produce a better fit than QED over some range of compositeness scales.

The only published limits on $ee\gamma\gamma$ contact interactions using the most current techniques are from VENUS [72], TOPAZ [74], and ALEPH [85]. These are presented in comparison with the AMY limits in Table 8-4. The AMY lower limits for Λ_+, although generally larger than the limits from the other collaborations, may be somewhat inflated by the low measured cross section of the 58 GeV data set.

8.4 Limits on Excited Electron Mass

Using Equation 1.40, we can use the 95% C.L. on $\Lambda_+^{\rm L}$, for example, to set a lower limit on the allowed compositeness scale as a function of excited electron mass $m_{e_L^*}$. This result is presented in Figure 8-5.

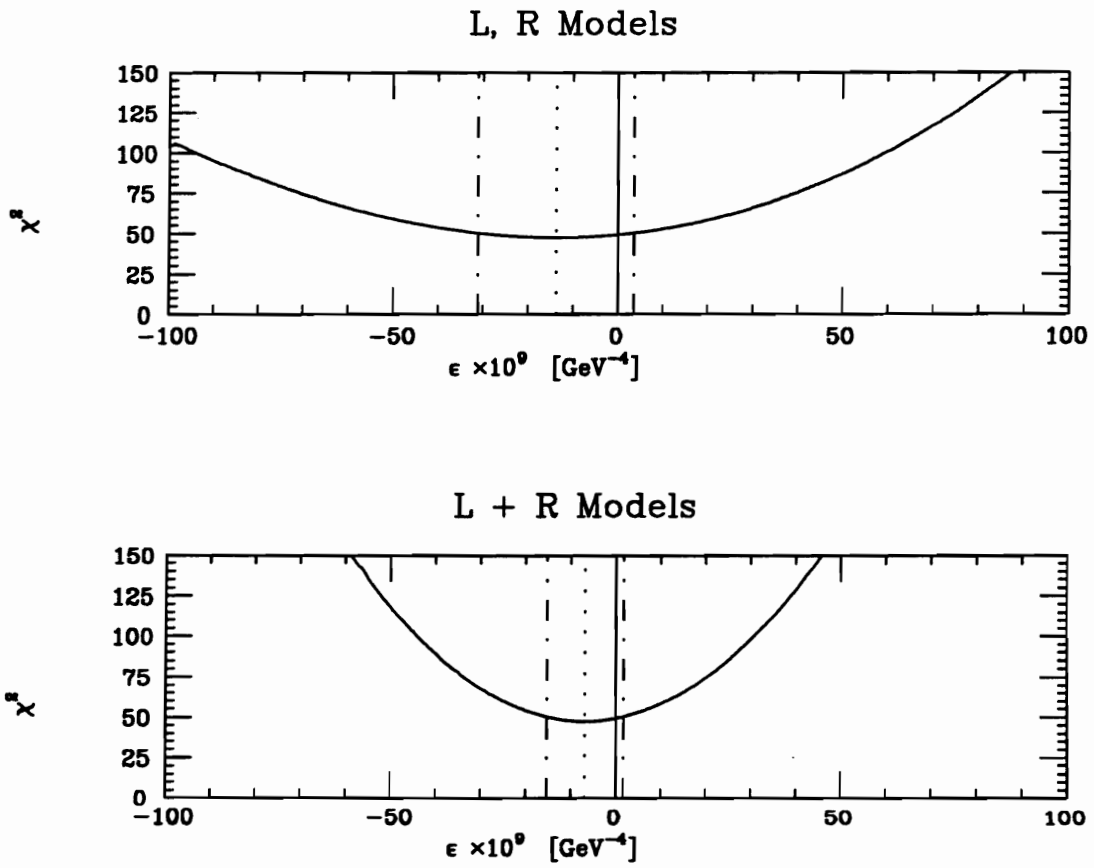

Figure 8-3: Plot of χ^2 vs. ϵ for L, R and $L + R$ contact models. Dotted lines indicate the χ^2 minimum ϵ_{min}; dash-dotted lines indicate 95% C.L. limits for $\Lambda_{\pm}$.

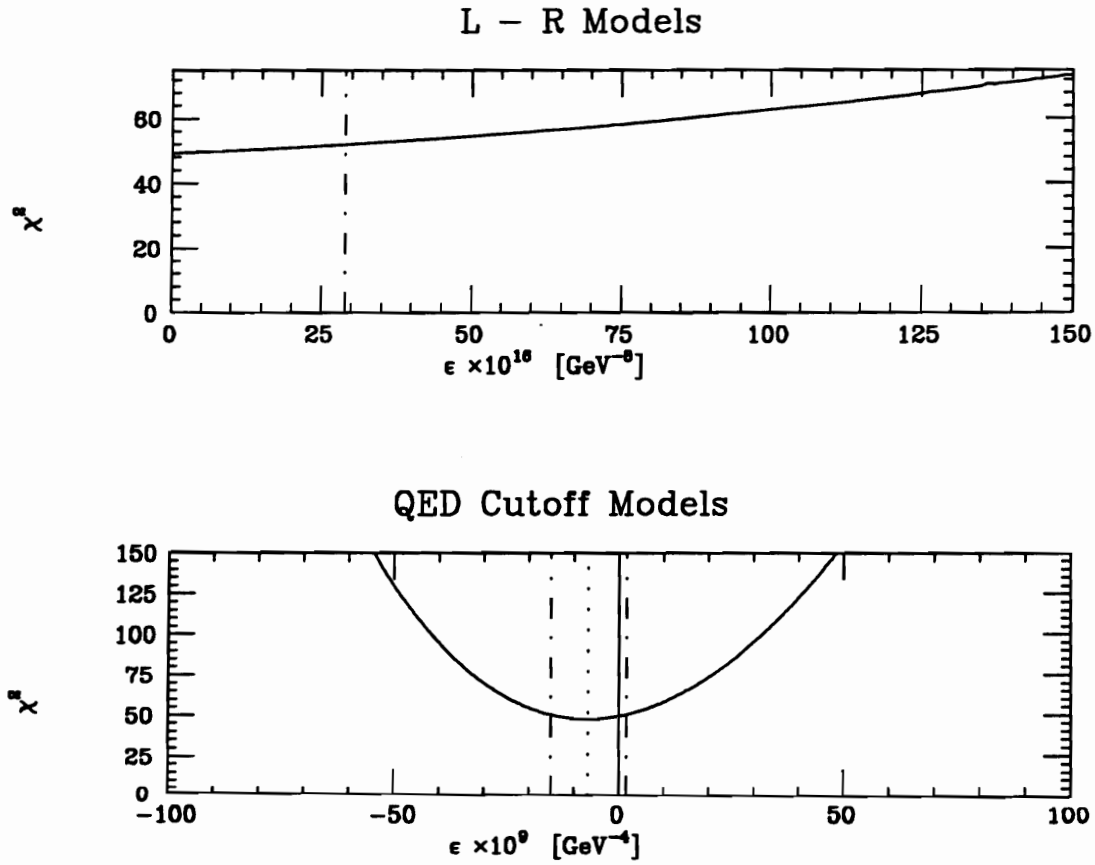

Figure 8-4: Plot of χ^2 vs. ϵ for $L-R$ and QED cutoff contact models. Dotted lines indicate the χ^2 minimum $\epsilon_{\min}$; dash-dotted lines indicate 95% C.L. limits for $\Lambda_{\pm}$.

Table 8-1: Fit Parameters for Electron-Photon Contact Models. All units are in GeV^{-4} (GeV^{-8} for $L - R$ case).

Model	ϵ_{min}	σ^+	σ^-	ϵ'
L, R	-1.37×10^{-8}	1.05×10^{-8}	1.06×10^{-8}	N.A.
$L + R$	-0.68×10^{-8}	0.52×10^{-8}	0.52×10^{-8}	N.A.
$L - R$	N.A.	N.A.	N.A.	2.89×10^{-15}
QED cutoff	-0.68×10^{-8}	0.52×10^{-8}	0.50×10^{-8}	N.A.

Table 8-2: Best Fits and 95% C.L. Limits for Electron-Photon Contact Models. All units are in GeV.

Model	Best Fit	Λ_-	Λ_+
L, R	$\Lambda_- = 92$	75	130
$L + R$	$\Lambda_- = 110$	90	156
$L - R$	QED	66	66
QED cutoff	$\Lambda_- = 110$	90	156

Table 8-3: Best fit normalization values for contact models.

Parameter	σ_N	$N(QED)$	$N(\epsilon_{\min}; L, R)$	$N(\epsilon_{\min}; L+R)$
N^{52}	0.020	1.0049	1.0043	1.0040
N^{55}	0.012	0.9991	0.9990	0.9993
N^{56}	0.009	0.9992	0.9989	0.9988
N^{57}	0.010	0.9969	0.9972	0.9970
N^{58}	0.021	1.0287	1.0101	1.0104
$N^{AMY\,1.0}$	0.024	0.9824	0.9771	0.9769
N^{MC}	0.008	1.0022	0.9990	0.9988

Table 8-4: 95% C.L. lower limits on Λ_+ and Λ_- from AMY, VENUS, TOPAZ and ALEPH.

Model	AMY		VENUS		TOPAZ		ALEPH	
	Λ_+	Λ_-	Λ_+	Λ_-	Λ_+	Λ_-	Λ_+	Λ_-
L, R	130	75	68	69	141	81	102	109
$L+R$	156	90	81	82	168	97	121	130
$L-R$	66	66	52	52	68	68	79	79
QED cutoff	156	90	81	82	168	97	120	129

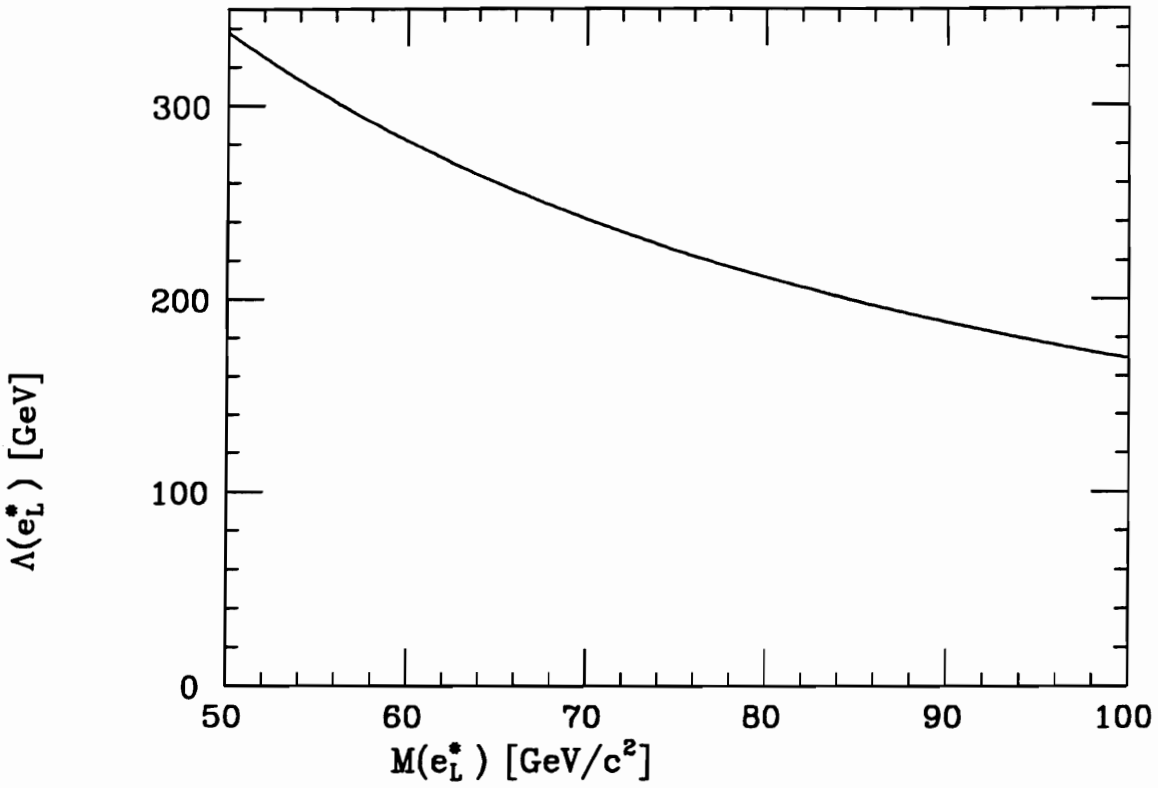

Figure 8-5: 95% C.L. limit for compositeness scale as a function of excited electron mass. Area below the curve is excluded.

Chapter 9

Search for Unstable Photinos

The detection and measurement of the hypothetical pair production of unstable photinos differs from the measurements we have previously discussed. Whereas the other processes show a strong signal above a small background, this process would, if observed, likely show a small signal against a moderate background. As it would be somewhat surprising to observe a clear signal from this process, the limit of our sensitivity (in the case of a null result) would be the most relevant quantity to measure. We would then use this result to set limits on the allowed masses of the photino and the scalar electron.

We recall that the final state contains two photons and two unobservable goldstino particles. If we observe two photons in the SHC, and discover that there is missing momentum and energy (which in turn requires that there be no other substantial SHC or endcap tags), we know that one of two things is true: either the missing particle(s) have escaped down the beam pipe, or the missing particle(s) have passed through some detector element without interacting. In the first case, the kinematics are severely constrained (especially for AMY 1.5, with its 3.0° veto angle). In the second case, either the missing particles are neutrinos (for which the cross section is extremely small), or we are observing a new physical process.

First, we will discuss the kinematical properties of the $\tilde{\gamma}\tilde{\gamma}$ production and decay processes.

Second, we will establish some kinematical cuts to distinguish unstable photino events from the two main backgrounds: $e^+e^- \rightarrow (\gamma)\gamma\gamma$ (where one of the photons is unobserved), and $e^+e^- \rightarrow (e^+e^-)\gamma\gamma$ (where the final state electrons are unobserved). Finally, we will apply these cuts to the data and to the unstable photino Monte Carlo, in an attempt to discover new physics. Failing such serendipity, we will use the Monte Carlo to establish what ranges of photino and selectron masses would be accessible to this experiment, and thereby rule out the existence of unstable photinos at that level.[1]

We will conduct our search for unstable photinos using all data taken before Fall, 1992 (only high-energy collinear data are currently available from this run period). The data sample comprises 156.86 pb^{-1} of integrated luminosity at energies from 50 to 64 GeV.

9.1 Some Observations on Kinematics

The photon energies and topology of the final state depend most crucially upon the photino mass. Let us consider two extreme cases: the very heavy and the very light photino.

In the case of the heavy photino, the photino is nearly at rest in the laboratory frame. Each daughter photon is emitted in a uniformly random direction (regardless of the specific differential cross section for $\tilde{\gamma}\tilde{\gamma}$ production), and each has an energy of $E_{\text{beam}}/2$. Because the ϕ directions are uniformly random and uncorrelated, there is typically a very high acoplanarity.[2] A scatter plot of acoplanarity vs. photino mass is shown in Figure 9-1.

In the case of the light photino, the particle decays in a highly boosted frame. Daughter photons tend to travel along the original direction of the photino (due to the "lighthouse" effect); therefore, the acollinearity tends to be low. Photon energies have a much broader distribution than in the case of the heavy photino. This is shown in Figure 9-2.

[1] Factors representing detection efficiency and acceptance factors are included in the PHASER Monte Carlo; details can be found in Section 3.2.

[2] The reader is reminded that acoplanarity is defined as $\xi = |180^\circ - |\phi_1 - \phi_2||$.

Because the kinematics of photino decay change so dramatically with photino mass, it shows that no one set of cuts will be ideal for all photino masses. A requirement of high acoplanarity, for example, can eliminate almost all of the $e^+e^- \rightarrow (\gamma)\gamma\gamma$ background to heavy photino decay while leaving the signal nearly intact. Such a cut would, however, destroy any signal from the decay of a light photino, which is better distinguished from the $e^+e^- \rightarrow \gamma\gamma$ background with a set of photon energy cuts.

We must not forget that the SHC was designed to optimize angular resolution, rather than energy resolution. The best strategy, then, is to make a loose acoplanarity cut for the heavy photino case, and a tight energy cut for the light photino case.

9.2 Low Mass $\tilde{\gamma}$ Search

9.2.1 Selection Criteria

The only substantial background to light photino decay is $e^+e^- \rightarrow \gamma\gamma$, where the photon energies have been mismeasured. A scatter plot of photon energies from $e^+e^- \rightarrow \gamma\gamma$ Monte Carlo is shown in Figure 9-3; the distribution of photon energies from $e^+e^- \rightarrow \tilde{\gamma}\tilde{\gamma} \rightarrow \tilde{G}\tilde{G}\gamma\gamma$ with $M_{\tilde{\gamma}} = 0.5\,\mathrm{GeV}$ is shown in Figure 9-4. In order to stay well away from the edges of the $e^+e^- \rightarrow \gamma\gamma$ background, we require each photon in our sample of real data to be below a cut of $E_{\mathrm{beam}}/2$.

We also require an acoplanarity cut of $\xi < 3°$ (in order to separate this sample from the heavy photino case), and an acollinearity cut of $\zeta \leq 10°$, to eliminate any background from $e^+e^- \rightarrow (\gamma)\gamma\gamma$.

9.2.2 Results of the Search

Nine low-mass photino candidate events were found. Of these, one was caused by unusually late photon conversions. Although no false candidates of this type were expected,

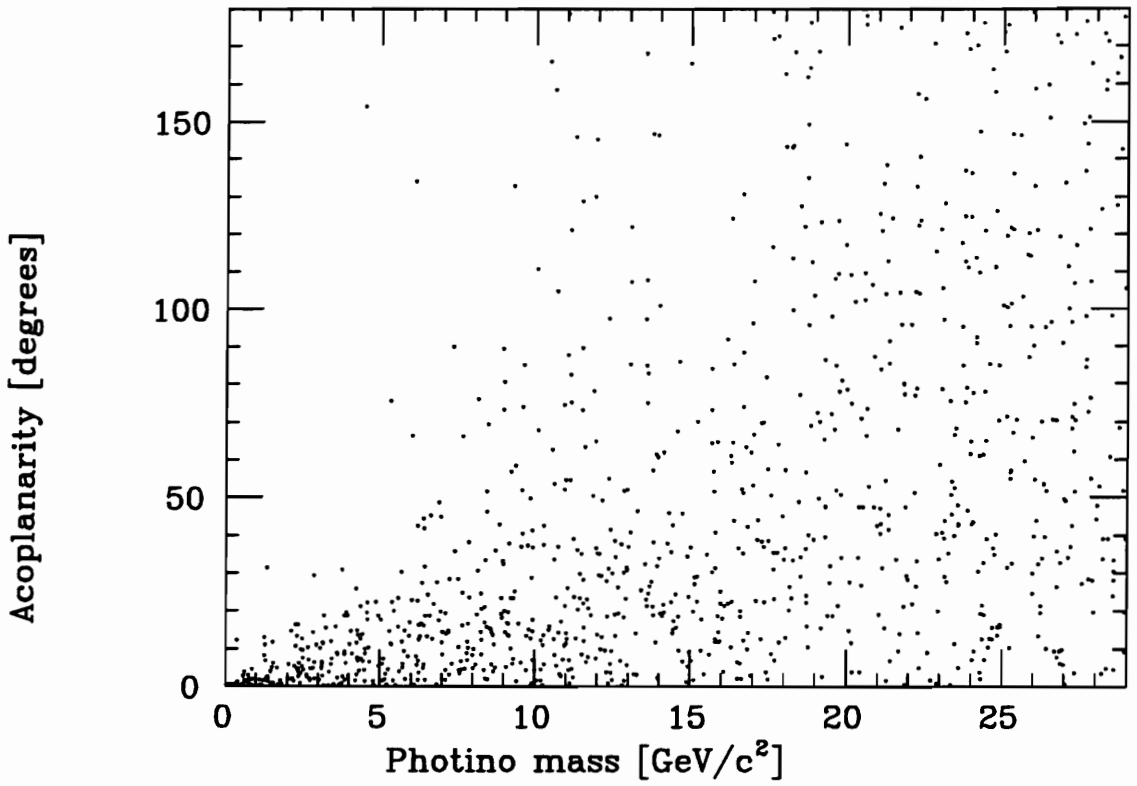

Figure 9-1: Scatter plot of acoplanarity ξ vs. photino mass $M_{\tilde{\gamma}}$.

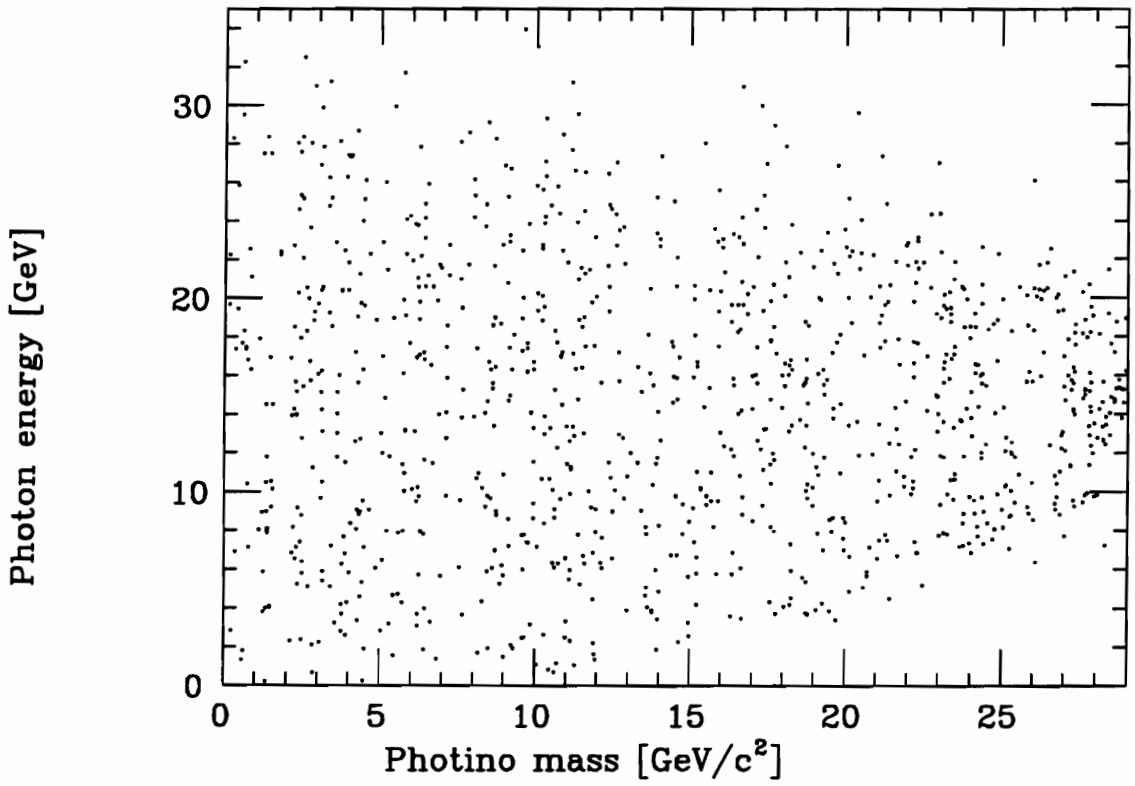

Figure 9-2: Scatter plot of daughter photon energies vs. photino mass $M_{\tilde{\gamma}}$.

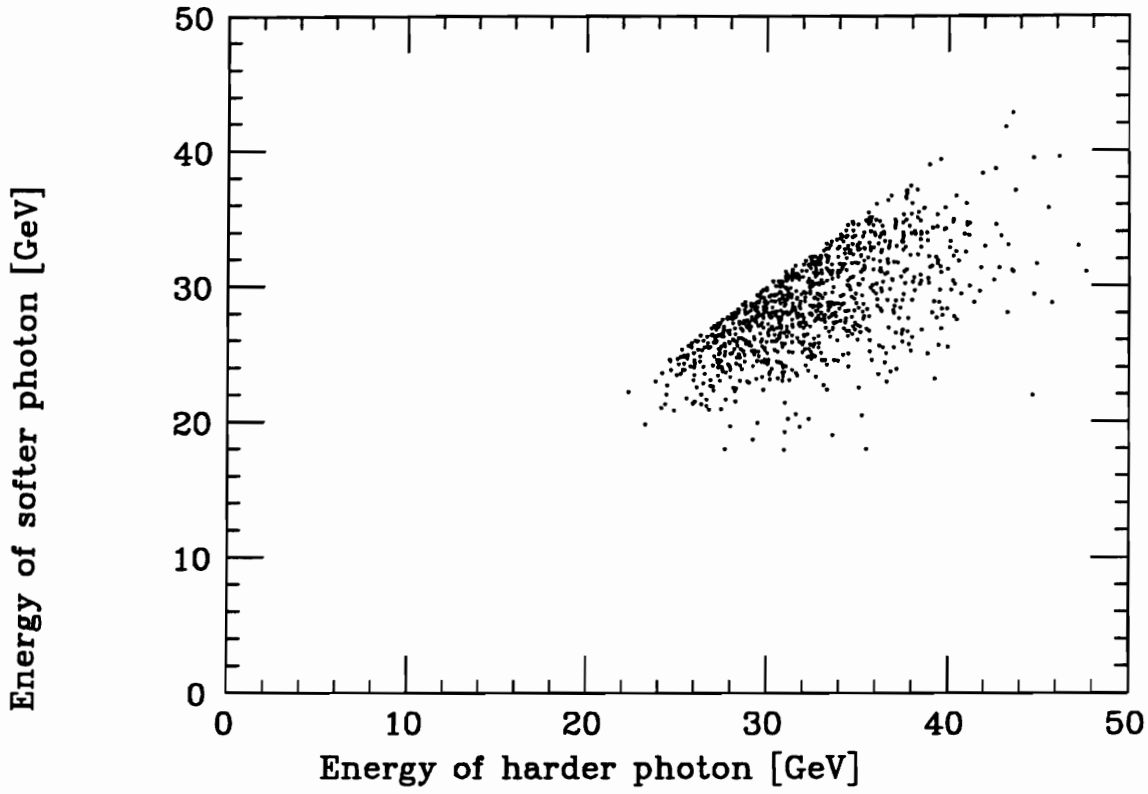

Figure 9-3: Scatter plot of photon energies from $e^+e^- \rightarrow \gamma\gamma$.

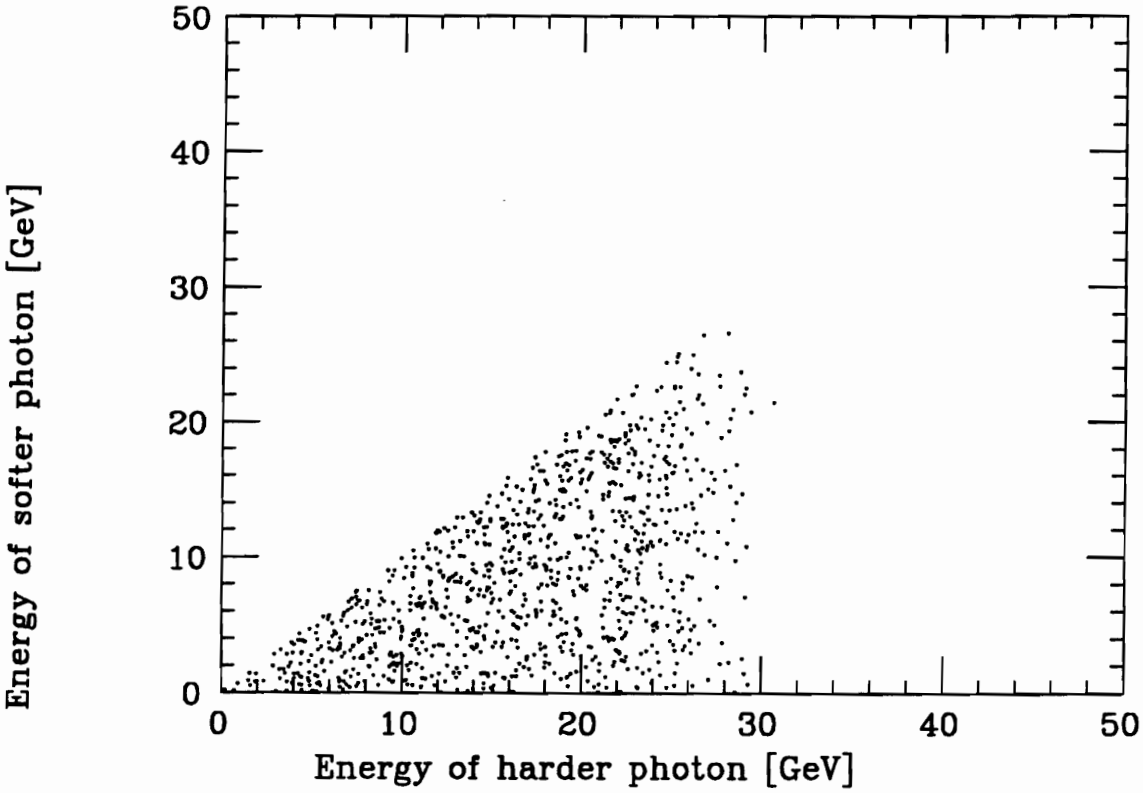

Figure 9-4: Scatter plot of photon energies from $e^+e^- \to \tilde{\gamma}\tilde{\gamma} \to \tilde{G}\tilde{G}\gamma\gamma$, where $M_{\tilde{\gamma}} = 0.5\,\mathrm{GeV}$.

the mechanism is clear enough to disqualify the event. Five other candidates showed very uneven shower development at sextant boundaries. Because this behavior is well understood (although not expressed in the Monte Carlo; see Section 6.4.5), these events are also disqualified.

The three remaining candidates are summarized in Table 9-1. All three events seem to be consistent with $e^+e^- \rightarrow \gamma\gamma$, except that the pulse heights are low. All voltages are recorded as being on. Neighboring events in the database show no anomalies (the third candidate was recorded 12 seconds after a normal SHC Bhabha event). Shower development is normal in all cases, although the long longitudinal profiles seem more consistent with higher-energy showers.

It is curious to note that in each case the acoplanarity is very low, and the photon energies are nearly the same.[3] If we assume that these events are indeed caused by unstable photino decay, the photino mass would have to be very low to have acollinearities of order 1° or less. In this case, however, the photon energy spectrum would extremely broad, and the photon energies unlikely to overlap. For the case of $M_{\tilde{\gamma}} = 0.5$ GeV, for example, only 2% of the surviving events exhibit a topology of $< .3°$ acoplanarity and $< 1.5°$ acollinearity with overlapping photon energies. If we expect a total of three surviving candidate events from both modes, the probability is $\mathcal{O}(10^{-5})$ that all three events will have this topology.

We therefore suggest that these candidate events are $e^+e^- \rightarrow \gamma\gamma$ events recorded during some sort of rare, transient hardware problem. Since we cannot pinpoint the nature of the problem, however, we must accept these events as a possible signal in the calculation of limits.

[3] It is even more curious to note that the CM energies are identical (58 GeV). The first candidate was taken during the miniscule 0.08 pb^{-1} 58 GeV run during the Spring, 1989 energy scan with AMY 1.0.

Table 9-1: Three candidate light photino events.

Run	Event	Photon	Energy (GeV)	θ	ϕ	ζ	ξ
6250	4548	1	9.05	96.9°	241.1°	1.04°	0.16°
		2	7.41	82.1°	61.3°		
10031	5674	1	6.22	115.2°	347.2°	0.84°	0.28°
		2	4.57	65.6°	166.9°		
12180	10920	1	4.94	61.9°	215.1°	0.24°	0.25°
		2	4.20	118.0°	34.9°		

9.2.3 Calculation of Production Limits

To set limits on $M_{\tilde{e}}$ as a function of $M_{\tilde{\gamma}}$, we first establish the upper limit on the observed signal. This can be derived from the formula

$$1 - \alpha = 1 - \frac{e^{-(\mu_B+N)} \sum_{n=0}^{n_0} \frac{(\mu_B + N)^n}{n!}}{e^{-\mu_B} \sum_{n=0}^{n_0} \frac{\mu_B^n}{n!}}, \tag{9.1}$$

where $\alpha = 0.05$ for 95% C.L., μ_B is the number of expected background events, n_0 is the number of observed events, and N is the upper limit on the number of signal events. In the case where we have three observed events and no expected background, $N = 7.754$.

For each value of $M_{\tilde{\gamma}}$ we choose a value for $M_{\tilde{e}}$, and compute an expected number of events by Monte Carlo integration (as described in Section 3.2), summing over the various CM energies, and using luminosities 1000 times greater than in the actual data samples. The value of $M_{\tilde{e}}$ is slowly incremented until the number of surviving MC events drops below 7800, at which point the 95% C.L. limit is set.

The contour for the 95% limit is shown as the dotted line in Figure 9-7.

9.3 High Mass $\tilde{\gamma}$ Search

9.3.1 Background from $e^+e^- \to (\gamma)\gamma\gamma$

The most important requirement that distinguishes high-mass unstable photino events from $e^+e^- \to (\gamma)\gamma\gamma$ events is a high acoplanarity between the two observed barrel photons. We have required that there be no other substantial SHC or endcap tags; this requires that the missing photon be no more than θ_{veto} from the beam axis. If we require the observed photons to be at least 45° away from the beam axis, geometry alone constrains the largest theoretical acoplanarity to be $2\arcsin(\tan\theta_{\mathrm{veto}})$ (this would be 30.20° for the 14.6° veto angle of AMY 1.0, and 6.004° for the 3.0° veto angle of AMY 1.5). Although the finite angular resolution makes larger measured acoplanarities possible, the singular peaking of the $e^+e^- \to \gamma\gamma\gamma$ cross section along the beam axis makes acoplanarities of even a few degrees uncommon.

In Figure 9-5 we see the Monte Carlo acoplanarity distributions for $e^+e^- \to (\gamma)\gamma\gamma$ in AMY 1.0 and AMY 1.5, where the distributions have been scaled to their respective luminosities of 33.55 pb^{-1} and 123.31 pb^{-1}. We have removed $e^+e^- \to \gamma\gamma$ events with additional tagged photons in the SHC, charged tracks, or endcap hits greater than 1 GeV. (The AMY 1.0 plot was produced from the AMY 1.5 fully simulated MC sample by neglecting endcap tags below $\theta = 14.6°$.) We can see in the plot that cuts of 3° for AMY 1.5 and 8° can eliminate virtually all background from $e^+e^- \to (\gamma)\gamma\gamma$. These cuts will also eliminate any misidentified Bhabha events remaining in the sample.

Figure 9-6 shows the Monte Carlo acoplanarity distributions for $e^+e^- \to \tilde{\gamma}\tilde{\gamma} \to \tilde{G}\tilde{G}\gamma\gamma$ at $M_{\tilde{\gamma}} = 25\,\mathrm{GeV}$ and $M_{\tilde{\gamma}} = 1\,\mathrm{GeV}$, with $M_{\tilde{e}} = 50\,\mathrm{GeV}$. We see that even photinos as light as 1 GeV would have a considerably broader acoplanarity distribution than the $e^+e^- \to (\gamma)\gamma\gamma$ background.

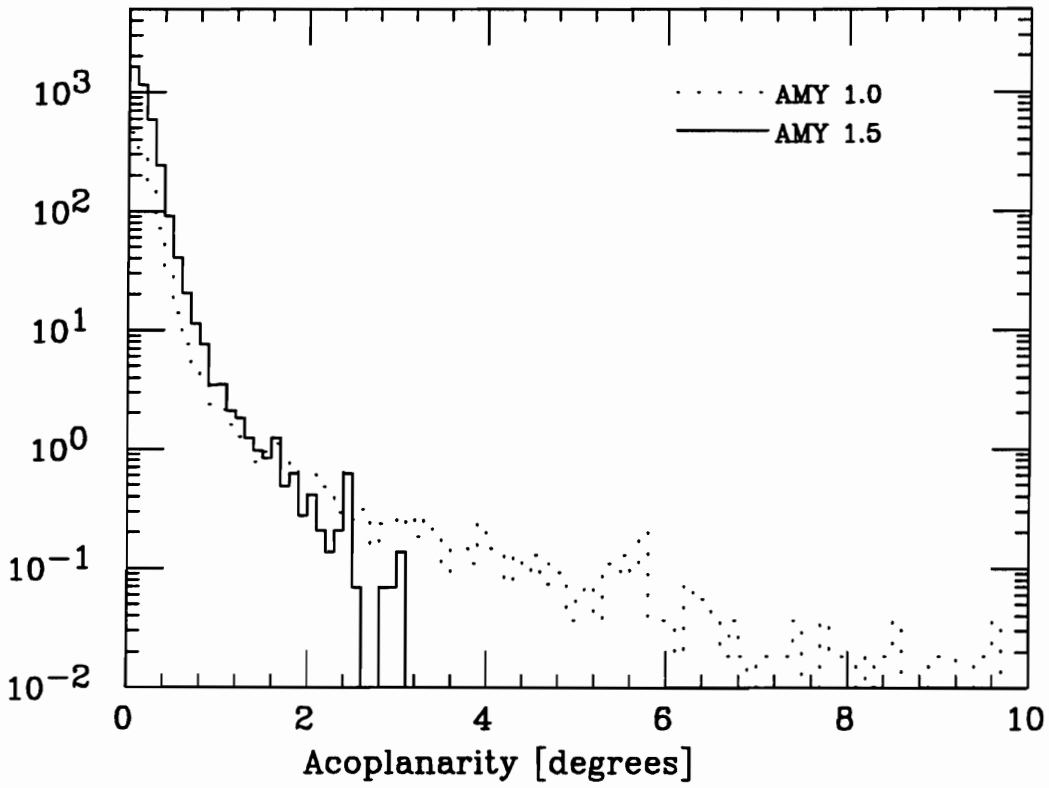

Figure 9-5: Acoplanarity distributions for $e^+e^- \to (\gamma)\gamma\gamma$ in AMY 1.0 and AMY 1.5.

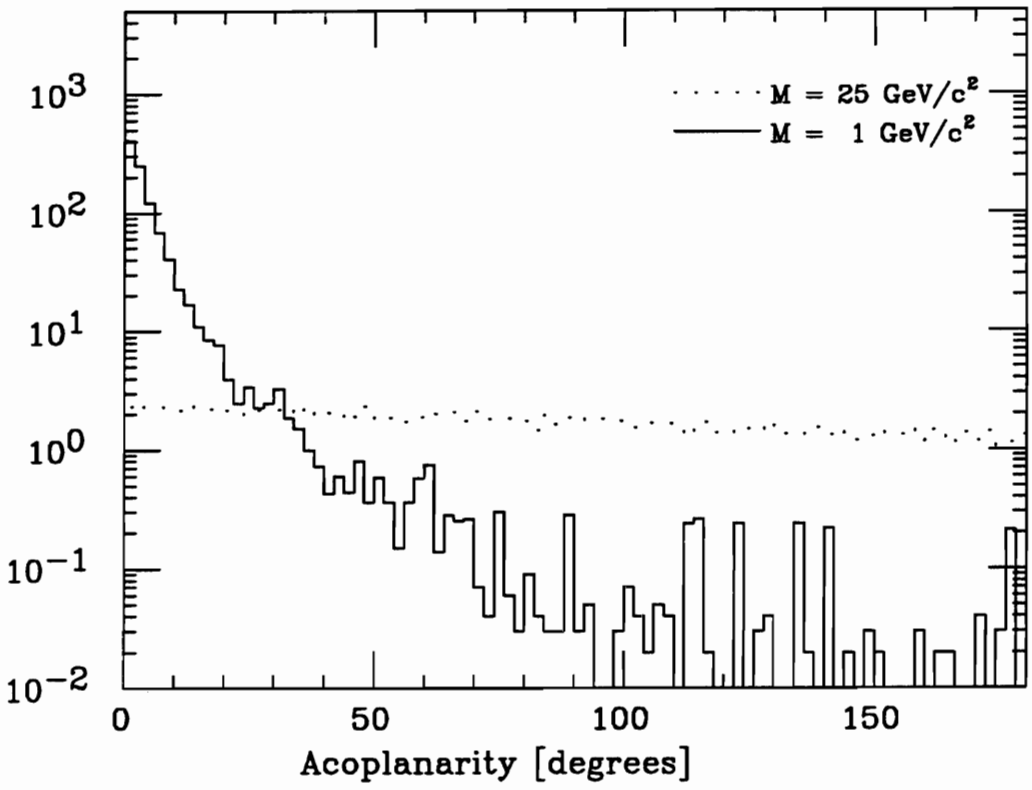

Figure 9-6: Acoplanarity distributions for $e^+e^- \to \tilde{\gamma}\tilde{\gamma} \to \tilde{G}\tilde{G}\gamma\gamma$ with $M_{\tilde{\gamma}} = 25\,\mathrm{GeV}$ and $M_{\tilde{\gamma}} = 1\,\mathrm{GeV}$. Here we use $M_{\tilde{e}} = 50\,\mathrm{GeV}$.

9.3.2 Background from $e^+e^- \rightarrow (e^+e^-)\gamma\gamma$

The process of $e^+e^- \rightarrow (e^+e^-)\gamma\gamma$ is kinematically more similar to the heavy photino decay signature than is $e^+e^- \rightarrow (\gamma)\gamma\gamma$. With two untagged particles in the final state, the difference between missing energy and missing momentum can be substantial.

Fortunately, hard radiated photons are most likely to be radiated along the direction of the initial or final state electrons; photons radiated at large angles tend to be soft. In a smeared, generated sample of 181 pb^{-1}, no events were found that pass the selection criteria for heavy photino decay.

9.3.3 Background from $e^+e^- \rightarrow (\nu\bar{\nu})\gamma\gamma$

With two invisible particles in the final state, it is flatly impossible to remove the $e^+e^- \rightarrow \nu\bar{\nu}\gamma\gamma$ background from the event sample. Using the Monte Carlo described in Section 3.5, we can hope to estimate the contribution from this process to our event sample.

A generated sample of 433 fb^{-1} resulted in 88 events that passed the selection criteria for the heavy photino decay signature. This effective cross section of 0.2 fb is completely negligible at our statistical level, even if we give a generous allowance to the intermediate state radiation diagrams not included in the Mana and Martinez Monte Carlo.

9.3.4 Selection Criteria

For an event to be considered a candidate for high-mass unstable photino decay, we require $\xi \geq 3.0°$ ($\xi \geq 8.0°$ for AMY 1.0), $E_1, E_2 \geq 2$ GeV, $45° \leq (\theta_1, \theta_2) \leq 135°$, and $\zeta < 177°$ (so that the showers are resolvably separated).

9.4 Search Results and Production Limits

No candidate events were found; 0.5 events were expected from the AMY 1.0 sample. In this case Equation 9.1 sets the upper limit on the photino signal at 3.00 events; that is, we require at least 3 expected candidate events to rule out any combination of $M_{\tilde{\gamma}}$ and $M_{\tilde{e}}$ at 95% C.L. Limits on $M_{\tilde{e}}$ are calculated in the same manner as for the light photino case, except that the limit is set at 3000 events for 156.86 fb^{-1} of MC data.

The contour for the 95% limit for heavy photino decay is shown as the solid line in Figure 9-7; the area inside the contour is again excluded. This limit covers almost the entire light photino limit, except for a small sliver in the very lightest photino mass region.

9.5 Comparison to Previous Limits

The AMY 95% C.L. limit is shown in comparison to limits from other collaborations (refs. [72], [86], [65], [87], and [88]) in Figure 9-8. It represents an improvement over previous limits, due mostly to high luminosity and fine angular resolution.

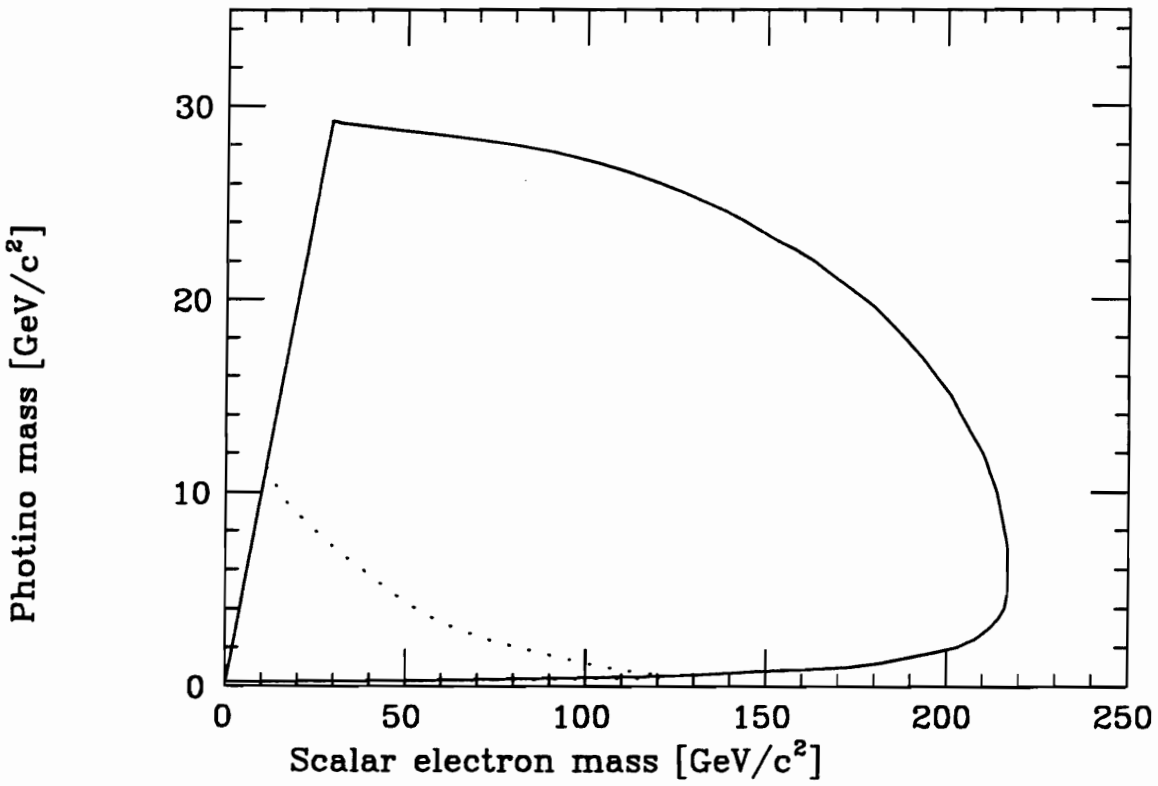

Figure 9-7: 95% C.L. limits from $e^+e^- \rightarrow \tilde{\gamma}\tilde{\gamma} \rightarrow \tilde{G}\tilde{G}\gamma\gamma$.

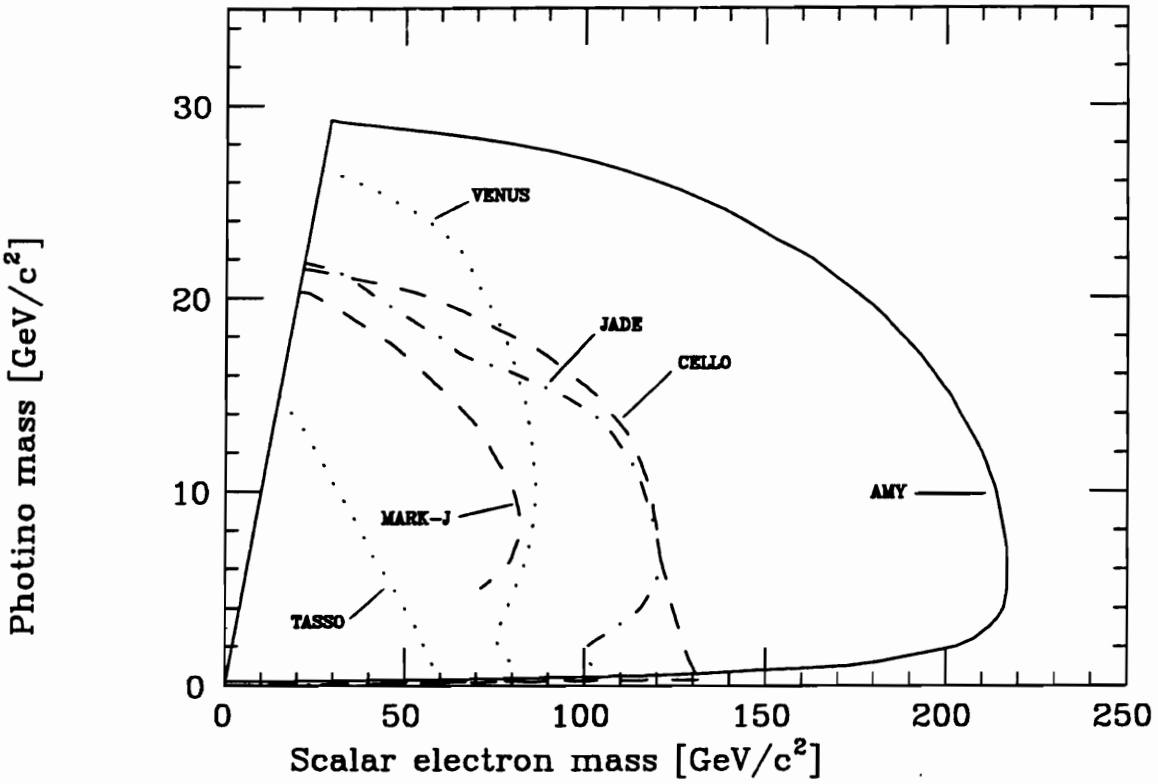

Figure 9-8: 95% C.L. limits from $e^+e^- \rightarrow \tilde{\gamma}\tilde{\gamma} \rightarrow \tilde{G}\tilde{G}\gamma\gamma$, compared to limits from other collaborations.

Chapter 10

Conclusions

We have analyzed data representing $e^+e^- \to \gamma\gamma$ at CM energies from 50 to 64 GeV, primarily at 58 GeV. The integrated cross section has been presented as a function of $\sqrt{s}$ for two detector configurations, with χ^2 values of 16.9 for 12 *dof* for AMY 1.0 and 9.8 for 10 *dof* for AMY 1.5. A plot of $d\sigma/d\Omega$ has also been presented for the summed AMY $e^+e^- \to \gamma\gamma$ sample, with data at different energies scaled by $s/(58\,\mathrm{GeV})^2$. The χ^2 was 15.1 for 14 *dof*, in good agreement with QED.

We have also presented measurements of the process $e^+e^- \to \gamma\gamma\gamma$ at $\sqrt{s} = 58$ GeV. After correcting for longitudinal vertex smearing and preforming kinematical reconstruction, good agreement with QED is obtained. The 101 events found in a 123.31 pb^{-1} subsample of the 58 GeV data yield a cross section of $(0.82 \pm 0.08 \pm 0.01)$ pb, compared to a theoretical value of (0.76 ± 0.02) pb. The photon spectrum and distributions for several kinematical kinematical variables also showed good agreement with QED.

Plots of the measured $e^+e^- \to \gamma\gamma$ cross section vs. $\cos\theta$ at 52, 55, 56, 57 and 58 GeV were then used to search for electron-photon contact interactions. Models with negative interference terms provided somewhat better fits to the data than did QED; this was a direct consequence of a low value for the measured cross section of the 58 GeV data.

We then conducted a search for the decay of unstable photinos, using acoplanar pairs of photons and low-energy collinear photon pairs. Three candidate events were found in the collinear channel, although none were expected. The events have not been easily explained. Their unusual topologies suggest that they are $e^+e^- \rightarrow \gamma\gamma$ events with low pulse heights caused by some unidentified hardware problem. No events were found in the acoplanar channel. The 95% C.L. production limits in the $M_{\tilde{e}}$-$M_{\tilde{\gamma}}$ plane represent an improvement over previously published limits.

Appendix A

Search for Anomalous $\gamma\gamma$ Production at TRISTAN

In September, 1992 the L3 Collaboration reported evidence for a peak near 60 GeV in the γ–γ invariant mass spectrum from $e^+e^- \rightarrow l^+l^-\gamma\gamma$ events. While L3 did not make any claims of a new physical process, the clustering of four events suggested a previously unknown state X with a mass near 60 GeV that decays primarily into a photon pair.

Any such state that can also couple to electrons would be resonantly produced in e^+e^- collisions near 60 GeV. If the state coupled only to photons, it still could be produced in e^+e^- collisions through photon fusion, or through an s-channel virtual photon decaying into $X + \gamma$. The state would be tagged by its decay products, leading to an enhancement of the $e^+e^- \rightarrow \gamma\gamma$ cross section.

To test this possibility, it was decided to run TRISTAN in energy scan mode in December, 1992. Nine energy points were taken with nominal energies between $\sqrt{s} = 57.6$ GeV and $\sqrt{s} = 59.7$ GeV. Approximately 1 to 2 pb^{-1} of data were taken at each point, with 19.44 pb^{-1} taken at 58 GeV.

The rest of this Appendix contains a reproduction of the paper presenting the AMY results from the energy scan [89]. No significant deviation from QED was found. Similar results were reported by VENUS [90] and TOPAZ [91], which took data concurrently with AMY.

Physics Letters B 303 (1993) 385–390
North-Holland

PHYSICS LETTERS B

Search for anomalous $\gamma\gamma$ production at TRISTAN

AMY Collaboration

K.L. Sterner [a], A. Abashian [a], K. Gotow [a], D. Haim [a], M.E. Mattson [a], N. Morgan [a], L. Piilonen [a], P. Kirk [b], C.P. Cheng [c], W.X. Gao [c], W.G. Yan [c], M.H. Ye[c], S. Lusin [d], C. Rosenfeld [d], A.T.M. Wang [d], S. Wilson [d], L.Y. Zheng [d], C.A. Fry [e], R. Tanaka [e], R.E. Breedon [f,s], L.M. Chinitz [f], Winston Ko [f], R.L. Lander [f], J. Rowe [f], J.R. Smith [f], D. Stuart [f], S. Kanda [h], S.L. Olsen [h], K. Ueno [h], K. Abe [g], Y. Fujii [g], Y. Kurihara [g], F. Liu [g], A. Maki [g], T. Nozaki [g], T. Omori [g], H. Sagawa [g], Y. Sakai [g], T. Sasaki [g], Y. Sugimoto [g], Y. Takaiwa [g], S. Terada [g], R. Walker [g,i], F. Kajino [j], R. Poling [k], T. Thomas [k], T. Aso [l], K. Miyano [l], H. Miyata [l], M. Oyoshi [l], M.H. Lee [m], F. Sannes [m], S. Schnetzer [m], R. Stone [m], J. Vinson [m], Y. Yamashita [n], A. Bodek [i], B.J. Kim [i], T. Kumita [i], Y.K. Li [i], C. Velisarris [i], S. Kobayashi [o], A. Murakami [o], S.K. Sahu [o], Y.S. Chung [p], J.S. Kang [p], K.B. Lee [p], K.W. Park [p], S.K. Kim [q], S.S. Myung [q], S.K. Choi [r], D. Son [r], S. Ebara [s], S. Matsumoto [s], N. Takashimizu [s] and T. Ishizuka [t]

[a] *Virginia Polytechnic Institute and State University, Blacksburg, VA 24061, USA*
[b] *Louisiana State University, Baton Rouge, LA 70803, USA*
[c] *Institute of High Energy Physics, Beijing 100039, China*
[d] *University of South Carolina, Columbia, SC 29208, USA*
[e] *SSC Laboratory, Dallas, TX 75237, USA*
[f] *University of California, Davis, CA 95616, USA*
[g] *KEK, National Laboratory for High Energy Physics, Ibaraki 305, Japan*
[h] *University of Hawaii, Honolulu, HI 96822, USA*
[i] *University of Rochester, Rochester, NY 14627, USA*
[j] *Konan University, Kobe 658, Japan*
[k] *University of Minnesota, Minneapolis, MN 55455, USA*
[l] *Niigata University, Niigata 950-21, Japan*
[m] *Rutgers University, Piscataway, NJ 08854, USA*
[n] *Nihon Dental College, Niigata 951, Japan*
[o] *Saga University, Saga 840, Japan*
[p] *Korea University, Seoul 136-701, South Korea*
[q] *Seoul National University, Seoul 151-742, South Korea*
[r] *Kyungpook National University, Taegu 702-701, South Korea*
[s] *Chuo University, Tokyo 112, Japan*
[t] *Saitama University, Urawa 338, Japan*

Received 15 February 1993

We report on measurements of the total cross section for $e^+e^- \to \gamma\gamma$ for center-of-mass energies between 57.4 and 59.5 GeV, using the AMY detector at the TRISTAN collider. We set new limits on the production of a possible new s-channel resonance decaying into photon pairs.

1. Introduction

Recently, the L3 Collaboration at LEP reported on an apparent excess of $e^+e^- \to l^+l^-\gamma\gamma$ events ($l = \mu$ or e) in which the invariant mass of the photon pair was clustered around 59 GeV [1]. The L3 Collaboration

Volume 303, number 3,4 PHYSICS LETTERS B 15 April 1993

did not speculate on the origin of their events beyond noting that the probability of observing such clustering in any 5 GeV wide mass bin above 40 GeV was $O(10^{-3})$, if the events were due purely to QED. The three other experiments at LEP have also reported on such events [2]. Out of fifteen $e^+e^- \to l^+l^-\gamma\gamma$ events found at LEP with $M_{\gamma\gamma} > 40$ GeV, five events were found with a $\gamma\gamma$ invariant mass in a 1 GeV range near 59 GeV.

A few speculative models have been advanced [3,4] on the origin of the clustered events of L3 assuming that they are not due to QED. The models are based on the decay of the Z^0 into a massive object X and another boson, where X may be a scalar–pseudoscalar mixture or a spin-2 particle with a mass of approximately 60 GeV that decays predominantly into two photons. Regardless of the details of such models, if the particle X can couple with electrons, then the direct s-channel production may be observable in the TRISTAN energy range. If there is no coupling of X to fermions, it can still be produced via an s-channel photon that results in $X \to \gamma\gamma$ plus a soft monochromatic photon. Previous studies of $e^+e^- \to \gamma\gamma$, $\gamma\gamma\gamma$ at TRISTAN [5,6] were consistent with the QED prediction, however, no direct search for a narrow resonance was conducted.

We have searched for the direct production of a new state X via the reaction $e^+e^- \to X \to \gamma\gamma$, using the AMY detector at the TRISTAN e^+e^- collider, for center-of-mass energies $\sqrt{s}$ between 57.4 and 59.5 GeV in 250 MeV steps, with 1–2 pb^{-1} of integrated luminosity per point (19 pb^{-1} at 57.8 GeV).

2. The AMY detector

The AMY detector is a general purpose solenoidal-type instrument employing two inner tracking chambers (VTX and ITC), a central drift chamber (CDC), and an electromagnetic calorimeter (SHC), all contained within a 3 T magnetic field, and a barrel muon detector (MUO) outside the magnet return yoke. The end cap regions are instrumented with calorimeters (ESC) and small-angle luminosity monitors (SAC). The AMY detector has been described in detail elsewhere [7].

Final states with two or more photons are detected primarily by the SHC. This is a 14.4 radiation length gas-sampling calorimeter, consisting of twenty alternating layers of lead and resistive plastic proportional tubes [8]. Each tube layer is sandwiched between cathode strips in the ϕ and θ directions. The SHC is constructed in six sextants, each covering an azimuthal range of 60° and a polar angle range of $|\cos\theta| < 0.73$.

Measurement of electromagnetic shower locations and energies in the SHC is determined by the signals from the cathode strips. The strips are arranged in projective towers that subtend an angle of 14.2 mr from the interaction point, and are ganged internally into five longitudinal divisions. The empirical energy resolution is found to be $\Delta E/E = 0.23/\sqrt{E} + 0.06$, with E in GeV. The large constant term is thought to be due to the effects of operating in the 3 T magnetic field. Shower centroids are typically located in ϕ and θ to less than one strip width.

Triggering. Within a given layer of the SHC, anode signals are ganged into 48 azimuthal sections; the ganged signals are summed externally over multiple layers to form trigger signals for 48 towers with either no segmentation or four longitudinal divisions. Three redundant combinations of these signals provide triggering for $e^+e^- \to \gamma\gamma$ events: (1) total energy trigger – the analog sum of all 48 trigger signals exceeding 8 GeV, (2) two-cluster trigger – two separate towers in coincidence with energies exceeding 5 GeV for one and 3 GeV for the other, and (3) shower shape trigger – coincidence between any two successive longitudinal divisions in a given tower, or in neighboring towers, with total energy exceeding 3 GeV.

Bhabha electrons are used to check the triggering efficiency independently, since they behave similarly to $\gamma\gamma$ events in the SHC. Bhabha events are triggered independently by the SHC triggers and by charged-track triggers derived from signals in the CDC and ITC. By examining the frequency of Bhabha events with a track trigger but no SHC trigger, we found the SHC trigger efficiency for Bhabha events to be essentially 100%. We assume, therefore, that the SHC triggering efficiency for $\gamma\gamma$ events exceeded 99% for all of the data of this study.

Luminosity determination. To search for an anomaly in the production of $\gamma\gamma$ events, the most critical parameter aside from event statistics is the reliable determination of the integrated luminosity. This is accomplished in the AMY experiment by recording

small-angle Bhabha events in the ESC, a sampling calorimeter constructed of alternating layers of lead and scintillator, with proportional tubes at the depth of the electromagnetic shower maximum for position determination. The ESC covers the polar angle range $0.799 < |\cos\theta| < 0.982$. The systematic error in ESC luminosity is estimated to be ~2%, and is dominated by the precision on alignment and fiducial definition.

3. Event selection and Monte Carlo

The selection of $e^+e^- \to n\gamma$ events ($n \geq 2$) was performed according to the following criteria: (1) at least two SHC clusters with energies greater than $\frac{1}{3}E_{\text{beam}}$ each, (2) the polar angle for each such cluster in the range $45° < \theta < 135°$, (3) the acollinearity angle between the two most energetic clusters of at most 10°, and (4) no charged tracks in the event. The resulting sample of 1054 events was visually scanned, resulting in the rejection of 19 background events from cosmic rays, misidentified Bhabhas, and SHC noise.

The cross section for $e^+e^- \to \gamma\gamma$, including radiative corrections to $O(\alpha^3)$, was calculated by Monte Carlo integration using a program by Fujimoto, Igarashi, and Shimizu [9,10]. This program is an implementation of the BASES/SPRING Monte Carlo package by Kawabata [11]. The cross section of 34.81 ± 0.18 pb is based on a fully simulated sample of 1.06 fb^{-1} at 58 GeV that was subjected to the same selection criteria as the experimental data. This value includes an event selection efficiency of $\varepsilon_{\gamma\gamma} = 0.933 \pm 0.011$.

We estimate the error in normalization for this analysis to be 2.3%, taking into account the uncertainty in the luminosity measurement and including the error in the $\gamma\gamma$ event selection efficiency.

4. Results

Table 1 summarizes the results of the energy scan. The center-of-mass energies $\sqrt{s}$ represent their actual values at the AMY interaction point rather than the nominal accelerator energies. The quantity σ_E represents the RMS width of the center-of-mass energy distribution. The luminosities L are those obtained with the ESC. The quantity N_γ [N_{QED}] represents the number of observed [simulated] $n\gamma$ ($n \geq 2$) events that pass the event selection criteria; N_{QED} is derived from the Monte Carlo simulation at 58 GeV discussed earlier, scaled by s and adjusted to the tabulated luminosity. The ratio of the observed $\gamma\gamma$ events to that expected from the standard model is also shown for each center-of-mass energy.

Barrel Bhabha events obtained concurrently with $\gamma\gamma$ events are used to test the internal consistency of the runs and to provide an additional check for systematic errors. For each center-of-mass energy, the ratio of observed barrel Bhabha events to ESC luminosity is scaled by s. These quantities are given in the last column of table 1, and indicate the constancy in the operation of the SHC during the scan runs.

Table 1
Results of the energy scan. $\sqrt{s}$ is the center-of-mass energy, σ_E is the width of the center-of-mass energy distribution, L is the integrated luminosity from the ESC, N_{QED} is the number of events expected from QED alone, $N_{\gamma\gamma}$ is the number of $e^+e^- \to \gamma\gamma$ seen, and N^s_{BB}/L is the number of barrel Bhabha events seen per pb^{-1} of luminosity, scaled by s.

$\sqrt{s}$ (GeV)	σ_E (GeV)	L (pb^{-1})	N_{QED}	$N_{\gamma\gamma}$	$N_{\gamma\gamma}/N_{\text{QED}}$	N^s_{BB}/L
57.374	0.095	2.05	72.9±0.4	69	0.95 ±0.11	265 ±11
57.772	0.096	19.55	680.5±3.4	636	0.935±0.037	276.0± 3.8
57.972	0.096	1.39	48.4±0.2	49	1.01 ±0.15	272 ±14
58.220	0.098	1.33	45.8±0.2	50	1.09 ±0.15	259 ±14
58.470	0.098	1.33	45.6±0.2	54	1.18 ±0.16	308 ±15
58.718	0.099	1.73	58.7±0.3	61	1.04 ±0.13	278 ±13
58.968	0.100	1.36	45.9±0.2	45	0.98 ±0.15	284 ±15
59.216	0.100	1.21	40.5±0.2	45	1.11 ±0.17	294 ±16
59.466	0.102	0.97	32.3±0.2	26	0.81 ±0.16	236 ±16

5. Analysis

The ratio of observed $n\gamma$ events ($n \geq 2$) to the QED expectation is plotted as a function of center-of-mass energy in fig. 1. The vertical error bars on the ratios are statistical only; the horizontal error bars indicate the RMS spread in $\sqrt{s}$ rather than the error on the central values. A comparison of the data to QED alone, allowing the normalization to float without constraint, gives a fully consisent fit with the χ^2/d.o.f. = 0.68 for 8 degrees of freedom and a normalization value of 0.961 ± 0.029. This fit is shown as the solid curve in fig. 1. The deviation of the normalization from unity is consistent, given the 2.9% statistical uncertainty from the fit on this parameter as well as the 2.3% normalization uncertainty mentioned above.

To examine the effect of a new state X, we again allow the normalization of the $\gamma\gamma$ data to float without constraint, and then compare these data to a model in which the $\gamma\gamma$ events are produced by an s-channel resonance X of mass M and total width Γ that sums incoherently with the conventional QED processes.

The effective cross section for production of X at center-of-mass energy $\sqrt{s}$, integrated over the solid angle of the SHC, is parameterized by a Breit–Wigner form:

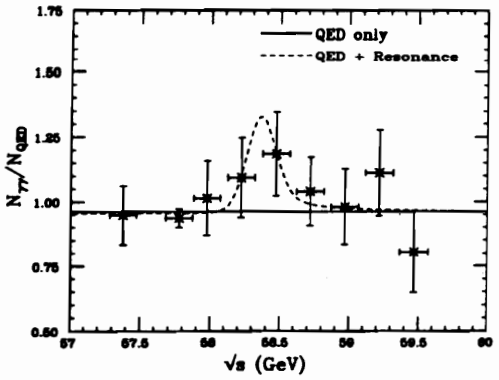

Fig. 1. Ratio of observed $\gamma\gamma$ events to the QED prediction. The solid curve is the QED prediction, with χ^2/d.o.f. = 0.68 for 8 degrees of freedom and a normalization of 0.961. The dashed curve is the maximum likelihood prediction, with χ^2/d.o.f. = 0.47 for 5 degrees of freedom and a normalization of 0.955.

$$\sigma_X(s) = (2J+1)\Gamma_{ee}\mathrm{BR}_{\gamma\gamma} f(s, M, \Gamma)\,, \tag{1}$$

where

$$f(s, M, \Gamma) = (\Omega\epsilon)_{\mathrm{eff}} \frac{\pi}{s} \frac{\Gamma}{(M-\sqrt{s})^2 + \frac{1}{4}\Gamma^2}\,. \tag{2}$$

Γ_{ee} is the partial width for $X \to e^+e^-$, $\mathrm{BR}_{\gamma\gamma} \equiv \Gamma_{\gamma\gamma}/\Gamma$ is the branching ratio for $X \to \gamma\gamma$, and $(\Omega\epsilon)_{\mathrm{eff}}$ is the effective acceptance for detecting $e^+e^- \to \gamma\gamma$. We use $(\Omega\epsilon)_{\mathrm{eff}} = \Omega_{\mathrm{SHC}} \cdot \epsilon_{\gamma\gamma} = 0.707 \cdot 0.933 = 0.659$. (This must be modified somewhat if the differential cross section is not isotropic.) The cross section σ_X is then convolved with the radiatively corrected beam resolution function [12]

$$G_{\mathrm{R}}(s, E) = \left(\frac{2\sigma_E}{\sqrt{s}}\right)^t \frac{t}{\sqrt{2\pi}\,\sigma_E} \times \int_0^\infty x^{t-1} \exp[-\tfrac{1}{2}(z-x)^2]\,\mathrm{d}x\,, \tag{3}$$

where $z = (\sqrt{s}-E)/\sigma_E$, $t = 2(\alpha/\pi)[\ln(s/m_e^2) - 1]$, and σ_E is the width of the center-of-mass energy distribution from table 1, to give the observed effective cross section

$$\bar{\sigma}_X(s) = (2J+1)\Gamma_{ee}\mathrm{BR}_{\gamma\gamma} \times \int_0^\infty f(E^2, M, \Gamma) G_{\mathrm{R}}(s, E)\,\mathrm{d}E\,. \tag{4}$$

The number of events expected from this process at center-of-mass energy $\sqrt{s}$ for an integrated luminosity L is given by $N_X(s) = \bar{\sigma}_X(s) \cdot L$, and adds to the number expected from QED alone, $N_{\mathrm{QED}}(s)$, listed in table 1.

For a normalization A_0, the likelihood of observing $N_X(s_i)$ events from s-channel production of X at center-of-mass energy $\sqrt{s_i}$ is a rescaled Poisson distribution [13]:

$$\mathscr{L}(s_i) = A_0 \exp\{N_{\mathrm{QED}}(s_i) - A_0[N_X(s_i) + N_{\mathrm{QED}}(s_i)]\} \times \left(\frac{A_0[N_X(s_i) + N_{\mathrm{QED}}(s_i)]}{N_{\mathrm{QED}}(s_i)}\right)^{N_{\gamma\gamma}(s_i)} \tag{5}$$

and the overall likelihood is $\mathscr{L} = \prod_i \mathscr{L}(s_i)$.

This likelihood function peaks at $M = 58.35^{+0.24}_{-0.08}$ GeV, $\Gamma = 16 \pm 13$ MeV and $(2J+1)\Gamma_{ee}\mathrm{Br}_{\gamma\gamma} = 4.2^{+3.4}_{-3.1}$ keV, with a normalization of $A_0 = 0.955 \pm 0.040$. The

Volume 303, number 3,4 PHYSICS LETTERS B 15 April 1993

best-fit curve of $A_0(N_X+N_{QED})/N_{QED}$ is shown as the dashed curve in fig. 1. A comparison of this curve to the data has χ^2/d.o.f.=0.47 with 5 degrees of freedom. Compared to χ^2/d.o.f.=0.68 with 8 degrees of freedom for QED alone, we conclude that this peak is not statistically significant.

We extract 90% confidence level upper limits on $(2J+1)\Gamma_{ee}BR_{\gamma\gamma}$ for the normalization of 0.955 and particular choices of M and Γ, by numerical integration of the likelihood function [#1]. These limits are shown in fig. 2. It is apparent that the limits are insensitive to the total width Γ when it is comparable to or smaller than the center-of-mass energy spread σ_E. Furthermore, the limits shift only slightly if the normalization is varied from is maximum likelihood value.

Upper limits on $(2J+1)\Gamma_{ee}BR_{\gamma\gamma}$ at the 90% confidence level range from 0.5 keV to 8 keV, for an X mass between 57 and 59.6 GeV and a total width Γ below 100 MeV. Our limits can be compared directly with the expectation from the L3 observation of $e^+e^-\to l^+l^-\gamma\gamma$ under the assumption that their clustered events arose from the production of a new state X. For example, if we assume that X is a scalar that couples only to photon and lepton pairs with a total width of $\Gamma\equiv\Gamma_{\gamma\gamma}+3\Gamma_{ee}$, then an upper limit on $(2J+1)\Gamma_{ee}BR_{\gamma\gamma}$ can be converted into an exclusion region in the plane of $\Gamma_{\gamma\gamma}$ versus Γ_{ee}. Our 90% CL upper limit is shown in fig. 3 for a scalar X of mass 59 GeV.

Our limits may be incorporated with 90% CL limits of other experiments such as the L3 measurements [1] of $e^+e^-\to l^+l^-\gamma\gamma$ and the OPAL measurement [14] of $e^+e^-\to\gamma\gamma\gamma$. For the former case, we calculate [15] the cross section using the automatic amplitude generator GRACE [16] including all possible diagrams. The limits from the three events with M_γ clustered near 59 GeV observed by the L3 Collaboration are shown as the dashed curve in fig. 3, while the limits imposed by the absence of a l^+l^- invariant mass near 59 GeV are given by the dash-dotted curve. The limits set by the non-observation of an excess of events with $M_{\gamma\gamma}=59$ GeV in the OPAL $\gamma\gamma\gamma$ measurement are shown as the dotted curve of fig. 3. The limits of our measurement are thereby restricted to satisfying the condition that $\Gamma_{\gamma\gamma}<10.6$ MeV and $\Gamma_{ee}<120$ MeV. To summarize, the four *inclusion* regions overlap in the lower left of fig. 3.

For a (pseudo-)scalar that couples directly to pairs of fermions as well as photons, the exact forms of the decay widths for $X\to e^+e^-$ and $X\to\gamma\gamma$ are

[#1] Since the data are consistent with pure QED, the confidence *interval* includes the point $(2J+1)\Gamma_{ee}BR_{\gamma\gamma}=0$.

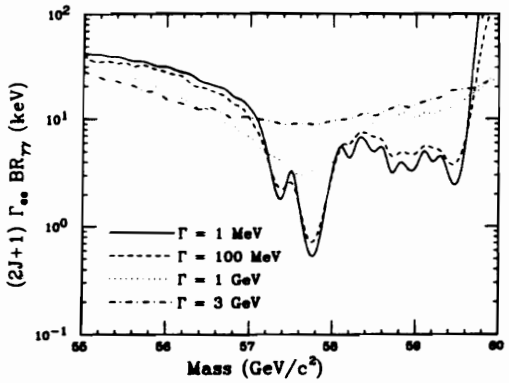

Fig. 2. 90% CL upper limits on $(2J+1)\Gamma_{ee}BR_{\gamma\gamma}$ as a function of mass M of the state X, for widths of 1 MeV (solid curve), 100 MeV (dashed curve), 1 GeV (dotted curve) and 3 GeV (dash-dotted curve), with a normalization of 0.955. The region above a given curve is excluded.

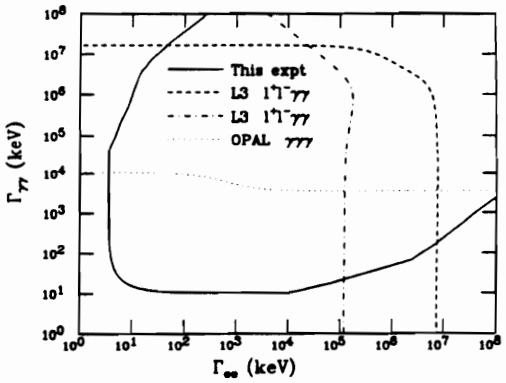

Fig. 3. Exclusion regions (90% CL) on $\Gamma_{\gamma\gamma}$ versus Γ_{ee} for a scalar X with $M\sim 59$ GeV, assuming $\Gamma\equiv\Gamma_{\gamma\gamma}+3\Gamma_{ee}$. The region above and to the right of a given curve is excluded. The solid curve is from this experiment. The other curves are from the observation of up to three $l^+l^-\gamma\gamma$ events with $M_{\gamma\gamma}\sim 59$ GeV (dashed) and the absence of $l^+l^-\gamma\gamma$ events with $M_{l^+l^-}\sim 59$ GeV (dash-dotted) (ref. [1]), and from the lack of a signal at $M_{\gamma\gamma}\sim 59$ GeV in $\gamma\gamma\gamma$ events (dotted) (ref. [14]).

$$\Gamma_{ee} = \frac{g_{ee}^2}{8\pi} M, \tag{6}$$

$$\Gamma_{\gamma\gamma} = \frac{\alpha^2}{64\pi^3} \frac{M^3}{F_X^2}, \tag{7}$$

respectively, where g_{ee} is the coupling constant of X to electrons, α is the fine structure constant, and F_X is a mass parameter analogous to f_π in π^0 decay. We use $\alpha/\pi F_X$ as the coupling constant of X to $\gamma\gamma$. Assuming that $BR_{\gamma\gamma} \sim 1$, we can convert the 90% CL upper limit on $\Gamma_{ee}BR_{\gamma\gamma}$ from our likelihood analysis into an upper limit on g_{ee} of 1.78×10^{-3}. We also place a 90% CL lower limit on F_X of 730 MeV that comes from the OPAL upper limit on $\Gamma_{\gamma\gamma}$ of 10.6 MeV [14]. We examine the effect of these limits upon the $ee\gamma$ vertex correction value, $(g-2)_e$, which will have an additional contribution from this model of the form [17]

$$\mathscr{A}_X \simeq \frac{m_e}{F_X} \frac{\alpha g_{ee}}{4\pi^3} \ln \frac{\Lambda}{M}, \tag{8}$$

where Λ is the ultraviolet cutoff (fixed at 1 TeV). our limits on F_X and g_{ee} imply an upper bound of $\mathscr{A}_X < 2.0\times10^{-10}$, which is within the maximum allowed contribution [18] to $(g-2)_e$ of 2.7×10^{-10}.

6. Conclusion

We have searched for resonant production of a new state X in e^+e^- collisions that couples to photon pairs at center-of-mass energies between 57.4 and 59.5 GeV. We find that the observed data are consistent with the QED prediction for $e^+e^- \to \gamma\gamma$ (χ^2/d.o.f. $=0.68$ for 8 degrees of freedom). Furthermore, we have extracted 90% CL upper limits on $(2J+1)\Gamma_{ee} \times BR_{\gamma\gamma}$ of 0.5–8.0 keV for the process $e^+e^- \to X \to \gamma\gamma$, should a state X exist with a mass between 57 and 59.6 GeV.

Acknowledgement

We thank the TRISTAN staff for the excellent operation of the storage ring. In addition we acknowledge the strong support provided by the staffs of our home institutions. We are particularly indebted to professor Lay Nam Chang for fruitful discussions on the theoretical aspects of this paper. This work has been supported by the Japan Ministry of Education, Science and Culture (Monbusho), the Japan Society for the Promotion of Science, the US Department of Energy, the US National Science Foundation, the Korean Science and Engineering Foundation, the Ministry of Education of Korea and the Academia Sinica of the People's Republic of China.

References

[1] L3 Collab., O. Adriani et al., Phys. Lett. B 295 (1992) 337.
[2] S. Komamiya, K.W. Bell and S. Holmgven, private communications.
[3] R. Garisto and J.N. Ng, preprint TRI-PP-92-124 (16 December 1992).
[4] K. Hagiwara and S. Matsumoto, private communications.
[5] K. Abe et al., Z. Phys. C 45 (1989) 175.
[6] K. Shimozawa et al., Phys. Lett. B 284 (1992) 144.
[7] AMY Collab., T. Kumita et al., Phys. Rev. D 24 (1990) 1339.
[8] A. Abashian et al., Nucl. Instrum. Methods A, to be published.
[9] J. Fujimoto and M. Igarashi, Prog. Theor. Phys. 74 (1985) 791.
[10] J. Fujimoto, M. Igarashi and Y. Shimizu, Prog. Theor. Phys. 77 (1987) 118.
[11] S. Kawabata, Comput. Phys. Commun. 41 (1986) 127.
[12] J.D. Jackson and D.L. Scharre, Nucl. Instrum. Methods 128 (1975) 13.
[13] O. Helene, Nucl. Instrum. Methods 212 (1983) 319.
[14] OPAL Collab., M.Z. Akrawy et al., Phys. Lett. B 257 (1991) 531.
[15] Y. Kurihara, unpublished.
[16] H. Tanaka, Comput. Phys. Commun. 58 (1990) 153;
H. Tanaka, T. Kaneko and Y. Shimizu, Comput. Phys. Commun. 64 (1991) 149;
T. Kaneko, in: New computing techniques in physics research, eds. D. Perret-Gallix and W. Wojcik (Edition du CRNS, Paris, 1990) p. 555.
[17] F. del Águila, A. Méndez and R. Pascual, Phys. Lett. B 140 (1984) 431.
[18] T. Kinoshita and W.B. Linquist, Phsy. Rev. Lett. 47 (1981) 1573.

Appendix B

Photon Conversion to e^+e^- Pair

The main cause of inefficiency within the fiducial volume for $e^+e^- \rightarrow n\gamma$ events is the presence of charged tracks. These are almost exclusively produced through the conversion of a photon into an e^+e^- pair in the EM field of an atomic nucleus.

The probability of $\gamma \rightarrow e^+e^-$ conversion is proportional to the radiative thickness of the material. The most likely place for such an interaction to occur is at the beam pipe, although conversions do occur in the straw chambers, and even within the gas volume of the CDC. The conversion rate for a single photon will be equal to a constant divided by $\sin\theta$.

The Monte Carlo rate of photon conversion to an e^+e^- pair is shown as a function of polar angle in Figure B-1 for the 1.5 mm thick aluminum beam pipe of AMY 1.0, and for the 1 mm thick beryllium beam pipe of AMY 1.5.[1] Samples of 10 GeV photons were used in the simulator; however, the probability of pair production is insensitive to photon energy for high energy photons. The conversion constants are determined to be $C_1 = 0.0278$ for the aluminum beam pipe and $C_2 = 0.0187$ for the beryllium beam pipe.

[1]The aluminum beam pipe of AMY 1.0 was also used with AMY 1.5 during the spring, 1990 data taking run. The photon conversion correction used for the small amount of data taken in fall, 1989 with a 1 mm thick aluminum beam pipe is virtually identical to that for the beryllium pipe.

Roughly one-third of $e^+e^- \to \gamma\gamma \to \gamma e^+e^-$ events will have the distinctive topology of a highly acollinear e^+e^- pair back-to-back with a beam-energy photon. It is a common practice to select these events, and include them in the $e^+e^- \to \gamma\gamma$ sample.

If we wish to include such events in our analysis, we must also consider the background from radiative Bhabha scattering. Consider the case where there is a very hard (*i.e.* beam energy) photon radiated from an initial state electron and an s-channel virtual photon. The virtual photon in this case is nearly on-shell, causing a singularity in the cross section (referred to as the s' channel singularity). The virtual photon couples to e^+e^-, which are produced in an extremely boosted frame and are therefore highly acollinear in the detector frame.

Candidate events are required to have a highly ($> 170°$) acollinear e^+e^- pair back-to-back with a photon. The photon and the summed e^+e^- momentum are required to satisfy the $e^+e^- \to \gamma\gamma$ selection criteria.

The 1.82 fb^{-1} sample of fully simulated $e^+e^- \to \gamma\gamma, \gamma\gamma\gamma$ events yielded 1562 candidate events, for an effective cross section of $0.858 \pm 0.022\,pb^{-1}$. A 962 pb^{-1} generator-level sample of $e^+e^- \to e^+e^-\gamma$ events yielded 766.3 events (taking into account the probability of the final state photon converting to another e^+e^- pair), for an effective cross section of $0.797 \pm 0.028\,pb^{-1}$. The samples were kinematically almost identical, with similar angular distributions.

The number of events expected from the combined processes from the beginning of AMY 1.0 to the end of the Spring, 1992 run is 269 ± 6 events. The experimental data yields 249 ± 16 events. Because this sample is so small compared to the $e^+e^- \to \gamma\gamma$ sample, because the signal-to-noise ratio is almost 1:1, and because the photon conversion data were not available for the most recent run periods, it was decided not to incorporate these events into the $e^+e^- \to \gamma\gamma$ cross section.

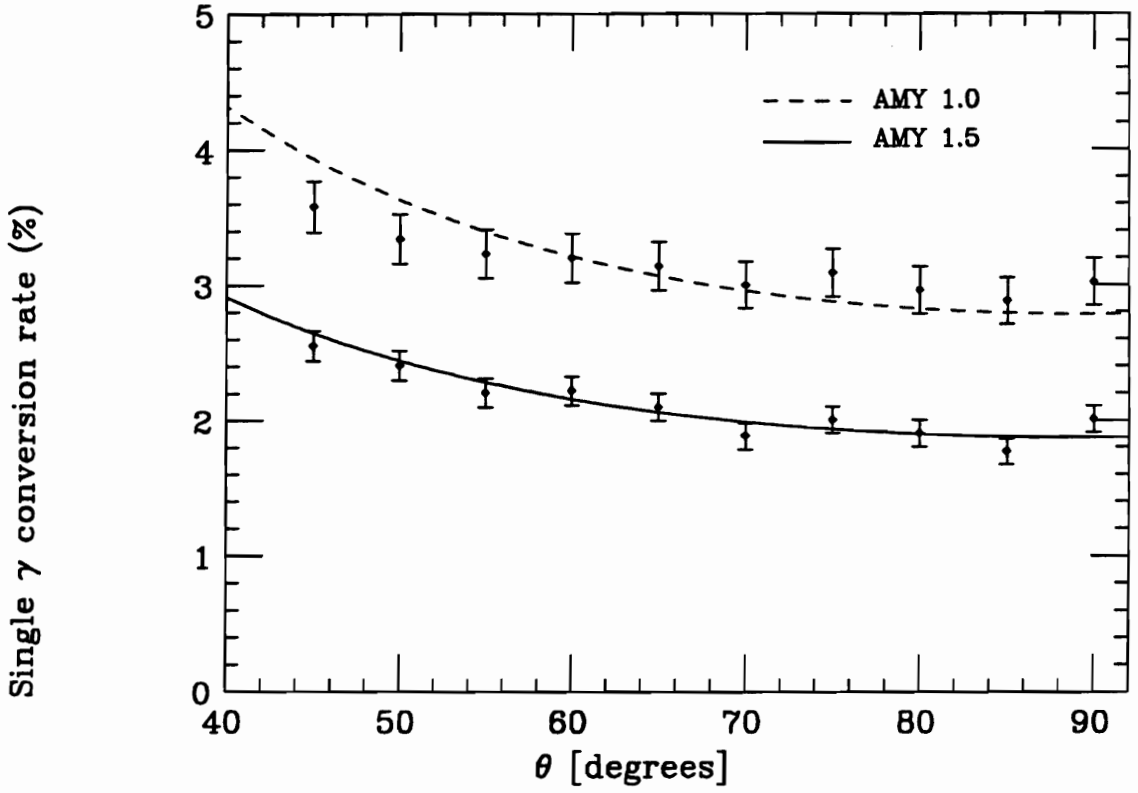

Figure B-1: Rate of $\gamma \rightarrow e^+e^-$ for 10 GeV photons.

Bibliography

[1] F. Bloch and A. Nordsieck, *Phys. Rev.* **52** (1937), 54.

[2] O. Adriani *et al.* (L3 Collaboration), *Phys. Lett.* **295B** (1992), 337.

[3] F.M. Renard, *Nucl. Phys.* **B196** (1982), 93.

[4] A. Barroso *et al.*, *Z. Phys.* **C28** (1985), 149.

[5] J. Fujimoto, M. Igarashi, Y. Shimizu, *Prog. Theor. Phys.* **77** (1987), 118.

[6] M. Capdequi Peyranere, Y. Loubatieres, M. Talon, *Nucl. Phys.* **B249** (1985), 61.

[7] L.M. Brown and R.P. Feynman, *Phys. Rev.* **85** (1952), 231.

[8] D.R. Yennie, S.C. Frautschi, H. Suura, *Ann. Phys.* **13** (1961), 379.

[9] I. Harris and L.M. Brown, *Phys. Rev.* **105** (1957), 1656.

[10] F.A. Berends and R. Gastmans, *Nucl. Phys.* **B61** (1973), 414.

[11] F.A. Berends and R. Kleiss, *Nucl. Phys.* **B186** (1981), 22.

[12] A. Andreassi *et al.*, *Phys. Rev.* **128** (1962), 1425.

[13] J. Fujimoto and M. Igarashi, *Prog. Theor. Phys.* **74** (1985), 791.

[14] F. Mandl and T.H.R. Skyrme, *Proc. Roy. Soc.* **A215** (1952), 497.

[15] Yu.A. Gol'fand and E.P. Likhtman, *JETP Lett.* **13** (1971), 393.
D.V. Volkov and V.P. Akulov, *JETP Lett.* **16** (1972), 438.
J. Wess and B. Zumino, *Nucl. Phys.* **B70** (1974), 39.

[16] H. Goldberg, *Phys. Rev. Lett.* **50** (1983), 1419.

[17] J.E. Kim, A. Masiero, D.V. Nanopoulos, *Phys. Lett.* **139B** (1984), 346.

[18] N. Cabibbo, G. Farrar, L. Maiani, *Phys. Lett.* **105B** (1981), 155.

[19] J. Ellis and J.S. Hagelin, *Phys. Lett.* **122B** (1983), 303.

[20] H.E. Haber and G.L. Kane, *Phys. Rep.* **117** (1985), 239ff.

[21] P. Fayet, *Nucl. Phys.* **B237** (1984), 367.

[22] S.D. Drell, *Ann. Phys.* **4** (1958), 75.

[23] K. Hagiwara, *Recommendations on Compositeness Studies at TRISTAN* (1988), unpublished.

[24] H.J. Lipkin, *Phys. Rev. Lett.* **44** (1980), 710.

[25] K. Satoh, *Proceedings of the KEK Topical Conference on* e^+e^- *Collision Physics* (1989), 205.

[26] C. Back *et al.*, (AMY Collaboration), *TRISTAN-EXP-003* (1984).

[27] Y. Doi, *et al.*, *Nucl. Inst. Meth.* **A274** (1989), 95.

[28] A. Maki *et al.*, AMY note 455 (1988).

[29] M. Frautschi *et al.*, *Nucl. Inst. Meth.* **A307** (1991), 52.

[30] K. Ueno *et al.*, University of Rochester preprint *UR-1050* (1988), Submitted to *Nucl. Inst. Meth.*

[31] F. Kajino *et al.*, *Nucl. Inst. Meth.* **A245** (1986) 507.

[32] A. Abashian *et al.*, Submitted to *Nucl. Inst. Meth.*

[33] Y. Sugimoto, AMY note 583 (1992).

[34] Y.C. Zhu, KEK Internal *86-25* (1987).

[35] H. Asakura et al., *Rep. Fac. Sci. Engrg.* (Saga University) **16** (1988), 101.

[36] H. Harada *et al.*, *Nucl. Inst. Meth.* **A265** (1988), 141.

[37] T. Yasuda, Masters Thesis, Chuo University (1989).

[38] Y. Sugimoto, private communication.

[39] A. Sill, University of Rochester preprint *UR-1192* (1990).

[40] Steven E. Koonin and Dawn C. Meredith, *Computational Physics (FORTRAN Version)*, Addison Wesley (1990), 197.

[41] S. Kawabata, *Comp. Phys. Comm.* **41** (1986), 127.

[42] K. Tobimatsu and Y. Shimizu, *Prog. Theor. Phys.* **74** (1985), 567. K. Tobimatsu and Y. Shimizu, *Prog. Theor. Phys.* **75** (1986), 905.

[43] S. Jadach *et al.* CERN preprint *TH-6230* (1991).

[44] B.F.L. Ward, private communication.

[45] F.A. Berends *et al.*, *Nucl. Phys.* **B301** (1988), 583.

[46] P. Mani and T. Nozaki, AMY Computer Note 12a.

[47] W.R. Nelson *et al.*, SLAC-Report-265 (1985).

[48] U. Amaldi, *Physica Scripta* **23** (1981), 409.

[49] E. Low, AMY note 545 (1990).

[50] H. Sagawa, AMY note 552 (1990).

[51] S.S. Myung, Doctoral Thesis, Korea University (1988).

[52] S. Sakamoto, AMY note 420 (1988).

[53] F. Kajino, AMY note 369 (1987).

[54] M. Derrick *et al.* (HRS Collaboration), *Phys. Lett.* **166B** (1986), 468.

[55] M. Derrick *et al.* (HRS Collaboration), *Phys. Rev.* **D34** (1986), 3286.

[56] E. Fernandez *et al.* (MAC Collaboration), *Phys. Rev.* **D35** (1987), 1.

[57] B. Adeva *et al.* (MARK-J Collaboration), *Phys. Rev. Lett.* **48** (1982), 967.

[58] B. Adeva *et al.* (MARK-J Collaboration), *Phys. Rev. Lett.* **53** (1984), 134.

[59] H.J. Behrend *et al.* (CELLO Collaboration), *Phys. Lett.* **103B** (1981), 148.

[60] H.J. Behrend *et al.* (CELLO Collaboration), *Phys. Lett.* **123B** (1983), 127.

[61] H.J. Behrend *et al.* (CELLO Collaboration), *Phys. Lett.* **140B** (1984), 130.

[62] H.J. Behrend *et al.* (CELLO Collaboration), *Phys. Lett.* **168B** (1986), 420.

[63] W. Bartel *et al.* (JADE Collaboration), *Phys. Lett.* **92B** (1980), 206.

[64] W. Bartel *et al.* (JADE Collaboration), *Z. Phys.* **C19** (1983), 197.

[65] M. Althoff *et al.* (TASSO Collaboration), *Z. Phys.* **C26** (1984), 337.

[66] M. Althoff *et al.* (TASSO Collaboration), *Phys. Lett.* **154B** (1985), 236.

[67] Ch. Berger *et al.* (PLUTO Collaboration), *Phys. Lett.* **94B** (1980), 87.

[68] S.K. Kim, Doctoral Thesis, Korea University (1988), unpublished.

[69] H.J. Kim, Doctoral Thesis, Korea University (1989), unpublished.

[70] S.K. Kim *et al.* (AMY Collaboration), *Phys. Lett.* **223B** (1989), 476.

[71] H.J. Kim *et al.* (AMY Collaboration), KEK preprint *89-52 AMY 89-11* (1989).

[72] K. Abe *et al.* (VENUS Collaboration), *Z. Phys.* **C45** (1989), 175.

[73] I. Adachi *et al.* (TOPAZ Collaboration), *Phys. Lett.* **200B** (1988), 391.

[74] K. Shimozawa *et al.* (TOPAZ Collaboration), *Phys. Lett.* **284B** (1992), 144.

[75] M.Z. Akrawy *et al.* (OPAL Collaboration), *Phys. Lett.* **241B** (1990), 133.

[76] M.Z. Akrawy *et al.* (OPAL Collaboration), *Phys. Lett.* **257B** (1991), 531.

[77] B. Adeva, *et al.* (L3 Collaboration), *Phys. Lett.* **250B** (1990), 199.

[78] B. Adeva, *et al.* (L3 Collaboration), *Phys. Lett.* **288B** (1992), 404.

[79] P. Abreu *et al.* (DELPHI Collaboration), *Phys. Lett.* **268B** (1991), 296.

[80] D. Decamp *et al.* (ALEPH Collaboration), *Phys. Lett.* **241B** (1990), 635.

[81] M.E. Mattson, AMY note 565 (1991).

[82] J.A. Nelder and R. Mead, *Computer Journal* **7** (1965), 308.

[83] H.J. Behrend *et al.* (CELLO Collaboration), *Z. Phys.* **C51** (1991), 149.

[84] H. Kroha, *Phys. Rev.* **D46** (1991), 58.

[85] D. Buskulic *et al.* (ALEPH Collaboration), *Z. Phys.* **C59** (1993), 215.

[86] H.J. Behrend *et al.* (CELLO Collaboration), *Z. Phys.* **C35** (1987), 181.

[87] W. Bartel *et al.* (JADE Collaboration), *Phys. Lett.* **139B** (1984), 327.

[88] B. Adeva *et al.* (MARK-J Collaboration), *Phys. Rep.* **109** (1984), 131.

[89] K.L. Sterner *et al.* (AMY Collaboration), *Phys. Lett.* **303B** (1993), 385.

[90] K. Abe *et al.* (VENUS Collaboration), *Phys. Lett.* **302B** (1993), 119.

[91] K. Abe *et al.* (TOPAZ Collaboration), *Phys. Lett.* **304B** (1993), 373.

Vita

Kevin Leslie Sterner was born on March 1, 1965 in Atlanta, GA. He received a B.S. degree in astronomy and physics from the State University of New York at Stony Brook in 1986. In 1990 he received an M.S. degree in general physics from Virginia Polytechnic Institute and State University. He received his Ph.D. from VPI&SU in 1993 in experimental high energy physics, using data taken with the AMY detector at TRISTAN. His advisor was Professor Alexander Abashian.